Dissection of host factors regulating pathological and protective immune responses in murine models of tuberculosis

Eunsol Choi

The Graduate School
Yonsei University
Department of Medical Science

Dissection of host factors regulating pathological and protective immune responses in murine models of tuberculosis

Eunsol Choi

The Graduate School
Yonsei University
Department of Medical Science

Dissection of host factors regulating pathological and protective immune responses in murine models of tuberculosis

A Doctoral Dissertation Submitted
to the Department of Medical Science
and the Graduate School of Yonsei University
in partial fulfillment of the
requirements for the degree of
Doctor of Philosophy in Medical Science

Eunsol Choi

January 2025

This certifies that the Doctoral Dissertation of Eunsol Choi is approved

Thesis Supervisor	Sung Jae Shin
Thesis Committee Member	Kihyuck Kwak
Thesis Committee Member	Jungsik Song
Thesis Committee Member	Sang-Jun Ha
Thesis Committee Member	Hyun-Jeong Ko

The Graduate School
Yonsei University

January 2025

ACKNOWLEDGEMENTS

First and foremost, I extend my sincere gratitude to all those who have supported me throughout the completion of my thesis.

Professor Sung Jae Shin, my advisor, deserves my utmost appreciation for his invaluable guidance and support during my doctoral journey. His mentorship has been pivotal in shaping me into a Ph.D. student capable of contributing meaningfully to the society as a future scientist. I am grateful for his strong leadership, sincere guidance, insightful advice, and financial support, which have successfully led Tolerance Breaking Lab to become the foremost Tuberculosis researchers in Korea.

I am also indebted to my thesis committee members, **Professor Kihyuck Kwak, Jungsik Song, Sang-Jun Ha, and Hyun-Jung Ko**, for their unwavering support and constructive feedback over the years. Their contributions have significantly enhanced the quality of my thesis and expanded my understanding of my research field. I am deeply appreciative of their mentorship as I embark on my journey as a future scientist.

Special thanks go to my colleagues and former colleagues in the TB Lab, particularly **Professor Kee Woong Kwon**, whose influence and encouragement have been instrumental in my perseverance throughout

my research endeavors. I am also grateful to **Hagyu Kim** and **Soon Myung Kang** for their companionship and support during challenging times. I extend my heartfelt gratitude to Hong-Hee Choi for her guidance and expertise in research on the NOX2KO mouse model, which has been invaluable to my growth as a scientist.

I would like to express my appreciation to all other members of the TB Lab, including **Dr. Lee Han Kim, Dr. Jihae Park, Dr. Hongmin Kim, Dr. Jumi Lee, Jaehun Park, Keueunsan Kim, Yeeun Bak, Yura Ha, Hyunji Kim, Jiyun Park, Sangwon Choi, Yerin Jeon, Seunghyun Lee, Hyeso Ah, Kyungmin Kim**, and **Wonseok Jeong**, for their camaraderie and support during my time as a student. Additionally, I am thankful to **Maro Kim**, **Hyunji Jang**, **Ingon Ryu**, and **Jieun Lee** for their assistance with experimental procedures as *in vivo* specialized researchers.

Finally, my deepest appreciation goes to my parents, **Dr. Hyun Choi** and **Mrs. Jinwon Kim,** for their unwavering support and encouragement. And to my beloved fiancée, **Amélie Solange Madeleine Bonhour**, your steadfast support has been a constant source of strength and inspiration.

Thank you all for your support and encouragement.

TABLE OF CONTENTS

LIST OF FIGURES

Chapter II

Chapter III

Chapter IV

ABSTRACT

Dissection of host factors regulating pathological and protective immune responses in murine models of tuberculosis

Tuberculosis (TB) is a severe pulmonary infectious disease caused by *Mycobacterium tuberculosis* (Mtb) infection, posing a persistent global public health. In order to advance understanding of TB pathogenesis and devise novel, efficacious preventive measures, there is an imperative need for in-depth exploration of anti-TB immunity mechanisms and host factors. To deepen our understanding of immune responses in the context of tuberculosis (TB) immunopathogenesis, we employed a novel approach by utilizing a NADPH Oxidase 2 (NOX2) knockout (*Nox2*$^{-/-}$) mouse model. This model resembles X-linked Chronic Granulomatous Disease (CGD) in human patients and is known to exhibit susceptibility to intracellular pathogens, including Mtb. Additionally, we employed another knockout mouse model, the Cholesterol 25-hydroxylase (CH25H) knockout mouse, which has been reported to demonstrate resistance to intracellular pathogens. By utilizing these distinct mouse models with opposing responses to intracellular pathogens, we aimed to identify critical host factors contributing to susceptibility or resistance against Mtb infection and to elucidate the underlying mechanisms.

Chapter I provides a comprehensive overview of immune alterations caused by NADPH Oxidase 2 deficiency, which exhibits altered immune responses across a spectrum of pathogens. This chapter delves into the immunological characteristics of NOX2 deficiency, exploring both innate and adaptive immunity, with a particular emphasis on deficiencies in phagocytosis, dysregulation of

immune cell populations, and excessive inflammation. Subsequent chapters will focus on how Mtb infection induces irregular immunologic characteristics in mouse models and whether these uncontrolled immune features influence tuberculosis susceptibility or anti-tuberculosis immunity *in vivo*.

Chapter II focuses on the establishment of a tuberculosis (TB)-susceptible male *Nox2*$^{-/-}$ mouse model and the screening process of host factors correlated with TB progression. Through *in vivo* challenge with the highly virulent Mtb K strain, male *Nox2*$^{-/-}$ mice displayed exacerbated TB pathogenesis compared to wild type (WT) mice and female *Nox2*$^{-/-}$ mice. We could conclude that the disrupted immune tolerance observed in male *Nox2*$^{-/-}$ mice following Mtb challenge, characterized by the dominance of pathogenic immature lung neutrophils and uncontrolled inflammation, is hypothesized to be the reason for TB susceptibility in this mouse model. Furthermore, we analyzed the functional and phenotypic properties of atypical *Nox2*$^{-/-}$ lung neutrophils and concluded that these cells are key drivers of TB pathogenesis in the susceptible male *Nox2*$^{-/-}$ mouse model.

Chapter III delves into the pathogenic role of pulmonary neutrophils and the underlying immunologic mechanisms required for the generation of detrimental immature neutrophils. To identify specific immunologic factors contributing to the uncontrolled generation of pathogenic neutrophils, excessive cytokines upregulated by Mtb infection in male *Nox2*$^{-/-}$ mice were neutralized using cytokine-specific mAbs. We concluded that G-CSF, rather than other pro-inflammatory cytokines, is the key factor driving the generation of pathogenic immature lung neutrophils. This chapter highlights the pivotal role of G-CSF and pulmonary neutrophil generation in TB pathogenesis and proposes the therapeutic potential of targeting the G-CSF–immature neutrophil axis to modulate TB susceptibility.

Chapter IV presents a novel approach to modifying anti-TB immunity through the use of a distinct

mouse model. Our study revealed that CH25H deficiency, an interferon-stimulated gene (ISG), alters dendritic cell functionality and enhances Th1 immunity, a critical component of effective defense against Mtb infection. Furthermore, we demonstrated that CH25H deficiency significantly boosts the efficacy of BCG vaccination by promoting Th1 memory responses and sustaining prolonged anti-TB immunity established by BCG immunization *in vivo*. These findings provide a new perspective on anti-TB immunity by leveraging a unique TB-resistant mouse model with ISG deficiency.

Collectively, these findings advance our understanding of the immunological factors that underpin TB pathogenesis in susceptible animal models or individuals. By elucidating the intricate mechanisms of immune dysfunction in TB susceptibility, this research provides valuable insights that can inform future studies and therapeutic strategies.

Key words : tuberculosis, *Mycobacterium tuberculosis*, immunopathogenesis, NADPH Oxidase 2, inflammation, neutrophil, G-CSF, type I interferon, Cholesterol 25-hydroxylase, BCG

Chapter I

NADPH Oxidase 2 deficiency and its impacts on immune alterations

1. INTRODUCTION

Reactive Oxygen Species (ROS) are pivotal in orchestrating diverse cellular reactions in eukaryotic organisms. While mitochondria primarily govern ROS production, NADPH Oxidase (NOX) also assumes a notable role in ROS generation. Both mitochondrial ROS and NOX-driven ROS are essential elements in modulating a range of cellular responses, spanning from intracellular signaling to cytoskeleton organization[1,2]. Presently, through diverse research conducted in mouse and human studies, seven NADPH oxidases are recognized: NOX1, NOX2, NOX3, NOX4, NOX5, DUOX 1, and DUOX2, each demonstrating distinct functions and tissue localization. NOX2 was the initial member identified and extensively researched in phagocytes, particularly neutrophils[3,4]. It is a multimeric enzyme, composed of one catalytic transmembrane heterodimer (gp91phox / p22phox) and four cytosolic subunits (p40phox / p47phox / p67phox / Rac). Among the six major components of the NOX2 complex, gp91phox serves as the catalytic core for ROS generation[5,6]. NOX2 plays a central role in the non-mitochondrial production of ROS in phagocytes. These NOX2-driven ROS are involved in various cellular responses, ranging from autophagy to cytokine and chemokine signaling[7-9].

Impaired NOX2 function in humans can lead to the development of chronic granulomatous disease (CGD), a genetic disorder characterized by increased susceptibility to pathogens and uncontrolled inflammation[10-12]. Since *Nox2* (*gp91*) is located at Xp21.1 allele of the X chromosome, CGD caused by *Nox2* deficiency, X-linked CGD, is inherited in an X-linked recessive manner, primarily affecting young males[13,14]. Individuals diagnosed with CGD demonstrate excessive susceptibility to various pathogens, including *Mycobacterium tuberculosis* (Mtb), as well as bacterial and fungal infections[15,16]. These infections often lead to the development of granulomas within vital organs, such as the lungs, liver, kidneys, and brain, when exposed to pathogens. Despite progressions in antibacterial and antifungal prophylactic treatments, the life expectancy of CGD patients remains notably lower in contrast to that of the general population.

This chapter illustrates the impacts of NOX2 deficiency on disrupting proper immune responses against pathogens or autoimmunity, based on clinical and experimental reports. Beyond its role in host defense through ROS-mediated direct killing of pathogens, various reports highlight the roles of NOX2 in regulating adaptive immune responses and maintaining immune homeostasis. The chapter elucidates the multifaceted impacts of impaired NOX2 function in immunity, encompassing its roles in phagocyte function, inflammation, adaptive immune responses, and its involvement in the pathogenesis of immune-mediated diseases. Moreover, the potential of the NOX2KO mouse model as a tool to study tuberculosis (TB) susceptibility shall be discussed by dissecting altered immune responses in NOX2-deficient individuals and animals.

2. Altered immune responses in NOX2-deficient mice and humans

2.1. Impaired microbial killing

Deficiencies in microbial killing capacity represent one of the most extensively studied immunologic features associated with NOX2 deficiency. This impairment in microbial clearance efficacy, particularly against intracellular pathogens, is widely documented across various immune responses. Research has consistently highlighted the role of NOX2 in the generation of ROS, which play a crucial role in the eradication of invading microbes. NOX2-driven ROS mediates rapid oxidization, leading to an instant decrease in cytosolic pH and activation of various phagocytic enzymes, thereby facilitating efficient microbial killing and clearance by phagocytes[17,18]. For instance, NOX2-driven ROS production by neutrophils has the capability to directly eliminate intracellular pathogens due to the potent oxidative nature of ROS[19,20]. As NOX2-derived ROS is extremely significant and indispensable in the primary innate immune responses against microbial threats, the impaired production of ROS in NOX2-deficient CGD patients significantly compromises the ability of phagocytes to eliminate pathogens effectively. This deficiency in ROS production undermines the microbial killing capacity of phagocytes, leading to persistent and recurrent infections in affected individuals[21]. Consequently, individuals with NOX2 deficiency are predisposed to recurrent bacterial and fungal infections, as evidenced by numerous infection models and clinical studies[15,22,23]. Furthermore, CGD patients also feature susceptibilities to parasitic infections, expanding the spectrum of pathogens associated with NOX2 deficiency[24-26].

2.2. Susceptibility to infections

Individuals with NOX2 deficiency exhibit heightened susceptibility to a broad spectrum of bacterial and fungal infections, encompassing pathogens such as *Staphylococcus aureus*[27],

Aspergillus species[28], *Pseudomonas cepacia*[29], and *Burkholderia cepacia*[30]. These infections often present as recurrent abscesses, pneumonia, and systemic infections, reflecting the compromised immune response in individuals deficient in NOX2[23]. CGD patients frequently exhibit impaired fungal clearance, predisposing them to recurrent and often severe infections. Among the most prevalent fungal pathogens in CGD patients are *Aspergillus* species, including *Aspergillus myofasciitis* and *Aspergillus fumigatus*, which frequently cause invasive infections[31,32]. *Aspergillus* infections in CGD patients typically manifest as invasive pulmonary aspergillosis, with the potential to rapidly advance and spread to other organs if not promptly treated[33]. Additionally, infections by *Candida* species[34], *Cryptococcus neoformans*[35], and *Scedosporium*[36] species have been documented in CGD patients. These infections may present with a diverse array of clinical manifestations, including skin and soft tissue abscesses, hepatosplenic infections, and involvement of the central nervous system[37].

2.3. Susceptibility to mycobacterial infections

Patients with CGD also exhibit an elevated susceptibility to mycobacterial infections, including *Mycobacterium tuberculosis* (Mtb) and *Mycobacterium avium*, both of which are gram-negative intracellular pathogens[38,39]. This heightened susceptibility presents significant challenges for tuberculosis (TB) therapy and prevention in CGD patients. Conventional Bacillus Calmette-Guérin (BCG) vaccination cannot be safely administered to CGD patients due to the heightened risk of BCGosis, a disseminated infection caused by *Mycobacterium bovis*, which results from BCG vaccination. BCGosis is more frequently observed in male patients due to the nature of the NOX2 gene, which is located on the X chromosome and inherited recessively[16,40-42]. Although phagocyte NADPH oxidase-originated ROS plays a crucial role in clearing intracellular pathogens, studies have shown that phagocyte NADPH oxidase deficiencies did not significantly alter mycobacterial

growth. Studies adapting NOX2-deficient mouse models illustrated the underlying immunologic mechanism in the pathogenesis of TB in NOX2 deficient mice. Olive et al. pointed out that NOX2-deficient mice show increased lung inflammation, but not a distinct increase in pulmonary bacterial load. Such pulmonary inflammation in Mtb-infected NOX2-deficient mice is caused by IL-1 signaling-mediated influx of permissive granulocytes[3]. Thomas et al. supported the idea, showing that NOX2-deficient mice display pulmonary inflammation and an influx of neutrophils, which is dependent on Caspase 1/11 and IL-1 signaling pathways. [43]. Similar IL-1-mediated neutrophilic inflammation is also reported in a model of *Mycobacterium marinum* infection, which causes severe pulmonary inflammation under NOX2 deficient conditions[44].

2.4. Dysregulated inflammation

Dysregulated inflammatory responses represent another prominent hallmark associated with NOX2 deficiency. Experimental studies utilizing NOX2-deficient mice and clinical observations in X-linked CGD patients consistently demonstrate a propensity for uncontrolled inflammation upon pathogenic challenge[45]. Research findings underscore the pivotal role of NOX2-derived reactive oxygen species (ROS) in modulating inflammatory processes. In the absence of functional NOX2, dysregulated inflammation ensues, characterized by aberrant cytokine production, tissue damage, and the establishment of chronic inflammatory states.[45-47]. NOX2-deficient phagocytes, such as macrophages and neutrophils, are major producers of pro-inflammatory cytokines[48,49], which can cause tissue damage[44,50]. For instance, Segal et al. demonstrated the role of NOX2 in regulating zymosan-induced pulmonary inflammation, which is mediated by uncontrolled pro-inflammatory cytokine production through lung neutrophils.[46]. Liao et al. illustrated the roles of NOX2-deficient neutrophils in facilitating joint inflammation, which involves the production of excessive pro-inflammatory cytokines and reduced expression of the checkpoint molecule PD-

L1[48]. Furthermore, Song et al. illustrated that the IL-1-G-CSF axis is upregulated by neutrophils in NOX2-deficient mice, serving as a positive feedback mechanism that amplifies neutrophilic pulmonary inflammation[50,51]. Indeed, various studies underscore phagocytes as the primary source of uncontrolled inflammation in NOX2-deficient mice. However, a recent study by Keller et al. reported that impaired NOX2 function in dendritic cells (DCs) results in excessive presentation of autoantigens. This presentation triggers uncontrolled neutroinflammation in an EAE model mediated by CD4 T cells[52].

2.5. Altered neutrophil function

Neutrophils stand as the foremost phagocytic cells pivotal to innate immunity, with NOX2 playing a critical role in their antimicrobial function. Therefore, the impacts of impaired ROS production are highlighted in neutrophils. Studies elucidate that NOX2-deficient neutrophils manifest compromised microbial killing capabilities and diminished oxidative burst upon encountering pathogens, consequently impeding effective pathogen eradication[53,54]. However, impaired phagocytic capacity is not the only functional alteration in NOX2-deficient neutrophils. They also exhibit aberrant chemotaxis, attributed to disrupted rearrangements of the cytoskeleton and defective signaling pathways involved in cell polarization and motility[55]. For instance, NOX2-deficient neutrophils display impaired direction sensing in the model of zymosan-mediated inflammation, regulated by TREM-1[56]. Impaired NOX2 function also disrupts neutrophil apoptosis, resulting in a prolonged neutrophil lifespan. This leads to the perpetuation of inflammatory responses, thereby contributing to tissue damage. Such delay in neutrophil apoptosis is demonstrated in studies by Carneiro et al., revealing that NOX2-originated oxidative burst plays crucial roles in inducing proper clearance of inflammatory neutrophils in *Leishmania* infection[57,58]. Furthermore, as mentioned above, NOX2-deficient neutrophils serve as the primary source of pro-

inflammatory cytokine secretion. NOX2 deficiency alters cytokine production profiles, resulting in an overproduction of pro-inflammatory cytokines such as TNF-α and IL-1β. These alterations occur due to modifications in various pathways, including ERK1/2[47,59-61]. NOX2 deficiency is also reported to be correlated with excessive neutrophil extracellular trap (NET) formation in infection models. Although NOX-driven ROS are crucial for the generation of NETs, studies on NETosis triggered by *Staphylococcus aureus* infection propose that NETs can also be induced through NOX-independent pathways[62,63]. NETosis in NOX2-deficient neutrophils can promote inflammation and lung damage through neutrophil-platelet interactions in zymosan-induced lung inflammation. [64]

2.6. Macrophage dysfunction

In addition to its impact on neutrophil function, NOX2 deficiency significantly influences macrophage activity, leading to impaired pathogen phagocytosis and reduced reactive oxygen species (ROS) production. Studies have demonstrated that NOX2-deficient macrophages exhibit compromised phagocytic capabilities and decreased ROS generation upon encountering pathogens, consequently undermining the host's ability to control infections and resolve inflammation[65]. The impaired ROS production in NOX2-deficient macrophages not only affects microbial killing but also disrupts signaling pathways essential for the regulation of inflammatory responses. Barrett et al. emphasized alterations in the IL-10/STAT3 axis mediated by NOX2-deficient macrophages, which consequently alter macrophage-mediated cytokine production in the model of neuroinflammation[66,67]. Interestingly, Idol et al. proposed different aspects of NOX2 deficiency in neutrophils and macrophages. They suggested that NOX2-specific deletion increased excessive inflammation only in neutrophils, but not in macrophages, in the model of *Aspergillus fumigatus*-induced fungal infection[68]. Thus, NOX2 deficiency may alter the phagocytic capacities

of macrophages, while its impacts on defective regulation of inflammation might be specific to neutrophils.

2.7. Uncontrolled influx of myeloid cells and granuloma formation

As the name 'Chronic Granulomatous Disease' implies, aberrant granuloma formation, which involves a complex process comprising various immune cells and inflammatory mediators aimed at containing and neutralizing a persistent threat to the body, is one of the most crucial features of CGD[69,70]. The absence of functional NOX2-driven ROS compromises the antimicrobial function of myeloid cells, such as neutrophils and macrophages, leading to an exaggerated recruitment of these cells to sites of infection. Such an uncontrolled influx of malfunctioning myeloid cells contributes to tissue inflammation and damage, even without proper clearance of pathogens. While granulomas serve as a localized attempt to contain persistent infections, in NOX2-deficient conditions, they may become excessive or dysregulated, exacerbating damage to the host[71]. Uncontrolled expansion of granulomas is highly correlated with an increased number of myeloid cells. In CGD patients, a significant number of myeloid cells, including neutrophils, can be observed not only in the granuloma but also in circulating blood[72]. Such an increase in myeloid cells is induced by excessive growth factors such as GM-CSF and G-CSF, which are crucial for the generation of myeloid cells. According to Bagaitkar et al., G-CSF, a cytokine responsible for the explosive generation of granulocytes, is highly upregulated in NOX2-deficient mice undergoing zymosan-induced lung inflammation, and its neutralization was effective at relieving pulmonary infiltration and reducing quantitative counts of pulmonary neutrophils[50].

2.8. Impacts on adaptive immunity

Although immune alterations caused by impaired NOX2 function mostly focus on myeloid cell deficiencies, due to the nature of NOX2 as a phagocyte oxidase, the influence of NOX2 deficiency extends beyond the realm of innate immunity and significantly impacts adaptive immune responses. NOX2 deficiency adjusts adaptive immunity through various mechanisms, such as altering antigen presentation, inducing excessive T cell activation, and enhancing antibody production[45,47]. As NOX2 controls the antigen-presenting capacities of DCs by modulating phagosomal pH through ROS production, NOX2-deficient DCs exhibit altered capacity in antigen presentation. This may result in impaired cross-presentation of antigens, impaired antigen-presenting capacity, or excessive presentation of autoantigens, depending on the model[52,73,74]. Such adjustments in DC functions eventually alter T cell responses, thereby inhibiting proper helper T cell responses against pathogens or activating autoreactive T cell responses. On the other hand, T cell activation or proliferation can also be adjusted in NOX2-deficient conditions, as NOX-derived ROS can directly modulate signaling pathways involved in T cell activation and proliferation[75-77]. For instance, in the model of asthma, NOX2-null mice featured enhanced Th2 effector functions in a T cell intrinsic manner, independently from the influence of DC[76]. Additionally, emerging studies suggest that NOX2 deficiency may also affect B cell-related adaptive immune responses such as B cell follicle formation and antibody production[78,79]. McCarthy et al. reported that NOX2-deficient mice feature impaired B cell responses, such as germinal center B cell formation or plasma cell differentiation, which is caused by MyD88-dependent influx of detrimental monocytes and neutrophils[80]. Furthermore, Dasoveanu et al. emphasized that NOX2 deficiency leads to defects in monocyte-mediated plasma cell regulation, resulting in excessive secretion of antibodies[81].

2.9. Role in chronic inflammatory diseases

Although CGD is mainly known for its extreme susceptibility to pathogens, CGD patients and NOX2-deficient animal models also feature exacerbated pathogenesis of various non-infectious chronic inflammatory diseases, including inflammatory bowel disease (IBD), rheumatoid arthritis (RA), and asthma. NOX2 deficiency may exacerbate inflammation due to dysregulated ROS signaling, which can lead to neutrophilic inflammation or robust T cell responses against autoantigens[82]. In IBD, NOX2-derived ROS is known to regulate intestinal inflammation and epithelial barrier function, and NOX2 deficiency exacerbates disease severity through uncontrolled inflammation mediated by myeloid cells in the tissue.[83]. In RA, NOX2-derived ROS also play a role in regulating immune responses and joint inflammation. [84]. NOX2 deficiency is reported to exacerbate RA through uncontrolled pro-inflammatory cytokine production from joint neutrophils and altered development of Th17 and Treg cells. [48,85]. Impaired NOX2 function is also associated with the progression of asthma, triggering increased airway inflammation and hyper-responsiveness, highlighting its role in regulating inflammatory pathways in the respiratory system[86,87]. Collectively, these findings underscore the significance of NOX2-derived ROS in maintaining immune homeostasis and suggest that NOX2 deficiency may contribute to the pathogenesis and exacerbation of chronic inflammatory diseases. Autoimmune encephalomyelitis (AE) is another chronic autoimmune inflammation model strongly associated with NOX2. NOX2 controls the expression of various inflammatory cytokines and chemokines, such as GM-CSF, IL-1, IL-6, and the TNF superfamily, in the progression of AE. In NOX2-deficient conditions, such pro-inflammatory cytokines are upregulated by various cells, including inflammatory myeloid cells and autoreactive T cells, consequently exacerbating neuroinflammation[88,89]. Systemic lupus erythematosus (SLE) is another chronic autoimmune inflammatory disease known to be susceptible in CGD patients. Campbell et al. provided evidence that NOX2 deficiency is highly correlated with the pathogenesis of SLE, featuring an increase in antibody-forming plasma cells

and autoreactive antibodies[79]. The role of NOX2 deficiency in the pathogenesis of SLE somehow resembles the pathogenesis of infectious diseases. Hahn et al. reported that impaired NOX2 function causes a diminished capacity for dead cell removal, resulting in poor removal of secondary necrotic cells by monocytes. Impaired clearance of immune-stimulatory necrotic cell compartments leads to autoimmune responses caused by monocytes and neutrophils[90].

2.10. Therapeutic approaches to overcome NOX2-related immune disorders

Diverse approaches to understand the underlying immunologic mechanisms of immune alterations in CGD patients and NOX2-deficient animals have enabled the establishment of various methods effective for controlling disease progression. Therapeutic interventions for NOX2-related immune disorders encompass a multifaceted approach aimed at managing infections, controlling inflammation, and restoring NOX2 function in affected individuals. Antimicrobial prophylaxis stands as a cornerstone in the management of CGD patients, mitigating the risk of recurrent bacterial and fungal infections[91]. Additionally, anti-inflammatory agents play a crucial role in modulating excessive inflammation associated with NOX2 deficiency, thereby alleviating symptoms and preventing tissue damage[92]. These agents may include corticosteroids, nonsteroidal anti-inflammatory drugs (NSAIDs), or biologic agents targeting specific inflammatory pathways[65,93]. Furthermore, hematopoietic stem cell transplantation (HSCT) represents a curative option for CGD patients, aiming to restore NOX2 function by providing healthy donor stem cells capable of generating functional phagocytes with intact NOX2 activity[23]. HSCT has shown promising outcomes in improving immune function and reducing the frequency of infections in CGD patients, although careful patient selection and post-transplant management are essential to ensure optimal outcomes. A recent clinical study suggests potential threats of hematopoietic stem cell inflammation, which is correlated with a high interferon score and

increased frequencies of myeloid progenitors, may be detrimental for the CGD patients receiving HSCT therapies[94]. Lentiviral gene therapy is emerging as a promising approach for the treatment of CGD. This innovative therapeutic strategy involves the delivery of functional copies of the affected gene into the patient's hematopoietic stem cells (HSCs) using lentiviral vectors derived from lentiviruses such as HIV-1[14]. Lentiviral gene therapy in CGD patients aims to restore defective phagocyte function by introducing a functional copy of the CYBB gene, which encodes the major subunit of the NOX2 complex[95]. This novel method is undergoing clinical trials, showing promising results so far, but additional confirmation is still needed.

3. CONCLUSION

NOX2 deficiency profoundly affects various aspects of immune function. This chapter illustrates how impaired NOX2 function causes immune alterations, according to various studies about impaired microbial killing, heightened susceptibility to infections, dysregulated inflammation, altered neutrophil and macrophage function, uncontrolled influx of myeloid cells and granuloma formation, disturbances in adaptive immunity, and the exacerbation of chronic inflammatory diseases. Extensive research conducted in both mouse models and human studies has offered valuable insights into the multifaceted roles of NOX2 in immune regulation. Understanding the intricate mechanisms underlying NOX2 deficiency and its implications for immune function is essential for developing effective therapeutic interventions for CGD patients. Although CGD is a severe disease that causes significant suffering for patients, its harmful effects are not widely known by the public due to its rarity. Further investigation into the role of NOX2 in immune regulation and the development of targeted therapies must continue for the better quality of life for patients. In addition, as NOX2 deficiency features clear alterations in immune responses against pathogens or non-pathogenic stimuli, deep understanding of NOX2-deficient animal models shall become a huge advantage for researchers adapting *in vivo* models for immunologic studies.

Chapter II

Identification of host factors exacerbating Tuberculosis pathogenesis in male NOX2KO mouse model

1. INTRODUCTION

Mycobacterium tuberculosis (Mtb) is the causative agent of Tuberculosis (TB), which remains a significant public health concern worldwide. Approximately, one-quarter of the world's population is estimated to have latent Mtb infection, with 5-10% of these individuals at risk of developing active TB at some point during their lifetime[96]. The factors that influence susceptibility to Mtb are still not completely understood, which hampers the control of this harmful pathogen[97-99]. There is extensive documentation indicating that males are more susceptible to TB than females, and this sexual bias is observed in various animal models including mice and humans[100,101]. The increased TB susceptibility in males is likely due to differences in immune cell functions as well as in their compositions[102,103]. Such host factor-mediated alterations in immune function may directly influence immune responses to Mtb infection. Considering the importance of immunological balance in maximizing anti-TB immunity, both excessive immune suppression or activation might be harmful to the host during TB progression[104-106]. These clues have led to the hypothesis that several host factors, such as biological sex and genetic distributions, which modulate inflammatory responses, may influence TB immunopathogenesis.

The phagocyte NADPH oxidase (NOX2, gp91^{phox}) is located in the lumen of phagosomes. Its primary function is to produce reactive oxygen species (ROS), which play a crucial role in protecting the host against a wide range of pathogens[3,4]. NOX2 also plays a vital role in regulating autophagy and cytokine/chemokine signaling[7-9]. The NOX2 complex is a multimeric enzyme composed of a single catalytic transmembrane heterodimer (gp91^{phox} / p22^{phox}) and four cytosolic subunits (p40^{phox} / p47^{phox} / p67^{phox} / Rac). Among the six major components of NOX2 complex, gp91^{phox} acts as the catalytic core for ROS generation[5,6]. Individuals with impaired NOX2 function may develop chronic granulomatous disease (CGD), characterized by an increased susceptibility to fungal and bacterial infections and impaired inflammation control[10-12]. Since *Nox2* is located at Xp21.1 of the X chromosome, CGD caused by *Nox2* deficiency is inherited in an X-linked recessive manner, primarily affecting young males[13,14]. Furthermore, individuals with X-linked CGD have a heightened vulnerability to mycobacterial infections[38]. This poses significant challenges for TB therapy and prevention in X-linked CGD patients as BCG vaccination cannot be implemented due to the high risks of BCGosis, which is a disseminated mycobacterial infection that can occur following BCG vaccination[16,40,41].

Although phagocyte NADPH oxidase-originated ROS play a crucial role in clearing intracellular pathogens, studies have shown that phagocyte NADPH oxidase deficiencies did not significantly alter mycobacterial growth compared to wild type (WT) animals. According to Cooper et al., p47^{phox}-deficient mice featured increase in lung mycobacterial load from 15 to 30 days post-infection. However, the increase in mycobacterial load was not sustained after 30 days post-infection[107]. Additionally, Olive et al. reported that male and female gp91^{phox}-deficient mice did not show an increase in lung mycobacterial load until 60 days or 20 weeks post-infection[108,109]. These researches give clues that NOX2 deficiency may modulate immune responses against Mtb, independently of ROS-mediated bactericidal effects. Recent studies support this idea as Thomas et al. demonstrated

that gp91^{phox}-deficient mice displayed enhanced inflammation and lung neutrophil infiltration after Mtb challenge, which were mediated by IL-1[3,43].

Dysregulated inflammatory responses and aberrant granuloma formation are hallmark features of X-linked CGD. X-linked CGD patients and NOX2-deficient mice exhibit uncontrolled formation of granulomas, characterized by an excessive influx of phagocytic myeloid cells to the site of infection[69,70]. NOX2-deficient phagocytes, such as macrophages and neutrophils, are major producers of pro-inflammatory cytokines[48,49], which can cause tissue damage[44,50]. Given that NOX2 deficiency-induced X-linked CGD can cause TB susceptibility along with lung hyperinflammation, we hypothesized that Mtb infection would cause uncontrolled inflammation and disruption of immune tolerance in NOX2-deficient mice. As the maintenance of immune tolerance is critical for effective anti-TB immunity, we further hypothesized that controlling the specific immunologic factor which causes Mtb infection-driven hyperinflammation would be crucial for ameliorating TB pathogenesis.

In this study, we established four experimental groups to investigate how two independent host factors (NOX2 deficiency and male sex) can modify the immunological responses against Mtb infection. As both male sex and NOX2 deficiency are risk factors for TB susceptibility, we hypothesized that male *Nox2*$^{-/-}$ mice would exhibit severer TB progression than female *Nox2*$^{-/-}$ mice and male WT mice. Additionally, we anticipated that specific immune factors would contribute to TB pathogenesis and hyperinflammation in male *Nox2*$^{-/-}$ mice, which show a clear correlation to disease progression. Finally, we aimed to discover novel interventions that can effectively regulate these disease-promoting factors in male *Nox2*$^{-/-}$ mice.

We found that male *Nox2*$^{-/-}$ mice exhibited higher levels of lung inflammation and mycobacterial burden compared to female *Nox2*$^{-/-}$ mice and WT mice following Mtb challenge. Male *Nox2*$^{-/-}$ mice also featured elevated production of pro-inflammatory cytokines in the lungs, along with excessive

infiltration of immature neutrophils and reduction of lymphocytes at infection sites. We also dissected the properties of aberrant permissive immature neutrophils, which were distinct from mature neutrophils and constituted the majority of immune cell populations in male *Nox2*$^{-/-}$ mice. By reducing the number of total lung neutrophils or immature neutrophils, we could successfully mitigate TB pathogenesis in male *Nox2*$^{-/-}$ mice. Finally, we determined that G-CSF, rather than other cytokines, is the dominant controller of immature neutrophil generation through *in vivo* neutralization of each cytokine. Collectively, we identified G-CSF driven permissive neutrophils as the key immunologic factor that facilitates TB immunopathogenesis and lung hyperinflammation in male *Nox2*$^{-/-}$ mice. Furthermore, we suggested novel therapeutic interventions targeting immature neutrophils, which might be potential for controlling TB in NOX2-deficient condition.

2. MATERIALS AND METHODS

2.1. Ethics statements and study approval

All animal experiments followed the regulations set by the Korean Food and Drug Administration. The Ethics Committee and Institutional Animal Care and Use Committee (2019-0174; C57BL/6N, *Nox2*$^{-/-}$, 2022-0140; C57BL/6N, *Nox2*$^{-/-}$) at Yonsei University Health System (Seoul, Korea) granted approval for each experimental protocol.

2.2. Mice

Six- to seven-week-old female and male C57BL/6N mice were obtained from Japan SLC, Inc. (Shizuoka, Japan). Six- to seven-week-old female and male *Nox2*$^{-/-}$ mice were provided by Dr. Yun Soo Bae (Ewha Womans University, Seoul, South Korea). The mice were housed in a specific pathogen-free (SPF) environment with barriered conditions at the Yonsei University Medical Research Center SPF facility.

2.3. Bacterial culture and infection protocols

Purchase of the Mtb K strain, mycobacterial culture, and aerosol infection processes were executed according to the referenced studies[110,111]. The mycobacteria were cultured in 7H9 broth supplemented with 10% oleic acid-albumin-dextrose-catalase (OADC; Difco Laboratories, MD) and 2 μg/ml of mycobactin J (Allied Monitor, Fayette, MO) for 4 weeks at 37℃. Following cultivation, all bacteria were washed three times with 10 mM phosphate-buffered saline (PBS; pH 7.4). Bacterial cell pellets were collected after centrifugation, and small aliquots were stored at -80℃ until use. The Mtb K strain used for *in vivo* challenges was PDIM positive. YFP vectors for the generation of YFP^{+} Mtb K strain were kindly gifted by Dr. Christopher Sassetti. In order to

deliver bacteria to the lungs of each mouse, all mice were exposed to at least 200 viable mycobacteria in an inhalation chamber for 60 minutes.

2.4. *In vivo* treatments for neutrophil control

From two weeks post-infection, 250 μg/mouse of anti-Ly6G mAb (clone: 1A8, Bio X Cell, West Lebanon, NH, USA), 200 μg/mouse of anti-IL-1R mAb (clone: JAMA-147, Bio X Cell, West Lebanon, NH, USA), 200 μg/mouse of anti-IFN-γ mAb (clone: H22, Bio X Cell, West Lebanon, NH, USA), and 250 μg/mouse of anti-IL-17A mAb (clone: 17F3, Bio X Cell, West Lebanon, NH, USA) mAb were intraperitoneally administered. The antibodies were diluted in PBS and administered three times a week for a total duration of two weeks. From one-week post-infection, 30 μg/mouse of anti-G-CSF mAb (clone: #67604, R&D Systems, Minneapolis, MN, USA), 200 μg/mouse of anti-IL-1R mAb (clone: JAMA-147, Bio X Cell, West Lebanon, NH, USA), 400 μg/mouse of anti-IL-6 mAb (clone: MP5-20F3, Bio X Cell, West Lebanon, NH, USA), 200 μg/mouse of anti-IL-1α mAb (clone: ALF-161, Bio X Cell, West Lebanon, NH, USA), and 200 μg/mouse of anti-IL-1β mAb (clone: B122, Bio X Cell, West Lebanon, NH, USA) were intraperitoneally administered. The antibodies were diluted in PBS and administered three times a week for a total duration of three weeks. Rat IgG2a, rat IgG1, Armenian hamster IgG, and mouse IgG1 isotype control antibodies were purchased from Bio X Cell (West Lebanon, NH, USA). Isotype control antibodies were administered to control mice in correspondence with the original antibodies. From one-week post-infection, 20 μg/mouse of AM80 (Sigma-Aldrich, St. Louis, MO, USA) was orally administered. AM80 was diluted in PBS and administered three times a week for a total duration of three weeks.

2.5. Antibodies and flow cytometry

Flow cytometric analysis of immune cells was conducted using the subsequent antibodies. LIVE/DEAD Fixable Near-IR Dead Cell Stain Kit, Green Dead Cell Stain Kit, and Aqua Dead Cell Stain Kit were purchased from Molecular Probes (Carlsbad, CA, USA). Brilliant violet (BV) 605-conjugated mAb against Thy1.2 and CD19; Allophycocyanin (APC)-conjugated mAb against CD45R (B220); BV 421-conjugated mAb against CD45; APC-R700-conjugated mAb against Siglec-F; Fluorescein isothiocyanate (FITC)-conjugated mAb against CD95 (FAS); BV 786-conjugated mAb against CXCR2; and V450- conjugated mAb against Ly6G were purchased from BD Bioscience (San Jose, CA, USA). Phycoerythrin (PE)-conjugated mAb against CXCR2, CD64, IFN-γ, and GL7; Peridinin chlorophyll (PerCP)-Cy5.5-conjugated mAb against CD11b; APC-Cy7-conjugated mAb against MHC-II; Alexa fluor 700-conjugated mAb against CD62L; and PE-Dazzle conjugated mAb against CD11c were purchased from Biolegend (San Diego, CA, USA). Surface and intracellular staining processes were executed according to the referenced study[112].

2.6. Preparation of single cell suspensions and immune cell analysis

Four weeks post-infection, the mice were euthanized via inhalation of carbon dioxide and then underwent an autopsy. The mouse lungs were perfused before undergoing flow cytometry analysis. Using the methods described in previous studies[113,114], single-cell suspensions were obtained from the entire lung tissue. These cells were then stained with the mAbs mentioned in the previous section and subjected to flow cytometry analysis.

2.7. Measurement of cytokines

For the analysis of lung cytokines, lung lysates from the autopsied mice were collected, homogenized, dissolved into PBS, and then stored in a -80℃ freezer. For the analysis of T cell cytokines, lung single cell suspensions were stimulated with two different Mtb antigens, PPD and

ESAT-6 according to the referenced studies[112,114]. To detect cytokines, sandwich enzyme-linked immunosorbent assay (ELISA) and LEGENDplex kits were utilized. Briefly, mouse G-CSF and IL-1α ELISA kits were purchased from R&D Systems (Minneapolis, MN, USA). Mouse IFN-γ, IL-1β, IL-17A, and IL-5 ELISA kits were purchased from Invitrogen (San Diego, CA, USA). Mouse IL-10 ELISA kit, LEGENDplex mouse B cell panel (for the detection of TNF-α, IL-4, IL-6, BAFF, and TGF-β), and LEGENDplex mouse inflammation panel (for the detection of IL-1α, IL-1β) were purchased from Biolegend (San Diego, CA, USA).

2.8. Quantification of lung inflammation and mycobacterial CFU

The lungs and spleens of Mtb infected mice were harvested four weeks post-infection. The right superior lobes of the lungs were kept in 10% formalin overnight for preservation and later embedded in paraffin. To perform histopathologic analysis, the lungs were sectioned at 4-5 μm and stained with hematoxylin and eosin (H&E). To quantify pulmonary inflammation in each mouse, we employed Adobe Photoshop (Adobe, San Jose, California) and ImageJ (National Institutes of Health, USA) programs, following a previously described reference[115]. The complete lung lesion image was isolated using Adobe Photoshop and saved as a separate file. Another image, identical in size to the original lung image but filled with black, was also saved as a separate file. These images were then opened in ImageJ. By using the 'Split Channels' function, the image from the green channel was processed to calculate the size of the area showing green positivity, which was originally purple-blue due to H&E staining. The black-colored image was analyzed through the green channel in the same manner to calculate the size of the entire lung lesion. The 'inflamed area (%)' value, which indicates the proportion of inflamed tissue relative to the entire lung lesion, was computed by dividing the green positivity values of the first image by the green positivity values of the black-colored image. Subsequently, the actual size of the inflamed lesion was calculated by determining

the pixel values in Adobe Photoshop. The pixel value corresponding to a single millimeter was calculated based on a 2mm scale bar included in each images. The pixel value for the entire lung lesion was also enumerated, and the value was divided by the square of the pixel value representing one millimeter to quantify the size (mm^2) of each lung lesion. By multiplying the inflamed area (%) values by the total lung sizes (mm^2) for each sample, we were able to precisely enumerate the exact size of each inflamed area (mm^2). To enumerate mycobacterial growth, lung and spleen tissues were plated onto Middlebrook 7H10 agar (Becton Dickinson, Franklin Lakes, NJ, USA) after homogenization, following preparation methods from previous studies[113,116]. After a four-week incubation period at 37℃, mycobacterial colonies were counted.

2.9. Neutrophil purification and assessment of mycobacterial permissiveness

MACS magnetic cell sorting kit including anti-Ly6G magnetic beads and LS MACS columns (Miltenyi Biotec, Bergisch Gladbach, Germany) was used to enrich $Ly6G^+$ cells from the lungs of Mtb-infected mice. The manufacturer's protocols were followed. After separating $Ly6G^+$ lung cells, the cells were treated with Triton X-100 (Sigma-Aldrich, St. Louis, MO, USA) and plated onto Middlebrook 7H10 agar (Becton Dickinson, Franklin Lakes, NJ, USA). After a three-week incubation period at 37℃, mycobacterial colonies were counted.

2.10. Statistical analyses

The results were presented as the mean ± standard deviation (SD). To analyze the significance of differences between two selected groups, One-way ANOVA and Mann-Whitney U test were conducted using GraphPad Prism version 8 for Windows (GraphPad Software, La Jolla, CA, USA, www.graphpad.com). The statistical significance was determined using the following definitions: *n.s.*: not significant, $*p < 0.05$, and $**p < 0.01$. Correlation analysis and unpaired t-test were

conducted using GraphPad Prism, and the correlation coefficients and p-values were reported for each graph. Flowjo V10 (Flowjo, Ashland, OR, USA) was employed to perform t-distributed stochastic neighbor embedding (t-SNE) analysis.

3. RESULTS

3.1. Male *Nox2*$^{-/-}$ mice feature increased mycobacterial burden and lung hyperinflammation following aerosol infection with the Mtb K strain

Female WT, male WT, female *Nox2*$^{-/-}$, and male *Nox2*$^{-/-}$ mice were aerosol-infected with the Mtb K. At four weeks post-infection, the mice were autopsied to assess the severity of TB and immune function **(Figure 1A)**. The mice were euthanized at the four weeks post-infection time point, when the increases in lung bacterial load **(Figure 2A)** and neutrophil infiltration **(Figure 2B)** - key pathological features of Mtb-infected *Nox2*$^{-/-}$ mice[3,43] - reached their peak. These measures began to increase from two weeks post infection, peaked at four weeks post-infection, and subsequently decreased until twelve weeks post-infection in *Nox2*$^{-/-}$ mice. Male *Nox2*$^{-/-}$ mice showed the highest lung bacterial load, spleen bacterial load, and lung inflammation. Female *Nox2*$^{-/-}$ mice featured the second-highest severity, while male and female WT mouse groups were ranked as 3rd and 4th, respectively **(Figure 1B, 1C)**. Pro-inflammatory cytokines including IFN-γ, IL-1α, IL-1β, IL-17A, IL-6, TNF-α, G-CSF, and BAFF were significantly upregulated in the lungs of male *Nox2*$^{-/-}$ mice **(Figure 1D)**. Conversely, anti-inflammatory cytokines including IL-4, IL-5, and TGF-β were not upregulated in the lungs of male *Nox2*$^{-/-}$ mice, although IL-10 was significantly upregulated **(Figure 1E)**. This indicates that NOX2 deficiency plays a significant role in accelerating TB immunopathogenesis, as both male and female *Nox2*$^{-/-}$ mice feature exacerbated TB progression. Furthermore, we also found that male sex additionally promotes TB pathogenesis, as indicated by severer TB progression in male *Nox2*$^{-/-}$ mice.

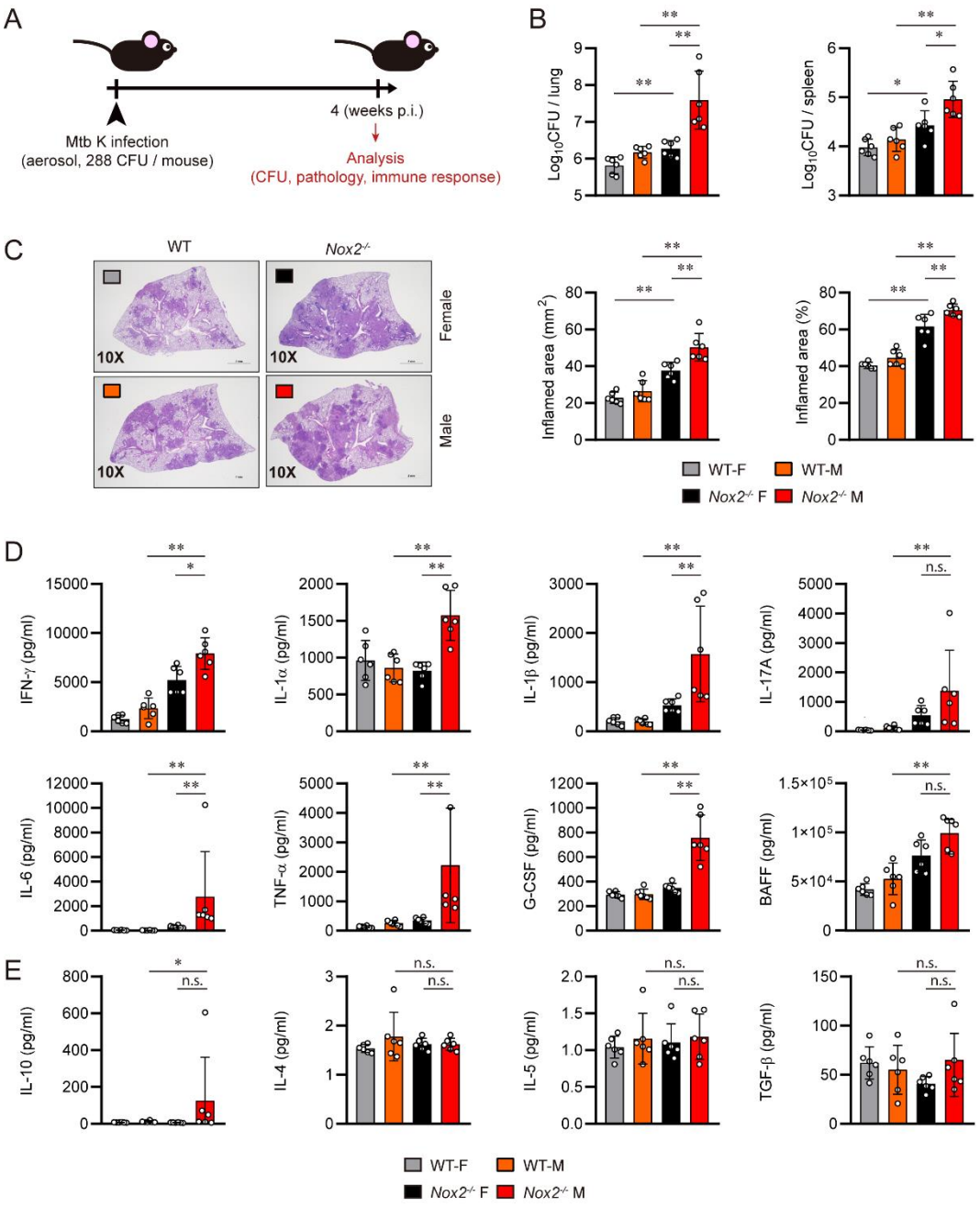

Figure 1. Male *Nox2*$^{-/-}$ mice featured severe lung hyperinflammation and increased bacterial load upon Mtb infection. (A) Experimental design for *in vivo* analysis of TB susceptibility. Six to seven-week-old female WT, male WT, female *Nox2*$^{-/-}$, and male *Nox2*$^{-/-}$ mice (n = 6 per group) were aerosol-infected with Mtb K strain. At four weeks post-infection, all mice were autopsied, and immunological analysis, bacterial counting, and histopathological analysis were conducted (indicated by red arrow). Initial CFU = 288. **(B)** Mycobacterial CFUs in the lungs and spleens of each group at four weeks post-infection were analyzed by calculating the number of colonies and presented in bar graphs. **(C)** H&E staining was performed on the superior lobes of the right lung at four weeks post-infection to visualize the gross lung pathology. The inflamed area of the H&E-stained samples was quantified in terms of percentage and square millimeters and presented in bar graphs. **(D)** IFN-γ, IL-1α, IL-1β, IL-17A, IL-6, TNF-α, G-CSF, and BAFF levels in Mtb-infected mouse lung lysates were measured by ELISA and LEGENDplex. **(E)** IL-10, IL-4, IL-5, and TGF-β levels in Mtb-infected mouse lung lysates were measured by ELISA and LEGENDplex. The cytokine levels are presented in bar graphs. The experiment was conducted twice. The data are presented as the mean ± SD of six mice in each group. The significance of differences was determined, using the One-way ANOVA test. *n.s.*, not significant. *$p < 0.05$, **$p < 0.01$.

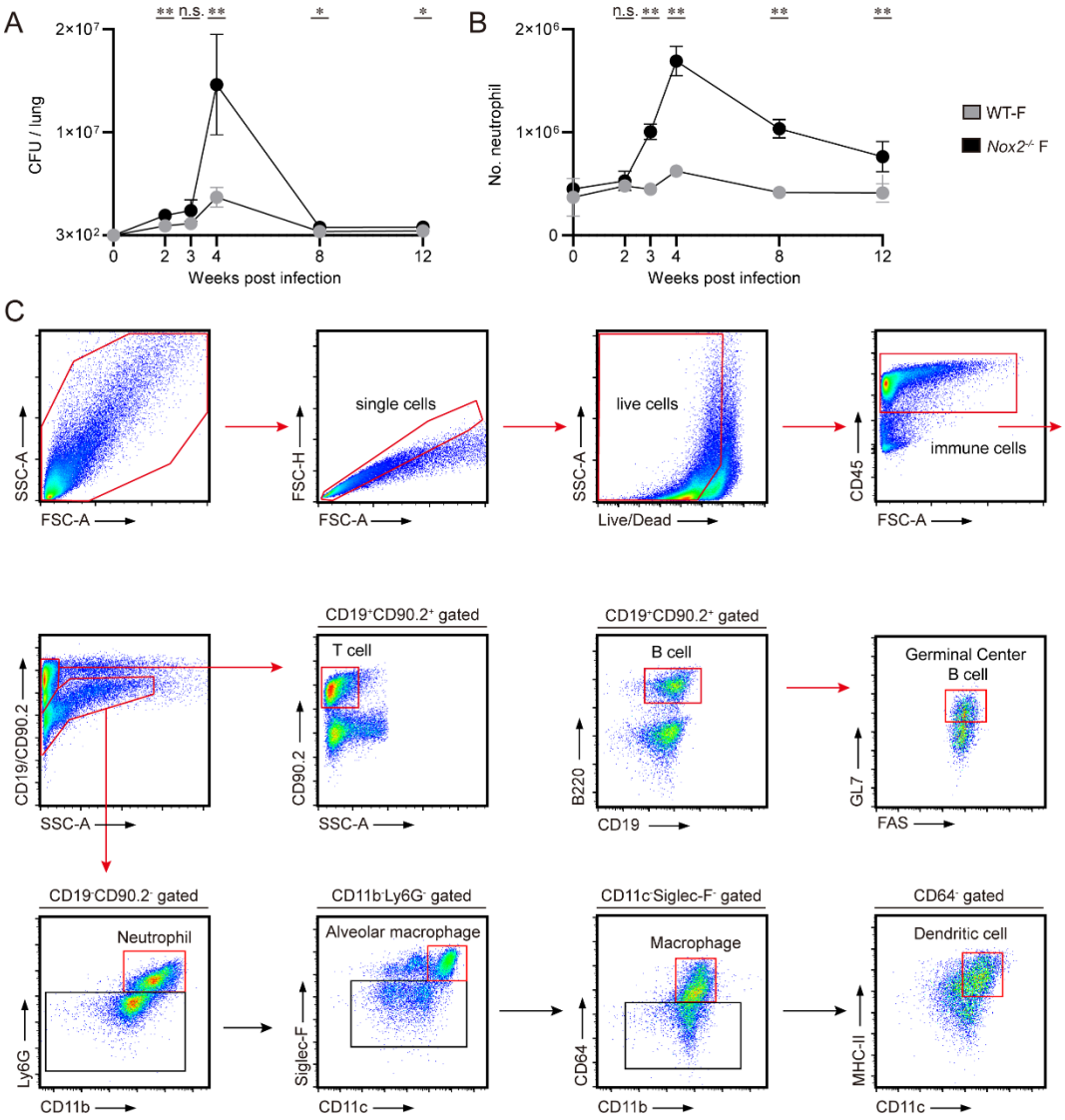

Figure 2. The gating strategy for immune cell populations and the kinetics time-course data of pulmonary CFUs and neutrophils are provided. (A) Pulmonary CFUs of female WT and *Nox2*$^{-/-}$ mice were enumerated in a time-course dependent manner. six-week old female WT and *Nox2*$^{-/-}$ mice (n = 5 per group) were aerosol infected with Mtb K strain. Mycobacterial CFUs in the lungs of Mtb infected mice were calculated at 0, 2, 3, 4, 8, and 12 weeks post-infection. Initial CFU = 373. The experiment was conducted once. **(B)** Pulmonary neutrophil counts were calculated at 0, 2, 3, 4, 8, and 12 weeks post-infection. The experiment was conducted once. The significance of differences was determined, using the One-way ANOVA and Mann-Whitney U test. *n.s.*, not significant. *$p < 0.05$. **$p < 0.01$**. (C)** The gating strategy for immune cell populations is presented as flow cytometry plots. Firstly, Live cells stained with the LIVE/DEAD Aqua Dead Cell Stain Kit were gated among single cells. $CD45^+$ immune cells were then gated in order to investigate lung immune cell compositions. Among $CD45^+$ immune cells, $CD19^+CD90.2^+$ SSC-A^{lo} lymphocytes and $CD19^-CD90.2^-$SSC-A^{hi} myeloid cells were discriminated. Lymphocytes consisted of $CD90.2^+$ T cells, $CD19^+B220^+$ B cells, and $CD19^+B220^+GL7^+FAS^+$ germinal center B cells. Myeloid cells consisted of $CD11b^+Ly6G^+$ neutrophils, $CD11c^+$Siglec-F^+ alveolar macrophages, $CD11b^+CD64^+$ macrophages, and $CD11c^+$MHC-II^+ dendritic cells.

3.2. Pulmonary infiltration of neutrophils and loss of B lymphocytes are correlated with TB pathogenesis of male *Nox2*$^{-/-}$ mice

To determine which immune cell population is associated with dysregulated pro-inflammatory cytokine production, live lung cell compositions of Mtb infected mice were examined according to the attached flow cytometry gating strategy **(Figure 2C)**. Male *Nox2*$^{-/-}$ mice exhibited the highest numbers and percentages of CD11b^{+}Ly6G^{+} lung neutrophils, while female WT mice featured the lowest among the four groups **(Figure 3A)**. On the other hand, male *Nox2*$^{-/-}$ mice showed a significant reduction in pulmonary CD90.2^{+} T cell percentages **(Figure 3B),** CD19^{+}B220^{+} B cell counts **(Figure 3C)**, and CD19^{+}B220^{+}GL7^{+}FAS^{+} Germinal Center B cell counts **(Figure 3D)**.

The disparity in TB progression peaked at four weeks post-infection, as male *Nox2*$^{-/-}$ mice exhibited significantly increased lung bacterial loads and pulmonary neutrophil counts at this time, compared to male WT mice and female *Nox2*$^{-/-}$ mice. The increase in lung CFU (Colony-forming unit) s and pulmonary neutrophils in male *Nox2*$^{-/-}$ mice began between two and three weeks post-infection and reached its maximum at four weeks post-infection. Interestingly, the disparity in pulmonary neutrophil counts between male *Nox2*$^{-/-}$ mice and other groups was more pronounced than the differences in lung CFUs at two and three weeks post-infection, as the latter did not show significant statistical differences, suggesting that the influx of pulmonary neutrophils occurs earlier than the increase in lung bacterial load **(Figure 3E)**. T cell responses against mycobacterial antigen stimulations were also examined, as IFN-γ producing CD4^{+} T cells take crucial roles in anti-TB immunity[117,118]. Although male *Nox2*$^{-/-}$ mice featured the most exacerbated TB progression among the four groups, T cell responses against Mtb antigens were strongly maintained **(Figure 4)**. The numbers of pulmonary CD11c^{+}Siglec-F^{+} alveolar macrophages, CD11b^{+}CD64^{+} macrophages, and CD11c^{+}MHCII^{+} dendritic cells were also significantly reduced in male *Nox2*$^{-/-}$ mice **(Figure 5)**. The immune cell dynamics in the lungs of mice infected with Mtb were visually represented using pie-

charts and t-SNE plots. We observed that neutrophils, B cells, and T cells comprise the majority of pulmonary immune cells **(Figure 3E)**. Furthermore, we found strong correlations between these immune cell populations and TB severity. The percentages of neutrophils displayed a strong positive correlation with TB severity, with high correlation coefficients and low p-values. Conversely, the percentages of T cells did not exhibit a significant correlation with TB severity, while the percentages of B cells demonstrated a reverse correlation with TB severity. The loss of pulmonary B cells also showed a significant negative correlation with neutrophil infiltration **(Figure 6).** Thus, we hypothesized that TB susceptibility of male *Nox2*$^{-/-}$ mice is highly associated with the increase of pulmonary neutrophils

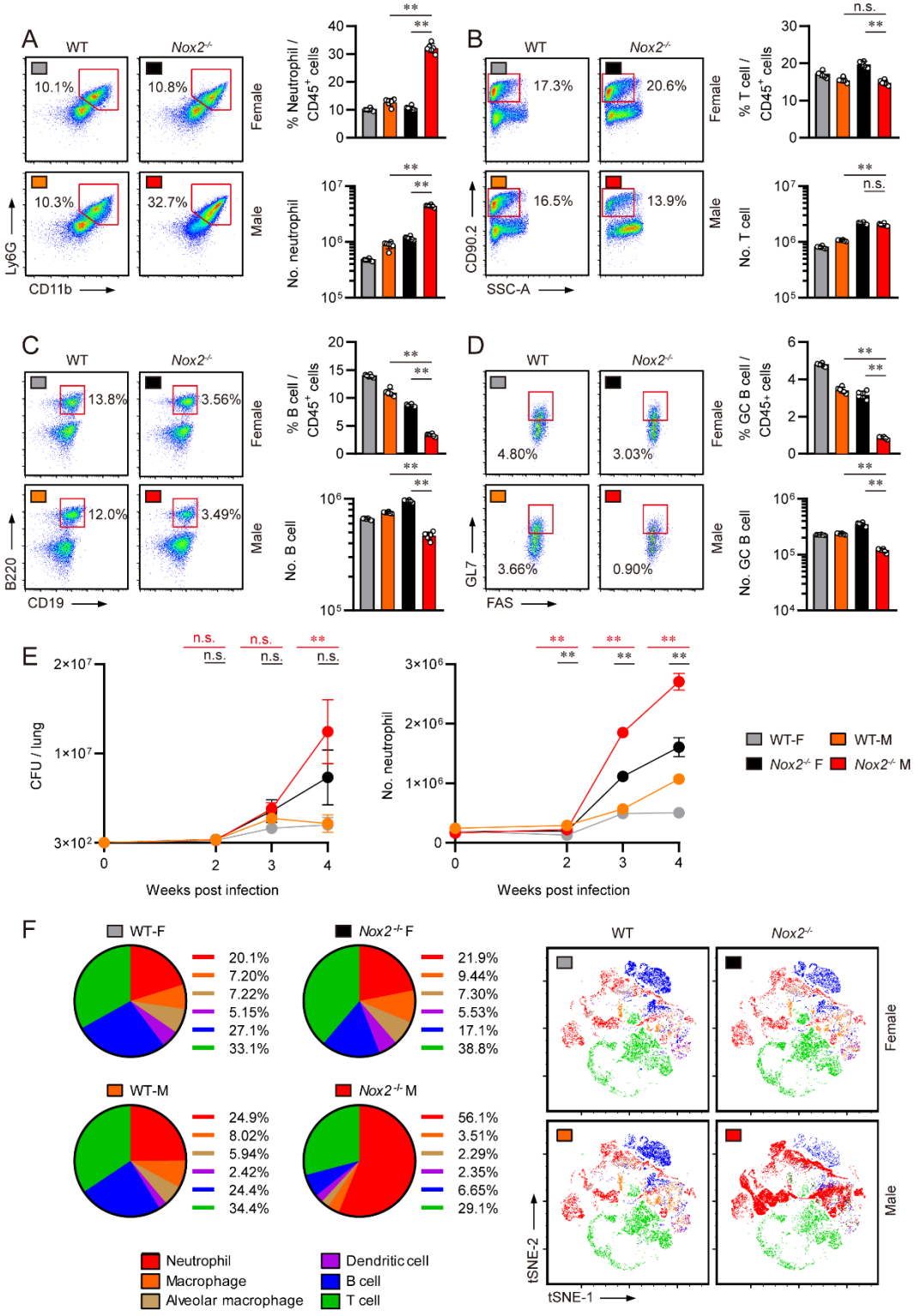

Figure 3. Neutrophils are increased in the lungs of Mtb infected male *Nox2*$^{-/-}$ mice while B cells are diminished. Pulmonary **(A)** CD11b^{+}Ly6G^{+} neutrophil, **(B)** CD90.2^{+} T cell, **(C)** CD19^{+} B220^{+} B cell, and **(D)** CD19^{+} B220^{+} GL7^{+} FAS^{+} Germinal Center B cell populations of Mtb-infected mice at four weeks post-infection. The percentages of each immune cell among lung CD45^{+} cells and total cell counts are presented in bar graphs. **(E)** Pulmonary CFUs and neutrophil counts of female WT, male WT, female *Nox2*$^{-/-}$, and male *Nox2*$^{-/-}$ mice were enumerated in a time-course dependent manner. Six-week old mice (n = 5 per group) were aerosol infected with Mtb K strain. The number of lung neutrophils were calculated at 0, 2, 3, and 4 weeks post-infection. Red bars and symbols represent statistical analysis between male *Nox2*$^{-/-}$ mice and male WT mice. Black bars and symbols represent statistical analysis between male *Nox2*$^{-/-}$ mice and female *Nox2*$^{-/-}$ mice. Initial CFU = 300. The experiment was conducted once. The data are presented as the mean ± SD of five or six mice in each group. The significance of differences was determined, using the One-way ANOVA test. *n.s.*, not significant. $^{**}p < 0.01$. **(F)** The compositions of the six major lung immune cell populations in Mtb-infected mice are presented in pie charts and t-SNE plots. The six major immune cells consist of neutrophils (red), macrophages (orange), alveolar macrophages (bright brown), dendritic cells (purple), B cells (blue), and T cells (green). The percentages of each immune cell among the sum of the six major immune cells are presented in pie charts.

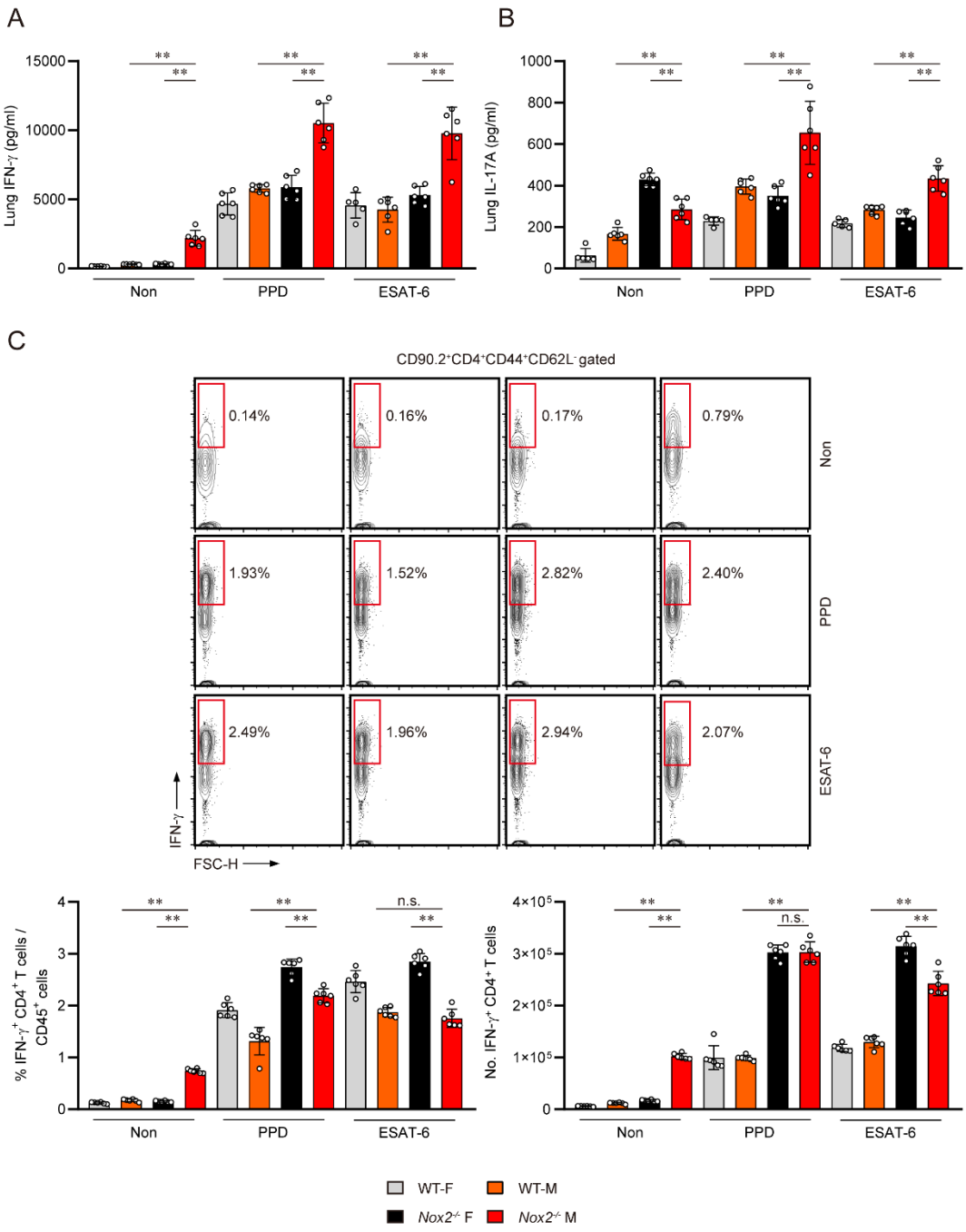

Figure 4. Pulmonary T cells of male *Nox2*$^{-/-}$ mice maintained strong responses against mycobacterial antigens. Live lung cell suspensions were cultured with or without the mycobacterial antigens ESAT-6 and PPD for 8 hours. **(A)** Lung IFN-γ levels and **(B)** Lung IL-17A levels after mycobacterial antigen stimulus are presented in bar graphs. **(C)** IFN-γ positive CD90.2^{+} CD4^{+} CD44^{+} CD62L^{+} effecter T cell populations are presented in bar graphs and flow cytometry plots. The data are presented as the mean ± SD of six mice in each group. The significance of differences was determined, using the One-way ANOVA test. *n.s.*, not significant. ***p* <0.01.

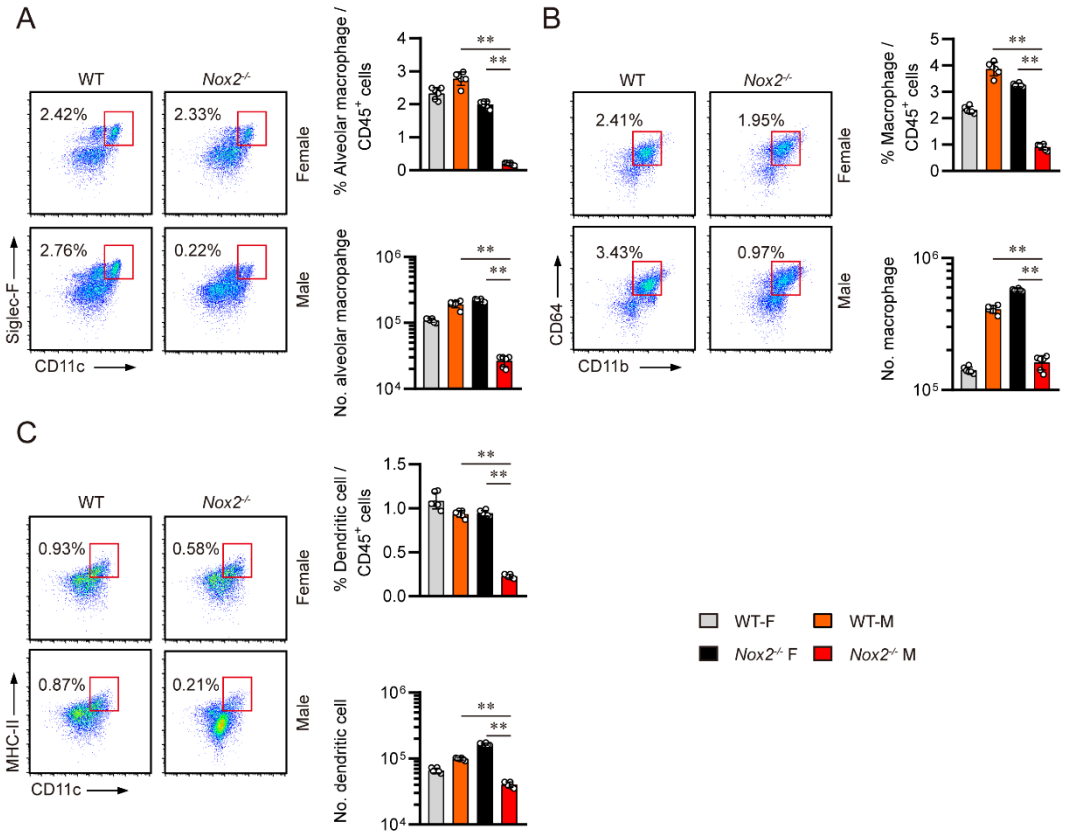

Figure 5. Alveolar macrophages, macrophages, and dendritic cells were reduced in the lungs of Mtb infected male *Nox2*$^{-/-}$ mice. Pulmonary **(A)** CD11c^{+}Siglec-F^{+} alveolar macrophages, **(B)** CD11b^{+}CD64^{+} macrophages, and **(C)** CD11c^{+}MHCII^{+} dendritic cell populations of Mtb-infected mice at four weeks post-infection. The percentages of each immune cell among lung CD45^{+} cells and total cell counts are presented in bar graphs. The data are presented as the mean ± SD of six mice in each group. The significance of differences was determined, using the One-way ANOVA test. $^{**}p < 0.01$.

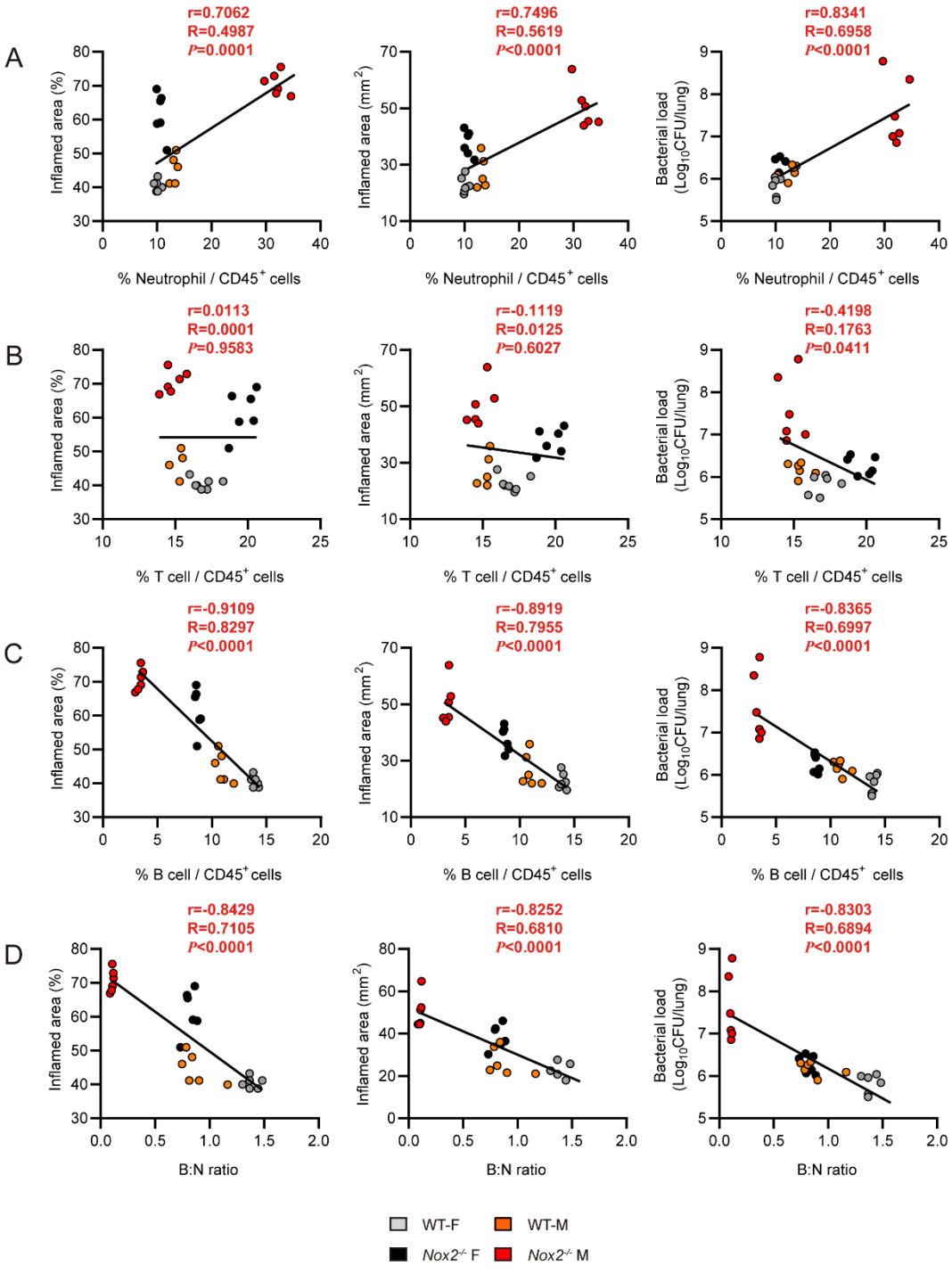

Figure 6. TB severity featured strong correlation to increase of lung neutrophils and decrease of lung B cells. The percentages of **(A)** neutrophils, **(B)** T cells, and **(C)** B cells among lung $CD45^+$ cells were individually correlated with inflamed lung percentages, inflamed lung area, and lung bacterial loads of each mouse and presented in correlation graphs. Additionally, **(D)** the ratio of pulmonary B cells to neutrophils (B:N ratio) was also individually correlated with inflamed lung percentages, inflamed lung area, and lung bacterial loads of each mouse and presented in correlation graphs. The significance of differences was determined by unpaired t-test and correlation analysis, featuring r and p values of each correlation.

3. Pulmonary neutrophils of Mtb infected male *Nox2*$^{-/-}$ mice are predominantly composed of aberrant CD11b^{int}Ly6G^{int}CXCR2^{lo}CD62L^{lo} permissive immature neutrophils

It was not only the number of neutrophils that were altered in male *Nox2*$^{-/-}$ mice. Pulmonary neutrophils of male *Nox2*$^{-/-}$ mice featured CD11b^{int}Ly6G^{int} phenotypes, while neutrophils of other mouse groups featured CD11b^{hi}Ly6G^{hi} phenotypes. Atypical lung neutrophils of male *Nox2*$^{-/-}$ mice showed relatively lower expression of CD11b, Ly6G, Ly6C, CXCR2, and CD62L compared to WT neutrophils, along with higher expression of CXCR4 **(Figure 7A)**. We categorized CD11b^{+}Ly6G^{+} pulmonary neutrophils into two distinct populations based on CXCR2 expression. According to previous studies, Ly6G^{hi} or CXCR2^{hi} lung neutrophils are categorized as mature neutrophils, whereas Ly6G^{int} or CXCR2^{lo} lung neutrophils are categorized as immature neutrophils[119-122]. We revealed that CD11b^{+}Ly6G^{+} pulmonary neutrophils of Mtb infected mice are consisted of CXCR2^{hi} and CXCR2^{lo} populations. Moreover, we figured out that CXCR2^{hi} mature pulmonary neutrophils highly expressed CD62L, while CXCR2^{lo} immature neutrophils featured low expression of CD62L through our own gating strategy **(Figure 7B)**. The majority of *Nox2*$^{-/-}$ pulmonary neutrophils were CXCR2^{lo}CD62L^{lo} immature neutrophils, whereas WT pulmonary neutrophils comprised both immature and mature neutrophils. This suggests that the excessive accumulation of pulmonary neutrophils in male *Nox2*$^{-/-}$ mice is primarily mediated by immature neutrophil-specific lung infiltration **(Figure 7C)**. We also analyzed neutrophil profiles from uninfected WT and *Nox2*$^{-/-}$ mice. The number of pulmonary total and immature neutrophils **(Figure 8A, 8B)**, as well as bone marrow (BM) total and immature neutrophils **(Figure 8C, 8D)**, were not increased in uninfected male *Nox2*$^{-/-}$ mice. Therefore, we concluded that the extreme pulmonary infiltration of CXCR2^{lo}CD62L^{lo} immature neutrophils is initiated by the pathogenic stimulus triggered by Mtb infection. CXCR2^{lo}CD62L^{lo} immature lung neutrophils displayed significantly lower expression levels of CD11b and Ly6G, which are major activation markers of neutrophils.

They also featured lower FSC-A and SSC-A values compared to mature lung neutrophils, indicating that $CXCR2^{lo}CD62L^{lo}$ neutrophils are characterized by their smaller size and reduced granularity when compared to mature neutrophils **(Figure 7D)**. To evaluate the permissiveness of pulmonary neutrophils, we isolated lung neutrophils from Mtb-infected mice and quantified intracellular bacterial counts. *Nox2*$^{-/-}$ pulmonary neutrophils, predominantly consisted of $CXCR2^{lo}CD62L^{lo}$ immature neutrophils, exhibited higher mycobacterial permissiveness compared to WT pulmonary neutrophils **(Figure 7E).** To examine if $CXCR2^{lo}CD62L^{lo}$ immature neutrophils are more permissive than $CXCR2^{hi}CD62L^{hi}$ mature neutrophils, we infected male WT and *Nox2*$^{-/-}$ mice with YFP-expressing Mtb K strain. At four weeks post-infection, the mice were euthanized, and neutrophil permissiveness was evaluated using flow cytometry analysis **(Figure 9A)**. We noted that neutrophils constituted the majority of YFP^+ cells in male *Nox2*$^{-/-}$ mice, and the number of Mtb-containing neutrophils were also increased. The mean fluorescence intensity (MFI) values of YFP in *Nox2*$^{-/-}$ lung neutrophils were substantially higher than those in WT mice, indicating increased mycobacterial permissiveness of *Nox2*$^{-/-}$ lung neutrophils **(Figure 9B)**. Both immature and mature Mtb-containing neutrophil populations were enlarged in *Nox2*$^{-/-}$ mice. Notably, immature neutrophils displayed considerably higher YFP MFI values than mature neutrophils, suggesting their increased permissiveness to Mtb **(Figure 9C)**. Conversely, the proportion of YFP^+ alveolar macrophages was lower in male *Nox2*$^{-/-}$ mice, and there was no significant difference in the number of YFP^+ alveolar macrophages between WT and *Nox2*$^{-/-}$ mice, although these cells exhibited relatively higher YFP MFI values compared to mature neutrophils **(Figure 9D)**. The number of YFP^+ macrophages was elevated in *Nox2*$^{-/-}$ mice, but their YFP MFI values were relatively lower than those of immature neutrophils and alveolar macrophages **(Figure 9E)**. In conclusion, we hypothesized that immature neutrophils are the primary permissive phagocytes in male *Nox2*$^{-/-}$ mice, considering both their dominance in population and their significant bacterial

permissiveness as indicated by MFI values. These results suggest that permissive immature lung neutrophils may play a key role in driving TB pathogenesis and lung hyperinflammation in male *Nox2*$^{-/-}$ mice.

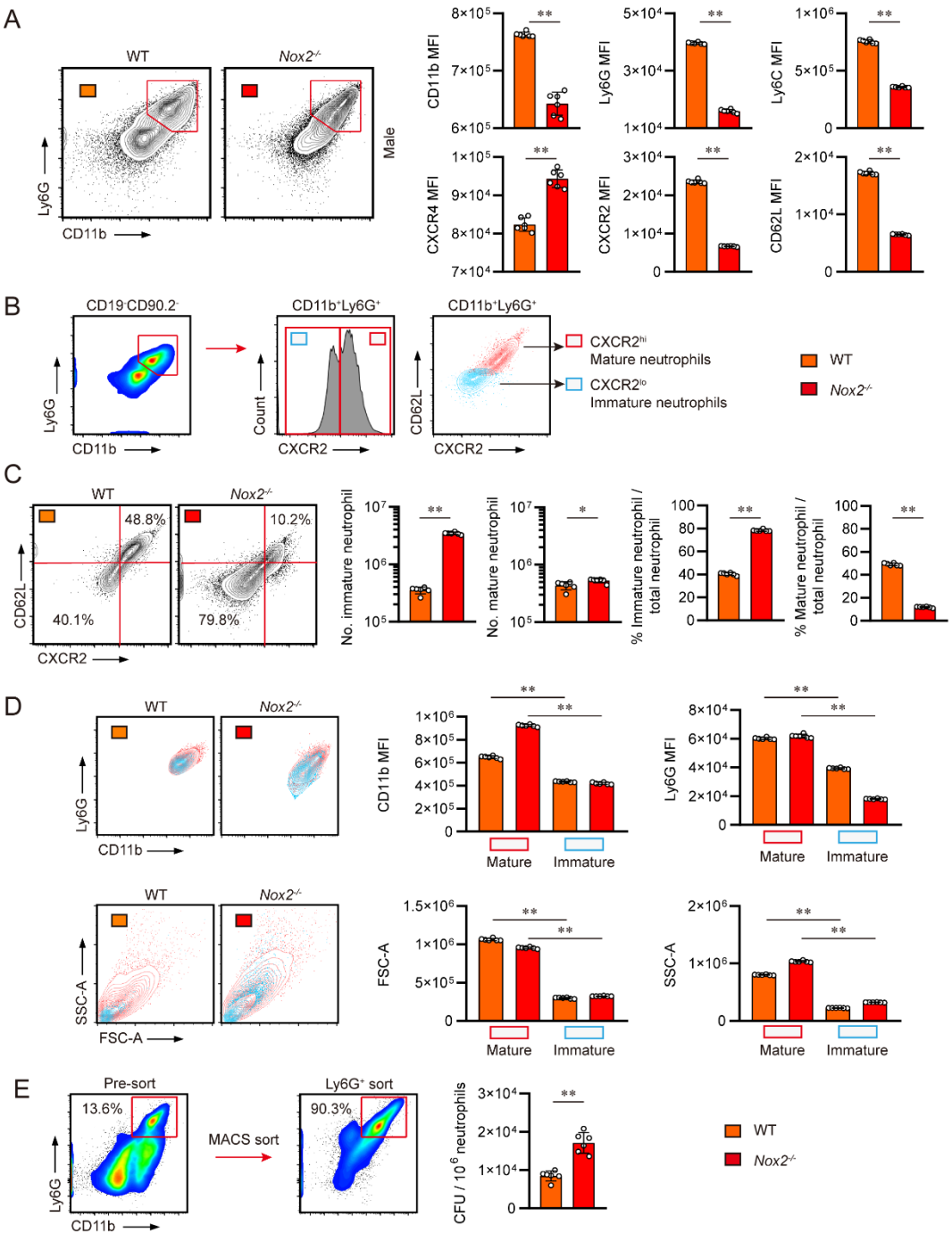

Figure 7. CD11b^{int}Ly6G^{int} CXCR2^{lo}CD62L^{lo} immature neutrophils were dominant among the pulmonary neutrophils of Mtb infected male *Nox2*$^{-/-}$ mice. (A) The expression levels of CD11b, Ly6G, Ly6C, CXCR4, CXCR2, and CD62L on CD11b^{+}Ly6G^{+} neutrophils in the lungs of Mtb-infected mice at four weeks post-infection are presented. The mean fluorescent intensity (MFI) values of each molecule are presented in bar graphs. **(B)** The gating strategy used to distinguish immature and mature pulmonary neutrophils. CD11b^{+}Ly6G^{+} neutrophils were classified into CXCR2^{hi} mature neutrophils (red) and CXCR2^{lo} immature neutrophils (bright blue). **(C)** CD62L expression levels of CXCR2^{hi} neutrophils and CXCR2^{lo} neutrophils are presented into contour plots, demonstrating that mature neutrophils feature CXCR2^{hi}CD62L^{hi} phenotypes while immature neutrophils feature CXCR2^{lo}CD62L^{lo}phenotypes. The numbers and percentages of immature and mature neutrophils among total pulmonary neutrophils in each group are presented in bar graphs, along with flow cytometry plots. **(D)** The expression levels of CD11b and Ly6G on mature and immature pulmonary neutrophils are presented in flow cytometry plots and bar graphs, along with FSC-A and SSC-A values of mature and immature neutrophils. **(E)** The purity of mouse lung neutrophils after Ly6G specific magnetic sorting and their bacterial permissiveness are presented in flow cytometry plots and bar graphs. Equal numbers of WT and *Nox2*$^{-/-}$ lung neutrophils were lysed and plated onto 7H10 agar plates to enumerate bacterial permissiveness. The data are presented as the mean ± SD of six mice in each group. The significance of differences was determined, using the One-way ANOVA test and Mann-Whitney U test. *$p < 0.05$, **$p < 0.01$.

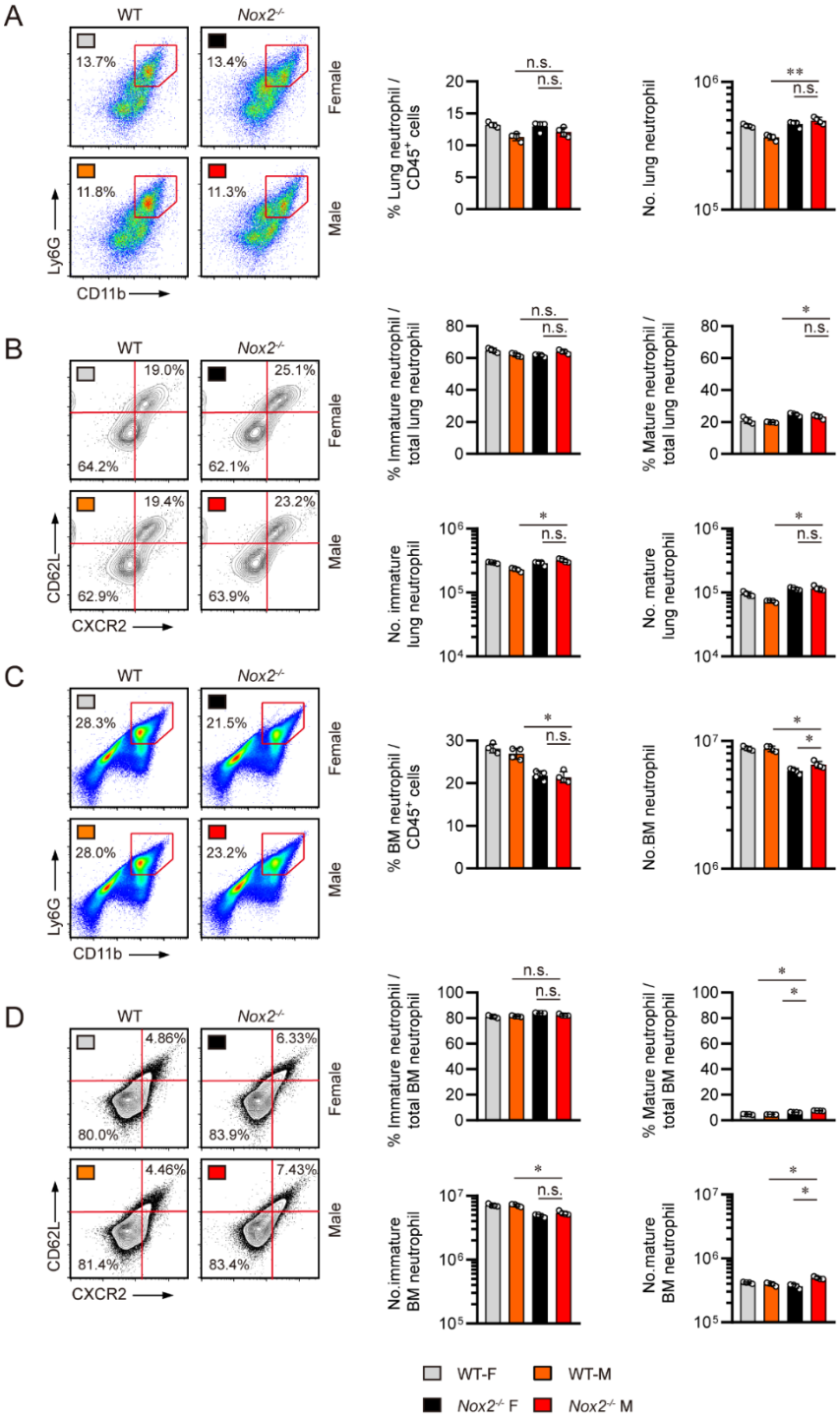

Figure 8. BM and lung neutrophil profiles of uninfected WT and *Nox2*$^{-/-}$ mice are illustrated. Neutrophil counts and percentages from the lungs and bone marrows of uninfected WT and *Nox2*$^{-/-}$ mice are provided (n = 4 per group). **(A)** The percentages of neutrophils among lung CD45^{+} cells and total cell counts are presented in bar graphs, along with flow cytometry plots. **(B)** Total cell counts and the percentages of CXCR2^{lo}CD62L^{lo} immature neutrophils and CXCR2^{hi}CD62L^{hi} mature neutrophils among total lung neutrophils are presented in bar graphs, along with flow cytometry plots. **(C)** The percentages of neutrophils among CD45^{+} bone marrow cells and total cell counts are presented in bar graphs, along with flow cytometry plots. **(D)** Total cell counts and the percentages of CXCR2^{lo}CD62L^{lo} immature neutrophils and CXCR2^{hi}CD62L^{hi} mature neutrophils among total bone marrow neutrophils are presented in bar graphs, along with flow cytometry plots. The data are presented as the mean ± SD of four mice in each group. The significance of differences was determined using the One-way ANOVA test and Mann-Whitney-U test. *n.s.*, not significant. *$p < 0.05$. **$p < 0.01$.

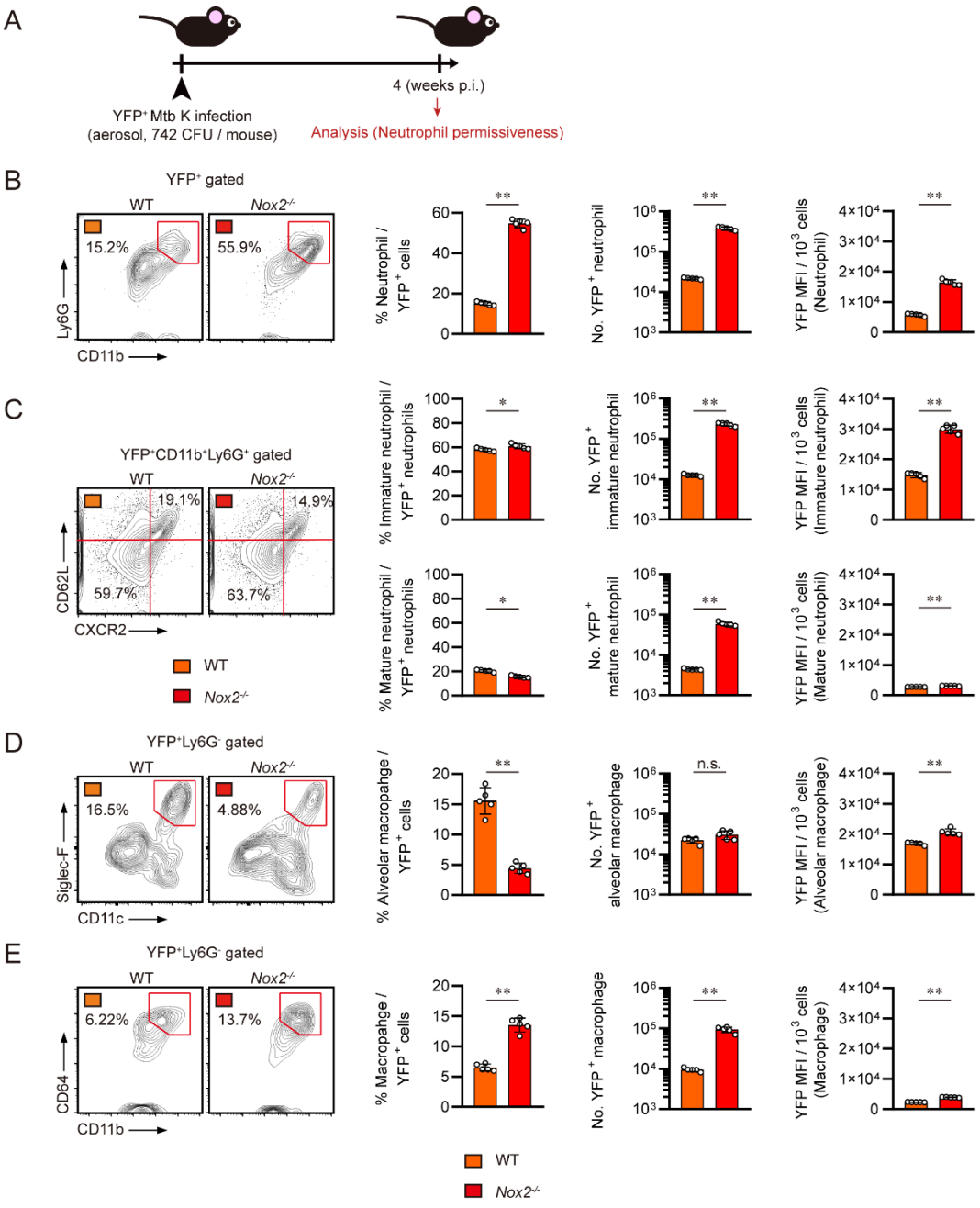

Figure 9. Immature neutrophils were the most permissive cells to mycobacterial infection among phagocytes infected with YFP$^+$ Mtb. (A) Experimental design for the *in vivo* enumeration of permissiveness in phagocytes. Male WT and *Nox2*$^{-/-}$ mice (n = 5 per group) were aerosol infected with YFP-expressing Mtb K strain. At four weeks post-infection, all mice were autopsied, and permissiveness of neutrophils were analysed via flow cytometry (indicated by red arrow). Initial CFU = 742. **(B)** The percentage of neutrophils among YFP$^+$ cells are presented in bar graphs, along with flow cytometry plots. The number of YFP$^+$ neutrophils and MFI values of YFP in concatenated neutrophils (10^3 cells) are presented in bar graphs. **(C)** Total cell counts, percentages among YFP$^+$ neutrophils, and MFI values of YFP (per 10^3 concatenated cells) in CXCR2^{lo}CD62L^{lo} immature neutrophils and CXCR2^{hi}CD62L^{hi} mature neutrophils are presented in bar graphs, along with flow cytometry plots. Total cell counts, percentages among YFP$^+$ cells, and MFI values of YFP (per 10^3 concatenated cells) in **(D)** CD11c$^+$Siglec-F$^+$ alveolar macrophages and **(E)** CD11b$^+$CD64$^+$ recruited macrophages are presented in bar graphs, along with flow cytometry plots. The experiment was conducted once. The data are presented as the mean ± SD of five mice in each group. The significance of differences was determined using the One-way ANOVA test and Mann-Whitney-U test. *n.s.*, not significant. *$p < 0.05$. **$p < 0.01$.

4. Neutrophil depletion alleviates TB pathogenesis and lung hyperinflammation in male *Nox2*$^{-/-}$ mice

The exacerbated TB pathogenesis of male *Nox2*$^{-/-}$ mice was characterized by uncontrolled pro-inflammatory cytokine production and influx of permissive immature pulmonary neutrophils. Considering that neutrophils contribute to lung inflammation in *Nox2*$^{-/-}$ mice[11,51,123], and they are responsible for the increased mycobacterial burden in TB susceptible mouse models[124,125], we hypothesized that reducing Ly6G^{+} neutrophils would alleviate TB pathogenesis in male *Nox2*$^{-/-}$ mice. Starting from two weeks post-infection, a Ly6G-specific monoclonal antibody (mAb) was intraperitoneally injected to WT and *Nox2*$^{-/-}$ mice to deplete neutrophils. At four weeks post-infection, the mice were autopsied **(Figure 10A)**. Neutrophil depletion alleviated TB pathogenesis in both WT and *Nox2*$^{-/-}$ mice, by effectively reducing bacterial load in the lungs and spleens **(Figure 10B)** and lung inflammation **(Figure 10C)**. IFN-γ, IL-1 α, IL-1 β, IL-6, TNF-α, and G-CSF levels were significantly downregulated in the lungs of male *Nox2*$^{-/-}$ mouse after neutrophil depletion **(Figure 10D)**, while IL-10, IL-4, IL-5, and TGF-β levels were not significantly altered **(Figure 10E)**. Therefore, we clarified that Ly6G^{+} neutrophils are the actual cause of TB progression and lung hyperinflammation in male *Nox2*$^{-/-}$ mouse.

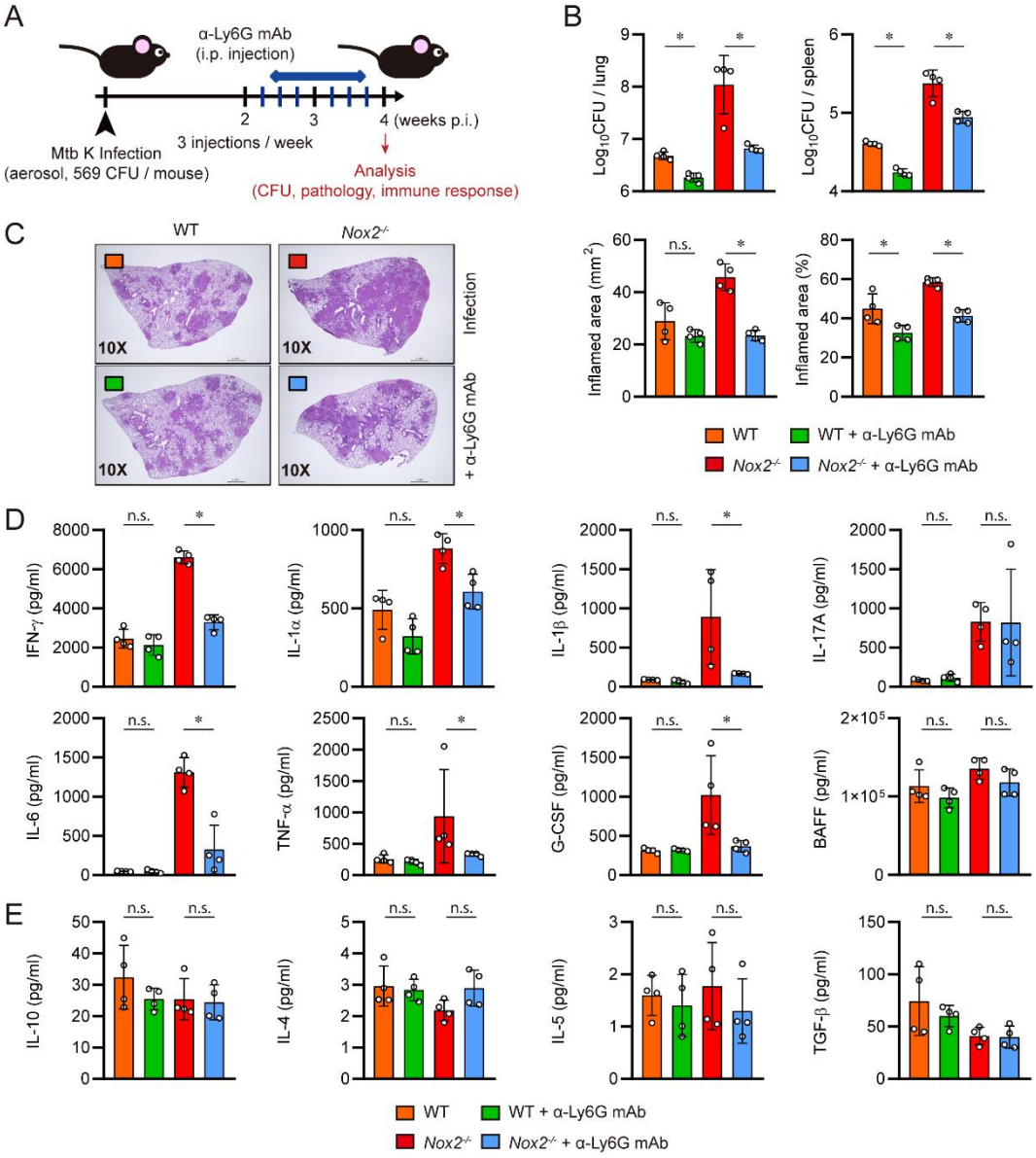

Figure 10. Neutrophil depletion ameliorated TB pathogenesis in male *Nox2*$^{-/-}$ *mice*. (A) Experimental design for *in vivo* depletion of neutrophils in Mtb infected mice. six-week old male WT and *Nox2*$^{-/-}$ mice (n = 4 per group) were aerosol infected with Mtb K strain. Starting from two weeks post-infection, 250 μg of anti-Ly6G mAb was intraperitoneally injected into each mouse three times a week (indicated by blue bars). At four weeks post-infection, all mice were autopsied, and immunological analysis, bacterial counting, and histopathological analysis were conducted (indicated by red arrow). Initial CFU = 569. **(B)** Mycobacterial CFUs in the lungs and spleens of each group at four weeks post-infection were analyzed by calculating the number of colonies and presented in bar graphs. **(C)** H&E staining was performed on the superior lobes of the right lung at four weeks post-infection to visualize the gross lung pathology. The inflamed area of the H&E-stained samples was quantified in terms of percentage and square millimeters and presented in bar graphs. **(D)** IFN-γ, IL-1α, IL-1β, IL-17A, IL-6, TNF-α, G-CSF, and BAFF levels in Mtb-infected mouse lung lysates were measured by ELISA and LEGENDplex. **(E)** IL-10, IL-4, IL-5, and TGF-β levels in Mtb-infected mouse lung lysates were measured by ELISA and LEGENDplex. The cytokine levels are presented in bar graphs. The experiment was conducted twice. The data are presented as the mean ± SD of four mice in each group. The significance of differences was determined, using the One-way ANOVA and Mann-Whitney U test. *n.s.*, not significant. *$p < 0.05$.

5. Neutrophil depletion reduces immature lung neutrophils and restores pulmonary lymphocytes in Mtb infected male *Nox2*$^{-/-}$ mice

Ly6G^{+} neutrophil depletion not only ameliorated TB pathogenesis, but also altered immune cell compositions in the lungs of male *Nox2*$^{-/-}$ mice. Neutrophil depletion removed most lung neutrophils in WT mice, and significantly reduced pulmonary neutrophil numbers in male *Nox2*$^{-/-}$ mice **(Figure 11A)**. Surprisingly, it was highly effective at reducing CXCR2^{lo}CD62L^{lo} pulmonary immature neutrophils in both WT and *Nox2*$^{-/-}$ mice **(Figure 11B)**. Along with the reduction of immature pulmonary neutrophils, the number of B cells were increased in the lungs of Mtb infected male *Nox2*$^{-/-}$ mice **(Figure 11C)**. However, neutrophil depletion did not significantly alter lung T cell population in male *Nox2*$^{-/-}$ mice **(Figure 11D)**. This phenomenon was evident from the pie-charts and t-SNE plots illustrating lung immune cell dynamics, which clearly showed the reduction of pulmonary neutrophils and the restoration of B cells **(Figure 11E)**. Consequently, we discovered that the reduction of pulmonary neutrophil counts can restore the balance between lung lymphocytes and neutrophils in male *Nox2*$^{-/-}$ mice.

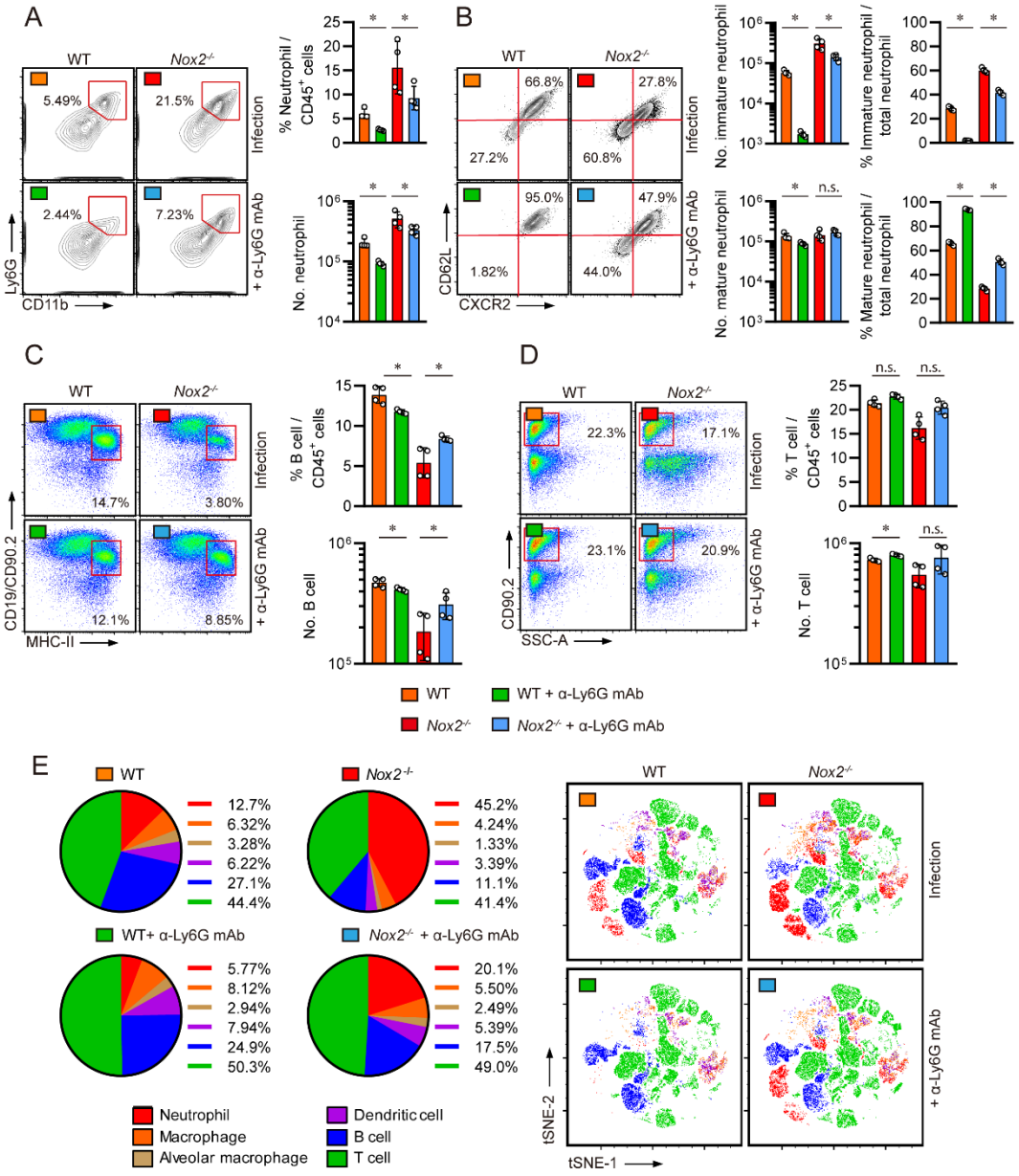

Figure 11. Neutrophil depletion removed immature neutrophils and restored lymphocytes in the lungs of Mtb infected *Nox2*$^{-/-}$ mice. Pulmonary **(A)** $CD11b^{+}Ly6G^{+}$ neutrophil, **(B)** $CD11b^{+}Ly6G^{+}CXCR2^{lo}CD62L^{lo}$ immature neutrophil, $CD11b^{+}Ly6G^{+}CXCR2^{hi}CD62L^{hi}$ mature neutrophil, **(C)** $CD19^{+}$MHC-II^{+} B cell, and **(D)** $CD90.2^{+}$ T cell populations of Mtb-infected mice at four weeks post-infection. The percentages of each immune cell among lung $CD45^{+}$ cells or total neutrophils, and total cell counts are presented in bar graphs, along with flow cytometry plots. **(E)** The compositions of the six major lung immune cell populations in Mtb-infected mice are presented in pie charts and t-SNE plots. The six major immune cells consist of neutrophils (red), macrophages (orange), alveolar macrophages (bright brown), dendritic cells (purple), B cells (blue), and T cells (green). The percentages of each immune cell among the sum of the six major immune cells are presented in pie charts. The data are presented as the mean ± SD of four mice in each group. The significance of differences was determined, using the One-way ANOVA and Mann-Whitney U test. *n.s.*, not significant. *$p < 0.05$.

4. DISCUSSION

Our study aimed to identify disease-promoting factors that are responsible for triggering Mtb-induced immunopathogenesis in the absence of phagocyte oxidase. We found that pulmonary infiltration of aberrant immature neutrophils is strongly associated with increased mycobacterial burden, lung hyperinflammation, and the loss of pulmonary lymphocytes in male *Nox2*$^{-/-}$ mice. We were able to remarkably alleviate TB progression in male *Nox2*$^{-/-}$ mice by reducing immature neutrophil counts. Overall, we identified G-CSF, rather than other host factors, as the initiator of immature pulmonary neutrophil-mediated TB immunopathogenesis in male *Nox2*$^{-/-}$ mice.

Progressed from previous studies on the roles of phagocyte oxidases in TB pathogenesis, our study proposed novel advocative findings. First, we have demonstrated that both sex difference and NOX2 deficiency can affect TB susceptibility in mice. In previous studies, gp91^{phox}-deficient mice did not feature a significant increase in mycobacterial load when compared to WT mice[3,43,108,109]. Similarly, Duox1 or p47^{phox}-deficient mice did not show an increase in lung mycobacterial load around four weeks post-infection[107,126]. Moreover, Olive et al. indicated that there was no variation in TB susceptibility between male and female gp91^{phox}-deficient mice[3,43]. However, we displayed that male *Nox2*$^{-/-}$ mice exhibited a significantly higher lung mycobacterial load compared to WT mice and female *Nox2*$^{-/-}$ mice. This could be attributed to the use of the Mtb K strain, recognized for its heightened virulence in comparison to the H37Rv and H37Ra strains[127,128]. Additionally, as we focused *in vivo* analysis at the four weeks post-infection period, when TB severity in *Nox2*$^{-/-}$ mice is optimized, we were able to evaluate the exacerbated TB susceptibility of male *Nox2*$^{-/-}$ mice. This observation of time-point-dependent alterations in TB progression in *Nox2*$^{-/-}$ mice is particularly significant, as the pulmonary influx of neutrophils occurs before the explosive increase in mycobacterial CFUs. Such findings highlight the crucial role of constant pulmonary neutrophil

influx, serving as a source of uncontrolled inflammation and a superior niche for Mtb, consequently driving TB pathogenesis. Our results newly indicate that biological sex is one of the crucial factors that accelerate TB pathogenesis in mice lacking phagocyte NADPH oxidase, which is inherited in an X-linked manner. Additionally, to the best of our knowledge, our study is the first to investigate the populations and functions of pulmonary lymphocytes in *Nox2*$^{-/-}$ mice during Mtb infection. We revealed that IFN-γ-producing CD4^{+} T cells were abundant, and antigen-specific Th1 responses were highly maintained in the lungs of male *Nox2*$^{-/-}$ mice. Hence, we concluded that the TB susceptibility of male *Nox2*$^{-/-}$ mice is not solely due to the inadequacy of Th1 responses, which contributes to TB susceptibility in various mouse models[113,129,130]. Lastly, we emphasized G-CSF as the primary inducer of immature neutrophil-mediated TB pathogenesis in male *Nox2*$^{-/-}$ mice, instead of other cytokines which remain essential for proper defense against Mtb infection. Chao et al. reported that the blockade of IL-1β or IL-1R can alleviate mycobacterial infection in phagocyte oxidase-deficient mice[3,44]. However, our data indicated that both IL-1α and IL-1β are required for proper defense against Mtb. IL-1α and IL-1β act as the upstream controllers of excessive G-CSF production in *Nox2*$^{-/-}$ mouse model[50,51], but they also play protective roles of in anti-TB immunity, such as activating myeloid cells in general, beyond just neutrophils[131-133]. We suggest that such protective roles of IL-1 signaling are especially crucial in the early phases of mycobacterial infection. By demonstrating that initiating IL-1R blockade at either one week or two weeks post-infection time point exacerbates TB progression in *Nox2*$^{-/-}$ mice, we highlighted the dominance of G-CSF over IL-1 in neutrophil-mediated TB pathogenesis.

Although *Nox2*$^{-/-}$ mice are prone to autoimmune diseases such as rheumatoid arthritis[84,85], Mtb-induced lung hyperinflammation in *Nox2*$^{-/-}$ mice was not primarily associated with impaired Th1 responses or autoreactive T cells. We observed that pulmonary neutrophils are the actual cause of lung hyperminflammation, and the loss of pulmonary B cells is more closely associated with

neutrophilic inflammation rather than alterations in T cell responses. Our research may offer deeper insights into TB susceptible animal models that are not associated with altered T cell function. We explicitly characterized immature lung neutrophils and identified them as the primary drivers of TB immunopathology in male *Nox2*$^{-/-}$ mice. While various studies have emphasized the importance of neutrophils in promoting lung inflammation in *Nox2*$^{-/-}$ mice undergoing bacterial, parasitic, or fungal challenge[46,50,123,134,135], their properties were not dissected in detail. We uncovered that *Nox2*$^{-/-}$ immature pulmonary neutrophils feature CD11b^{int}Ly6G^{int} and CXCR2^{lo}CD62L^{lo} phenotypes, altered size and granularity, and increased mycobacterial permissiveness. Still, we need transcriptomic or metabolomic analysis of CD11b^{int}Ly6G^{int}CXCR2^{lo}CD62L^{lo} immature neutrophils to elucidate the precise mechanisms underlying neutrophilic inflammation and mycobacterial permissiveness. We proposed novel interventions with therapeutic potentials to enable proper control of immature neutrophils. The effectiveness of neutrophil depletion in alleviating TB pathogenesis and Mtb-induced lung hyperinflammation was formerly demonstrated in TB susceptible *Nos2*$^{-/-}$ and *TLR2*$^{-/-}$ mice[136,137], as well as in WT mice suffering from chronic TB[138]. We firstly provided the therapeutic potential of neutrophil depletion in alleviating TB pathogenesis specifically in *Nox2*$^{-/-}$ mice. We also demonstrated the effectiveness of AM80 in alleviating TB pathogenesis. While Yamada et al. illustrated that ATRA intervention mitigated TB progression by increasing pulmonary T cell counts or reducing pulmonary myeloid-derived suppressor cells (MDSCs)[139-143], AM80 has not been tested on animal models as a therapeutic agent against TB. We highlighted the efficacy of AM80 in controlling TB pathogenesis in a susceptible mouse model, focusing on its role in reducing inflammatory neutrophils rather than altering T cell or macrophage responses. We have newly revealed that AM80 intervention does not alter Mtb-specific T cell responses in *Nox2*$^{-/-}$ mice. Although AM80 may affect the phagocytic capacities of *Nox2*$^{-/-}$ macrophages, we have excluded the effects on macrophages because AM80 did not alter the

phagocytosis of *Nox2*$^{-/-}$ BMDMs in our setup studies. Since AM80 shows enhanced potency compared to ATRA and is free from the side effects associated with RAR-γ activation[144,145], AM80 intervention may offer superior outcomes for establishing host-directed TB therapies in susceptible models compared to ATRA. Furthermore, our study newly discovered that G-CSF neutralization can alleviate TB pathogenesis in *Nox2*$^{-/-}$ mice. These attempts may provide insights into controlling TB progression in susceptible animal models with excessive pulmonary granulocyte influx.

Still, our study requires discussions on the following limitations. AM80 intervention was effective at mitigating TB pathogenesis in WT mice, while G-CSF neutralization did not clearly alter TB progression in this mouse model. This is considered to be originated from two different reasons. Firstly, unlike male *Nox2*$^{-/-}$ mouse model, WT mice do not show excessive and constant G-CSF production in response to Mtb infection. Therefore, Mtb infected WT mice may have an insufficient amount of circulating G-CSF which should be depleted through G-CSF neutralization. The second reason is that G-CSF and AM80 promotes myeloid cell generation via independent signaling pathways. AM80 induces neutrophil differentiation and maturation through the activation of RAR, while G-CSF is not involved in RAR signaling or C/EBPβ activation, rapidly generating immature neutrophils[146]. Therefore, we conclude that AM80 featured therapeutic capacity in both mouse strains, while G-CSF neutralization specifically showed potency in male *Nox2*$^{-/-}$ mouse model. While anti-Ly6G mAb injection successfully removed pulmonary neutrophils in WT mice, it failed to fully eliminate the cells in *Nox2*$^{-/-}$ mice. This outcome is thought to stem from the nature of the intraperitoneal injection of anti-Ly6G mAb (1A8). Boivin et al. noted that intraperitoneal injection of anti-GR1 or Ly6G monoclonal antibodies may not fully eliminate neutrophils, as newly synthesized young neutrophils can replenish the blood or organs even after depletion[147]. Furthermore, anti-Ly6G mAb mediates slow neutrophil depletion through Fc-dependent opsonization and phagocytosis of neutrophils by macrophages. Considering that NOX2 deficiency leads to both G-

CSF mediated constant neutrophil production and macrophage malfunction, we conclude that these two factors contributed to the incomplete depletion of pulmonary neutrophils in male *Nox2*$^{-/-}$ mice. A similar explanation can be given for the persistence pro-inflammatory cytokines in the lungs, even after mAb-mediated cytokine neutralization. This inefficiency is likely due to the nature of intraperitoneal injections, which effectively target circulating cells or cytokines but may not completely reach lung-residing targets. Additionally, since *Nox2*$^{-/-}$ neutrophils are inflammatory, they are likely the source of the cytokines that were still detected after intraperitoneal depletion. To optimally deplete such targets, a combination of intraperitoneal and intratracheal injections is likely necessary to effectively target and deplete cytokines residing in the lung. The disparity in the effects of IL-1R blockade on *Nox2*$^{-/-}$ mice also warrants discussion. Despite following protocols from Olive et al.[3], initiating IL-1R blockade from two weeks post-infection exacerbated TB in male *Nox2*$^{-/-}$ mice. We conclude that differences in the infection model system contributed to this discrepancy. Specifically, our study differed from previous ones in terms of the mycobacterial strain virulence, initial infectious doses, and the ages of the mice used. IL-1R blockade may suppress neutrophil-mediated TB pathogenesis in a less severe infection model, but it was ineffective in our system, which involved a severe infection with a high dose of the highly virulent Mtb K strain.

Despite the abundance of T cell responses, male *Nox2*$^{-/-}$ mice displayed severe TB progression. Accumulating evidences suggest that disrupted T cell responses during Mtb infection may diminish protection against the infection. For instance, the deficiency of the T cell inhibitory receptor PD-1 leads to a significant enhancement of T cell responses and an increase in the pulmonary mycobacterial burden[148,149]. Given that neutrophil depletion and G-CSF neutralization decreased the pulmonary levels of IFN-γ and IL-17A in male *Nox2*$^{-/-}$ mice, maintaining the balance between immune activation and suppression might be more crucial for the proper control of TB than the amount of cytokines produced. To gain a deeper understanding of TB pathogenesis, it is crucial to

identify immunologic factors that disrupt the proper activation of Th1 responses. The absence of pulmonary B cells in the presence of BAFF, TNF-α, and IL-6, which are B cell activating cytokines, remains a question to be solved. As pulmonary B cells play crucial roles in suppressing neutrophil-mediated lung inflammation through direct interaction[150,151], their absence may contribute to TB susceptibility in *Nox2*$^{-/-}$ mice. Thus, elucidating the association between the increase in neutrophils and the decrease in B cells may contribute to a better understanding of anti-TB immunity. We investigated the impacts of AM80 intervention at four weeks post-infection. However, considering the broad roles of retinoic acids in modulating macrophage and T cell responses[139,141], understanding the significance of non-neutrophil factors affected by AM80, such as T cell responses, recruited macrophage functions, and alveolar macrophage functions at early stages of Mtb infection, can significantly enhance our understanding of the pathogenesis of TB in susceptible animal models.

5. CONCLUSION

Collectively, our study revealed that phagocyte NADPH oxidase deficiency contributes to exacerbated TB immunopathogenesis in a sex-dependent manner. This is attributed to the excessive pulmonary infiltration of immature neutrophils in the presence of sufficient Th1 responses. Therapeutic interventions targeting the generation of G-CSF driven immature pulmonary neutrophils successfully ameliorated TB immunopathogenesis in male *Nox2*$^{-/-}$ mice. Our study provides a comprehensive understanding of TB pathogenesis and highlights potential therapeutic targets for proper TB control in the absence of phagocyte-specific NADPH oxidase.

Chapter III

Establishment of anti-TB immunotherapy targeting immature pulmonary neutrophils by targeting G-CSF

1. INTRODUCTION

Mycobacterium tuberculosis (Mtb) is the causative agent of Tuberculosis (TB), which remains a significant public health concern worldwide. Approximately, one-quarter of the world's population is estimated to have latent Mtb infection, with 5-10% of these individuals at risk of developing active TB at some point during their lifetime[96]. The factors that influence susceptibility to Mtb are still not completely understood, which hampers the control of this harmful pathogen[97-99]. There is extensive documentation indicating that males are more susceptible to TB than females, and this sexual bias is observed in various animal models including mice and humans[100,101]. The increased TB susceptibility in males is likely due to differences in immune cell functions as well as in their compositions[102,103]. Such host factor-mediated alterations in immune function may directly influence immune responses to Mtb infection. Considering the importance of immunological balance in maximizing anti-TB immunity, both excessive immune suppression or activation might be harmful to the host during TB progression[104-106]. These clues have led to the hypothesis that several host

factors, such as biological sex and genetic distributions, which modulate inflammatory responses, may influence TB immunopathogenesis.

The phagocyte NADPH oxidase (NOX2, gp91^{phox}) is located in the lumen of phagosomes. Its primary function is to produce reactive oxygen species (ROS), which play a crucial role in protecting the host against a wide range of pathogens[3,4]. NOX2 also plays a vital role in regulating autophagy and cytokine/chemokine signaling[7-9]. The NOX2 complex is a multimeric enzyme composed of a single catalytic transmembrane heterodimer (gp91^{phox} / p22^{phox}) and four cytosolic subunits (p40^{phox} / p47^{phox} / p67^{phox} / Rac). Among the six major components of NOX2 complex, gp91^{phox} acts as the catalytic core for ROS generation[5,6]. Individuals with impaired NOX2 function may develop chronic granulomatous disease (CGD), characterized by an increased susceptibility to fungal and bacterial infections and impaired inflammation control[10-12]. Since *Nox2* is located at Xp21.1 of the X chromosome, CGD caused by *Nox2* deficiency is inherited in an X-linked recessive manner, primarily affecting young males[13,14]. Furthermore, individuals with X-linked CGD have a heightened vulnerability to mycobacterial infections[38]. This poses significant challenges for TB therapy and prevention in X-linked CGD patients as BCG vaccination cannot be implemented due to the high risks of BCGosis, which is a disseminated mycobacterial infection that can occur following BCG vaccination[16,40,41].

Although phagocyte NADPH oxidase-originated ROS play a crucial role in clearing intracellular pathogens, studies have shown that phagocyte NADPH oxidase deficiencies did not significantly alter mycobacterial growth compared to wild type (WT) animals. According to Cooper et al., p47^{phox}-deficient mice featured increase in lung mycobacterial load from 15 to 30 days post-infection. However, the increase in mycobacterial load was not sustained after 30 days post-infection[107]. Additionally, Olive et al. reported that male and female gp91^{phox}-deficient mice did not show an increase in lung mycobacterial load until 60 days or 20 weeks post-infection[108,109]. These researches

give clues that NOX2 deficiency may modulate immune responses against Mtb, independently of ROS-mediated bactericidal effects. Recent studies support this idea as Thomas et al. demonstrated that $gp91^{phox}$-deficient mice displayed enhanced inflammation and lung neutrophil infiltration after Mtb challenge, which were mediated by IL-1[3,43].

Dysregulated inflammatory responses and aberrant granuloma formation are hallmark features of X-linked CGD. X-linked CGD patients and NOX2-deficient mice exhibit uncontrolled formation of granulomas, characterized by an excessive influx of phagocytic myeloid cells to the site of infection[69,70]. NOX2-deficient phagocytes, such as macrophages and neutrophils, are major producers of pro-inflammatory cytokines[48,49], which can cause tissue damage[44,50]. Given that NOX2 deficiency-induced X-linked CGD can cause TB susceptibility along with lung hyperinflammation, we hypothesized that Mtb infection would cause uncontrolled inflammation and disruption of immune tolerance in NOX2-deficient mice. As the maintenance of immune tolerance is critical for effective anti-TB immunity, we further hypothesized that controlling the specific immunologic factor which causes Mtb infection-driven hyperinflammation would be crucial for ameliorating TB pathogenesis.

In this study, we established four experimental groups to investigate how two independent host factors (NOX2 deficiency and male sex) can modify the immunological responses against Mtb infection. As both male sex and NOX2 deficiency are risk factors for TB susceptibility, we hypothesized that male *Nox2*$^{-/-}$ mice would exhibit severer TB progression than female *Nox2*$^{-/-}$ mice and male WT mice. Additionally, we anticipated that specific immune factors would contribute to TB pathogenesis and hyperinflammation in male *Nox2*$^{-/-}$ mice, which show a clear correlation to disease progression. Finally, we aimed to discover novel interventions that can effectively regulate these disease-promoting factors in male *Nox2*$^{-/-}$ mice.

We found that male *Nox2*$^{-/-}$ mice exhibited higher levels of lung inflammation and mycobacterial burden compared to female *Nox2*$^{-/-}$ mice and WT mice following Mtb challenge. Male *Nox2*$^{-/-}$ mice also featured elevated production of pro-inflammatory cytokines in the lungs, along with excessive infiltration of immature neutrophils and reduction of lymphocytes at infection sites. We also dissected the properties of aberrant permissive immature neutrophils, which were distinct from mature neutrophils and constituted the majority of immune cell populations in male *Nox2*$^{-/-}$ mice. By reducing the number of total lung neutrophils or immature neutrophils, we could successfully mitigate TB pathogenesis in male *Nox2*$^{-/-}$ mice. Finally, we determined that G-CSF, rather than other cytokines, is the dominant controller of immature neutrophil generation through *in vivo* neutralization of each cytokine. Collectively, we identified G-CSF driven permissive neutrophils as the key immunologic factor that facilitates TB immunopathogenesis and lung hyperinflammation in male *Nox2*$^{-/-}$ mice. Furthermore, we suggested novel therapeutic interventions targeting immature neutrophils, which might be potential for controlling TB in NOX2-deficient condition.

2. MATERIALS AND METHODS

2.1. Ethics statements and study approval

All animal experiments followed the regulations set by the Korean Food and Drug Administration. The Ethics Committee and Institutional Animal Care and Use Committee (2019-0174; C57BL/6N, *Nox2*$^{-/-}$, 2022-0140; C57BL/6N, *Nox2*$^{-/-}$) at Yonsei University Health System (Seoul, Korea) granted approval for each experimental protocol.

2.2. Mice

Six- to seven-week-old female and male C57BL/6N mice were obtained from Japan SLC, Inc. (Shizuoka, Japan). Six- to seven-week-old female and male *Nox2*$^{-/-}$ mice were provided by Dr. Yun Soo Bae (Ewha Womans University, Seoul, South Korea). The mice were housed in a specific pathogen-free (SPF) environment with barriered conditions at the Yonsei University Medical Research Center SPF facility.

2.3. Bacterial culture and infection protocols

Purchase of the Mtb K strain, mycobacterial culture, and aerosol infection processes were executed according to the referenced studies[110,111]. The mycobacteria were cultured in 7H9 broth supplemented with 10% oleic acid-albumin-dextrose-catalase (OADC; Difco Laboratories, MD) and 2 μg/ml of mycobactin J (Allied Monitor, Fayette, MO) for 4 weeks at 37℃. Following cultivation, all bacteria were washed three times with 10 mM phosphate-buffered saline (PBS; pH 7.4). Bacterial cell pellets were collected after centrifugation, and small aliquots were stored at -80℃ until use. The Mtb K strain used for *in vivo* challenges was PDIM positive. YFP vectors for the generation of YFP^{+} Mtb K strain were kindly gifted by Dr. Christopher Sassetti. In order to

deliver bacteria to the lungs of each mouse, all mice were exposed to at least 200 viable mycobacteria in an inhalation chamber for 60 minutes.

2.4. *In vivo* treatments for neutrophil control

From two weeks post-infection, 250 μg/mouse of anti-Ly6G mAb (clone: 1A8, Bio X Cell, West Lebanon, NH, USA), 200 μg/mouse of anti-IL-1R mAb (clone: JAMA-147, Bio X Cell, West Lebanon, NH, USA), 200 μg/mouse of anti-IFN-γ mAb (clone: H22, Bio X Cell, West Lebanon, NH, USA), and 250 μg/mouse of anti-IL-17A mAb (clone: 17F3, Bio X Cell, West Lebanon, NH, USA) mAb were intraperitoneally administered. The antibodies were diluted in PBS and administered three times a week for a total duration of two weeks. From one-week post-infection, 30 μg/mouse of anti-G-CSF mAb (clone: #67604, R&D Systems, Minneapolis, MN, USA), 200 μg/mouse of anti-IL-1R mAb (clone: JAMA-147, Bio X Cell, West Lebanon, NH, USA), 400 μg/mouse of anti-IL-6 mAb (clone: MP5-20F3, Bio X Cell, West Lebanon, NH, USA), 200 μg/mouse of anti-IL-1α mAb (clone: ALF-161, Bio X Cell, West Lebanon, NH, USA), and 200 μg/mouse of anti-IL-1β mAb (clone: B122, Bio X Cell, West Lebanon, NH, USA) were intraperitoneally administered. The antibodies were diluted in PBS and administered three times a week for a total duration of three weeks. Rat IgG2a, rat IgG1, Armenian hamster IgG, and mouse IgG1 isotype control antibodies were purchased from Bio X Cell (West Lebanon, NH, USA). Isotype control antibodies were administered to control mice in correspondence with the original antibodies. From one-week post-infection, 20 μg/mouse of AM80 (Sigma-Aldrich, St. Louis, MO, USA) was orally administered. AM80 was diluted in PBS and administered three times a week for a total duration of three weeks.

2.5. Antibodies and flow cytometry

Flow cytometric analysis of immune cells was conducted using the subsequent antibodies. LIVE/DEAD Fixable Near-IR Dead Cell Stain Kit, Green Dead Cell Stain Kit, and Aqua Dead Cell Stain Kit were purchased from Molecular Probes (Carlsbad, CA, USA). Brilliant violet (BV) 605-conjugated mAb against Thy1.2 and CD19; Allophycocyanin (APC)-conjugated mAb against CD45R (B220); BV 421-conjugated mAb against CD45; APC-R700-conjugated mAb against Siglec-F; Fluorescein isothiocyanate (FITC)-conjugated mAb against CD95 (FAS); BV 786-conjugated mAb against CXCR2; and V450- conjugated mAb against Ly6G were purchased from BD Bioscience (San Jose, CA, USA). Phycoerythrin (PE)-conjugated mAb against CXCR2, CD64, IFN-γ, and GL7; Peridinin chlorophyll (PerCP)-Cy5.5-conjugated mAb against CD11b; APC-Cy7-conjugated mAb against MHC-II; Alexa fluor 700-conjugated mAb against CD62L; and PE-Dazzle conjugated mAb against CD11c were purchased from Biolegend (San Diego, CA, USA). Surface and intracellular staining processes were executed according to the referenced study[112].

2.6. Preparation of single cell suspensions and immune cell analysis

Four weeks post-infection, the mice were euthanized via inhalation of carbon dioxide and then underwent an autopsy. The mouse lungs were perfused before undergoing flow cytometry analysis. Using the methods described in previous studies[113,114], single-cell suspensions were obtained from the entire lung tissue. These cells were then stained with the mAbs mentioned in the previous section and subjected to flow cytometry analysis.

2.7. Measurement of cytokines

For the analysis of lung cytokines, lung lysates from the autopsied mice were collected, homogenized, dissolved into PBS, and then stored in a -80℃ freezer. For the analysis of T cell cytokines, lung single cell suspensions were stimulated with two different Mtb antigens, PPD and

ESAT-6 according to the referenced studies[112,114]. To detect cytokines, sandwich enzyme-linked immunosorbent assay (ELISA) and LEGENDplex kits were utilized. Briefly, mouse G-CSF and IL-1α ELISA kits were purchased from R&D Systems (Minneapolis, MN, USA). Mouse IFN-γ, IL-1β, IL-17A, and IL-5 ELISA kits were purchased from Invitrogen (San Diego, CA, USA). Mouse IL-10 ELISA kit, LEGENDplex mouse B cell panel (for the detection of TNF-α, IL-4, IL-6, BAFF, and TGF-β), and LEGENDplex mouse inflammation panel (for the detection of IL-1α, IL-1β) were purchased from Biolegend (San Diego, CA, USA).

2.8. Quantification of lung inflammation and mycobacterial CFU

The lungs and spleens of Mtb infected mice were harvested four weeks post-infection. The right superior lobes of the lungs were kept in 10% formalin overnight for preservation and later embedded in paraffin. To perform histopathologic analysis, the lungs were sectioned at 4-5 μm and stained with hematoxylin and eosin (H&E). To quantify pulmonary inflammation in each mouse, we employed Adobe Photoshop (Adobe, San Jose, California) and ImageJ (National Institutes of Health, USA) programs, following a previously described reference[115]. The complete lung lesion image was isolated using Adobe Photoshop and saved as a separate file. Another image, identical in size to the original lung image but filled with black, was also saved as a separate file. These images were then opened in ImageJ. By using the 'Split Channels' function, the image from the green channel was processed to calculate the size of the area showing green positivity, which was originally purple-blue due to H&E staining. The black-colored image was analyzed through the green channel in the same manner to calculate the size of the entire lung lesion. The 'inflamed area (%)' value, which indicates the proportion of inflamed tissue relative to the entire lung lesion, was computed by dividing the green positivity values of the first image by the green positivity values of the black-colored image. Subsequently, the actual size of the inflamed lesion was calculated by determining

the pixel values in Adobe Photoshop. The pixel value corresponding to a single millimeter was calculated based on a 2mm scale bar included in each images. The pixel value for the entire lung lesion was also enumerated, and the value was divided by the square of the pixel value representing one millimeter to quantify the size (mm^2) of each lung lesion. By multiplying the inflamed area (%) values by the total lung sizes (mm^2) for each sample, we were able to precisely enumerate the exact size of each inflamed area (mm^2). To enumerate mycobacterial growth, lung and spleen tissues were plated onto Middlebrook 7H10 agar (Becton Dickinson, Franklin Lakes, NJ, USA) after homogenization, following preparation methods from previous studies[113,116]. After a four-week incubation period at 37℃, mycobacterial colonies were counted.

2.9. Neutrophil purification and assessment of mycobacterial permissiveness

MACS magnetic cell sorting kit including anti-Ly6G magnetic beads and LS MACS columns (Miltenyi Biotec, Bergisch Gladbach, Germany) was used to enrich $Ly6G^+$ cells from the lungs of Mtb-infected mice. The manufacturer's protocols were followed. After separating $Ly6G^+$ lung cells, the cells were treated with Triton X-100 (Sigma-Aldrich, St. Louis, MO, USA) and plated onto Middlebrook 7H10 agar (Becton Dickinson, Franklin Lakes, NJ, USA). After a three-week incubation period at 37℃, mycobacterial colonies were counted.

2.10. Statistical analyses

The results were presented as the mean ± standard deviation (SD). To analyze the significance of differences between two selected groups, One-way ANOVA and Mann-Whitney U test were conducted using GraphPad Prism version 8 for Windows (GraphPad Software, La Jolla, CA, USA, www.graphpad.com). The statistical significance was determined using the following definitions: *n.s.*: not significant, $*p < 0.05$, and $**p < 0.01$. Correlation analysis and unpaired t-test were

conducted using GraphPad Prism, and the correlation coefficients and p-values were reported for each graph. Flowjo V10 (Flowjo, Ashland, OR, USA) was employed to perform t-distributed stochastic neighbor embedding (t-SNE) analysis.

3. RESULTS

3.1. AM80 administration mitigates TB pathogenesis in male *Nox2*$^{-/-}$ mice and reduces pulmonary immature neutrophils

Among various strategies for the specific control of immature neutrophils, we considered RA treatment as a promising option. Previous studies have examined that retinoic acid (RA) or retinoic acid receptor (RAR) agonist administration can effectively promote the generation of fully differentiated mature neutrophils, which feature segmented nuclei and enhanced bactericidal capacity[152,153]. Moreover, Yamada et al. suggested the potential of RAs such as all-trans retinoic acid (ATRA) as a therapeutic agent against mycobacterial infection[139,141]. To investigate whether immature neutrophil-specific intervention can ameliorate TB pathogenesis in male *Nox2*$^{-/-}$ mouse, we utilized tamibarotene (AM80), a synthetic retinoid and a RAR agonist demonstrating 10 times greater potency than ATRA. AM80 induces the expression of key molecules, such as C/EBP, CD11b, and CXCR2 through the activation of RARα and RARβ[146], triggering a cascade of cellular pathways that generate fully functional mature neutrophils[154,155]. Starting from one-week post-infection, we orally administered 40 μg of AM80 per mouse, with a total of nine injections given over three weeks. At four weeks post-infection, the mice were autopsied **(Figure 1A)**. AM80 administration significantly reduced mycobacterial load in the lungs and spleens **(Figure 1B)** and alleviated lung inflammation **(Figure 1C)** in male *Nox2*$^{-/-}$ mice. However, despite a reduction in pulmonary bacterial load, its effects were not prominent in reducing lung inflammation of male WT mice. AM80 administration downregulated pulmonary expression of IFN-γ, IL-1 β, IL-17A, and G-CSF in male *Nox2*$^{-/-}$ mice. It did not substantially alter the expression of pro-inflammatory cytokines in male WT mice, although the expression of TNF-α was significantly reduced **(Figure 1D)**. AM80 intervention did not alter the expression of IL-10, IL-4, IL-5, and TGF-β in both WT and *Nox2*$^{-/-}$

mice **(Figure 1E)**. Total lung neutrophil counts **(Figure 1F)** and $CXCR2^{lo}CD62L^{lo}$ immature lung neutrophil counts **(Figure 1G)** were significantly decreased, and the portion of mature neutrophils among total lung neutrophils were increased in AM80-treated WT and *Nox2*$^{-/-}$ mice. While AM80 treatment effectively modified the accumulation of immature lung neutrophils, it did not exhibit significant effects in promoting Mtb-specific T cell responses in WT and *Nox2*$^{-/-}$ mice **(Figure 2)**. This suggests that the therapeutic potential of AM80 intervention in male *Nox2*$^{-/-}$ mice is largely contingent on the conversion of neutrophil maturity. To summarize, we specified immature lung neutrophils as the key subpopulation responsible for accelerating TB pathogenesis in male *Nox2*$^{-/-}$ mice.

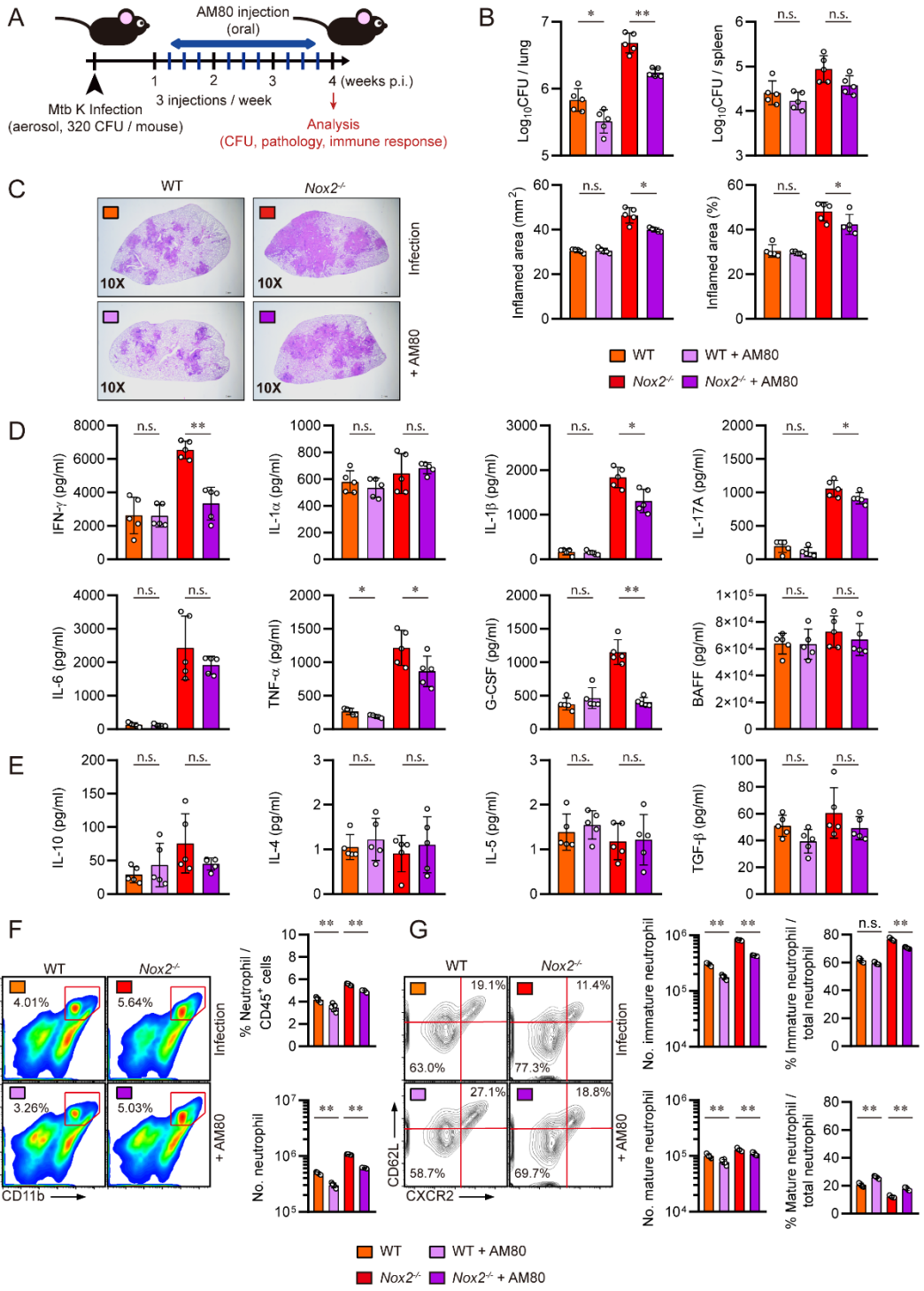

Figure 1. AM80 administration mitigated TB pathogenesis in male *Nox2*$^{-/-}$ mice by reducing immature neutrophils. (A) Experimental design for *in vivo* administration of AM80 in Mtb infected mice. Six-week old male WT and *Nox2*$^{-/-}$ mice (n = 5 per group) were aerosol infected with Mtb K strain. Starting from one week post-infection, 20 μg of AM80 was orally administered to each mouse three times a week (indicated by blue bars). At four weeks post-infection, all mice were autopsied, and immunological analysis, bacterial counting, and histopathological analysis were conducted (indicated by red arrow). Initial CFU = 320. **(B)** Mycobacterial CFUs in the lungs and spleens of each group at four weeks post-infection were analyzed by calculating the number of colonies and presented in bar graphs. **(C)** H&E staining was performed on the superior lobes of the right lung at four weeks post-infection to visualize the gross lung pathology. The inflamed area of the H&E-stained samples was quantified in terms of percentage and square millimeters and presented in bar graphs. **(D)** IFN-γ, IL-1α, IL-1β, IL-17A, IL-6, TNF-α, G-CSF, and BAFF levels in Mtb-infected mouse lung lysates were measured by ELISA and LEGENDplex. **(E)** IL-10, IL-4, IL-5, and TGF-β levels in Mtb-infected mouse lung lysates were measured by ELISA and LEGENDplex. The cytokine levels are presented in bar graphs. Pulmonary **(F)** $CD11b^{+}Ly6G^{+}$ neutrophil, **(G)** $CD11b^{+}Ly6G^{+}CXCR2^{lo}CD62L^{lo}$ immature neutrophil, and $CD11b^{+}Ly6G^{+}CXCR2^{hi}CD62L^{hi}$ mature neutrophil populations of Mtb-infected mice at four weeks post-infection. The percentages of each immune cell among lung $CD45^{+}$ cells or total neutrophils, and total cell counts are presented in bar graphs, along with flow cytometry plots. The experiment was conducted twice. The data are presented as the mean ± SD of five mice in each group. The significance of differences was determined, using the One-way ANOVA and Mann-Whitney U test. *n.s.*, not significant. *$p < 0.05$. **$p < 0.01$.

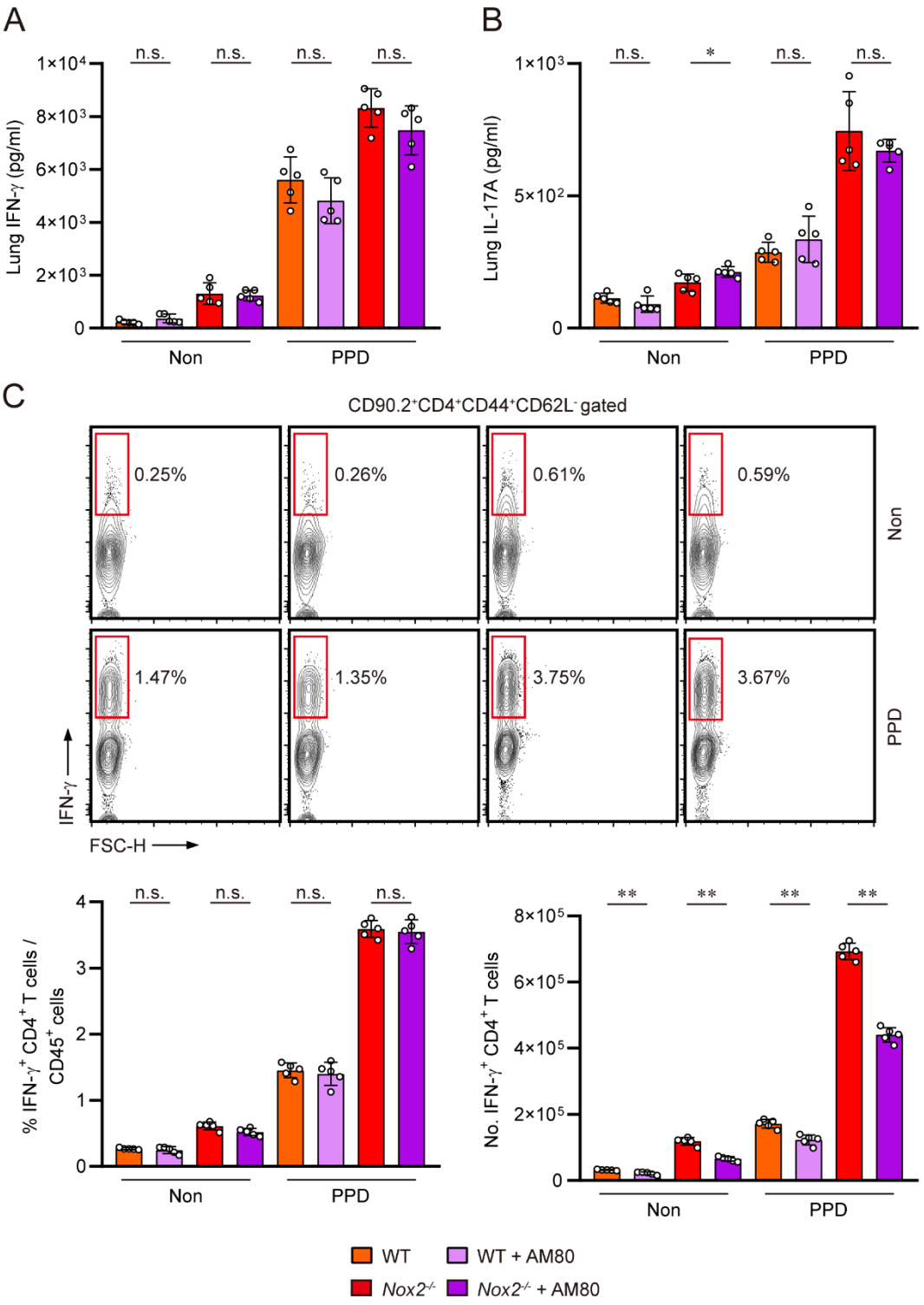

Figure 2. AM80 treatment did not significantly alter T cells responses against mycobacterial antigens. Live lung cell suspensions were cultured with or without mycobacterial antigens ESAT-6 and PPD for 8 hours. **(A)** Lung IFN-γ levels and **(B)** Lung IL-17A levels after mycobacterial antigen stimulus are presented in bar graphs. **(C)** IFN-γ positive $CD90.2^+$ $CD4^+$ $CD44^+$ $CD62L^+$ effecter T cell populations are presented in bar graphs and flow cytometry plots. The data are presented as the mean ± SD of five mice in each group. The significance of differences was determined, using the One-way ANOVA test and Mann-Whitney test. *n.s.*, not significant. $*p < 0.05$. $**p < 0.01$.

3.2. G-CSF predominantly regulates the generation of permissive immature pulmonary neutrophils in Mtb infected male *Nox2*$^{-/-}$ mice

To conclude the study, we aimed to identify specific immunologic factors responsible for the generation of CXCR2^{lo}CD62L^{lo} permissive immature pulmonary neutrophils**.** Considering that pro-inflammatory cytokines upregulated in the lungs of Mtb-infected male *Nox2*$^{-/-}$ mice, such as IL-1, IL-6, and G-CSF accelerate the production of immature neutrophils through emergency granulopoiesis[156-158], we hypothesized that uncontrolled production of pro-inflammatory cytokines may trigger an explosive generation of immature neutrophils. To identify the causative cytokines, we administered mAbs to neutralize each cytokine in *Nox2*$^{-/-}$ mice. We confirmed that IFN-γ and IL-17A, key cytokines in anti-TB immunity for both innate and adaptive immune responses, are not associated with the generation of immature neutrophils. *In vivo* neutralization of IFN-γ or IL-17A increased mycobacterial burden, lung inflammation, pro-inflammatory cytokine levels, and pulmonary influx of immature neutrophils in female *Nox2*$^{-/-}$ mice **(Figure 3)**. Furthermore, *in vivo* neutralization of IL-6, IL-1α, and IL-1β also aggravated immature neutrophil-mediated TB pathogenesis and lung hyperinflammation in *Nox2*$^{-/-}$ mice, although IL-1 is reported to be crucial for mediating neutrophilic inflammation in NOX2-deficient conditions[3,44,50,51] **(Figure 4)**. Blockade of IL-1 receptor (IL-1R), which inhibits the function of both IL-1α, and IL-1β, exacerbated TB progression in *Nox2*$^{-/-}$ mice as well. We implemented two different *in vivo* blockade models: a three-week IL-1R blockade on female *Nox2*$^{-/-}$ mice and a two-week IL-1R blockade on male *Nox2*$^{-/-}$ mice, following the protocols from Olive et al.[3]. Both blockade models resulted in exacerbated TB progression, as evidenced by increased pulmonary bacterial load, lung inflammation, and neutrophil counts in both female and male *Nox2*$^{-/-}$ mice **(Figure 5)**. In contrast, *in vivo* neutralization of G-CSF, the main controller of granulopoiesis, remarkably ameliorated immature neutrophil-mediated TB pathogenesis in male *Nox2*$^{-/-}$ mice. Starting from one-week post-infection, G-CSF specific mAb was

intraperitoneally administered, with a total of nine injections over a three-week period. At four weeks post-infection, the mice were autopsied **(Figure 6A)**. While G-CSF neutralization did not alleviate TB progression in WT mice, it significantly reduced mycobacterial load in the lungs and spleens **(Figure 6B)** and mitigated lung inflammation **(Figure 6C)** of male *Nox2*$^{-/-}$ mice. G-CSF neutralization also downregulated IFN-γ, IL-1α, IL-1β, IL-17A, IL-6, TNF-α, G-CSF, and BAFF levels specifically in the lungs of male *Nox2*$^{-/-}$ mice **(Figure 6D)**, while IL-10. IL-4, IL-5, and TGF-β **(Figure 6E)** levels did not change. G-CSF neutralization decreased total lung neutrophil counts **(Figure 6F)** and CXCR2^{lo}CD62L^{lo} immature lung neutrophil counts **(Figure 6G)** in male WT and *Nox2*$^{-/-}$ mice. The reduction of immature lung neutrophils was particularly pronounced and dramatically reflected in G-CSF neutralized male *Nox2*$^{-/-}$ mice. This underscores that the excessive G-CSF-mediated accumulation of pathogenic immature neutrophils is a specific event observed in TB susceptible male *Nox2*$^{-/-}$ mice Ultimately, we concluded that upregulated G-CSF is the immunologic trigger for the generation of permissive immature pulmonary neutrophils, which facilitates TB immunopathogenesis and lung hyperinflammation in male *Nox2*$^{-/-}$ mice **(Figure 7)**.

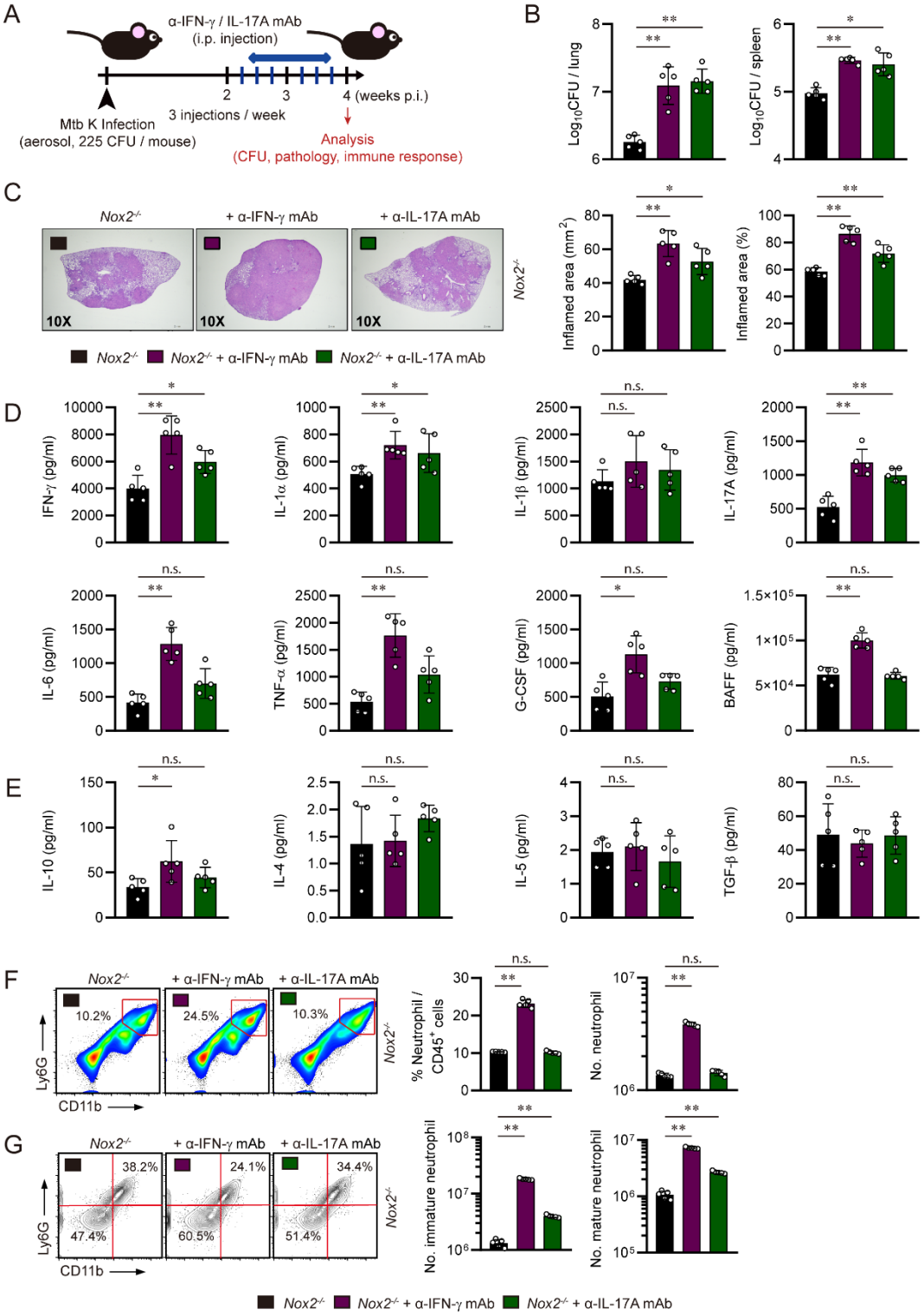

Figure 3. Neutralization of IFN-γ and IL-17A exacerbated TB pathogenesis of female *Nox2*$^{-/-}$ mice. (A) Experimental design for *in vivo* neutralization of IFN-γ and IL-17A in Mtb infected mice. six-week old female *Nox2*$^{-/-}$ mice (n = 5 per group) were aerosol infected with Mtb K strain. Starting from two weeks post-infection, 200 μg of anti-IFN-γ mAb or 250 μg of anti-IL-17A mAb was intraperitoneally administered to each mouse three times a week (indicated by blue bars). At four weeks post-infection, all mice were autopsied, and immunological analysis, bacterial counting, and histopathological analysis were conducted (indicated by red arrow). Initial CFU = 225. **(B)** Mycobacterial CFUs in the lungs and spleens of each group at four weeks post-infection were analyzed by calculating the number of colonies and presented in bar graphs. **(C)** H&E staining was performed on the superior lobes of the right lung at four weeks post-infection to visualize the gross lung pathology. The inflamed area of the H&E-stained samples was quantified in terms of percentage and square millimeters and presented in bar graphs. **(D)** IFN-γ, IL-1α, IL-1β, IL-17A, IL-6, TNF-α, G-CSF, and BAFF levels in Mtb-infected mouse lung lysates were measured by ELISA and LEGENDplex **(E)** IL-10, IL-4, IL-5, and TGF-β levels in Mtb-infected mouse lung lysates were measured by ELISA and LEGENDplex The cytokine levels are presented in bar graphs. Pulmonary **(F)** $CD11b^{+}Ly6G^{+}$ neutrophil, **(G)** $CD11b^{+}Ly6G^{+}CXCR2^{lo}CD62L^{lo}$ immature neutrophil, and $CD11b^{+}Ly6G^{+}CXCR2^{hi}CD62L^{hi}$ mature neutrophil populations of Mtb-infected mice at four weeks post-infection. The percentages of each immune cell among lung $CD45^{+}$ cells and total cell counts are presented in bar graphs, along with flow cytometry plots. The experiment was conducted once. The data are presented as the mean ± SD of five mice in each group. The significance of differences was determined, using the One-way ANOVA test. *n.s.*, not significant. $*p < 0.05$. $**p < 0.01$.

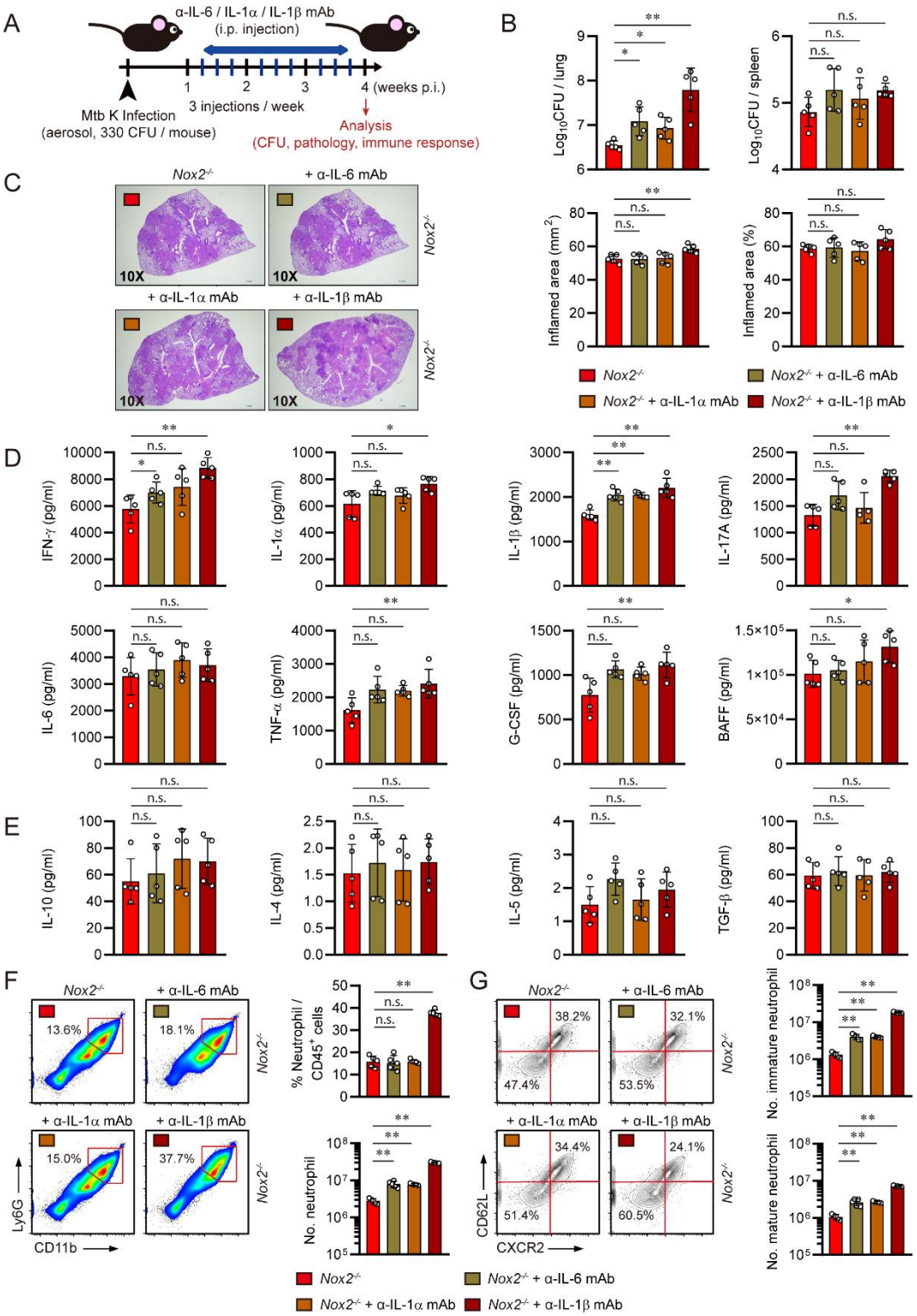

Figure 4. Neutralization of IL-6, IL-1α, and IL-1β exacerbated TB pathogenesis of male *Nox2*$^{-/-}$ mice. (A) Experimental design for *in vivo* neutralization of IL-6, IL-1α, and IL-1β in Mtb infected mice. six-week old male *Nox2*$^{-/-}$ mice (n = 5 per group) were aerosol infected with Mtb K strain. Starting from one week post-infection, 400 μg of anti-IL-6 mAb or 200 μg of anti-IL-1α mAb or 200 μg of anti-IL-1β mAb was intraperitoneally administered to each mouse three times a week (indicated by blue bars). At four weeks post-infection, all mice were autopsied, and immunological analysis, bacterial counting, and histopathological analysis were conducted (indicated by red arrow). Initial CFU = 330. **(B)** Mycobacterial CFUs in the lungs and spleens of each group at four weeks post-infection were analyzed by calculating the number of colonies and presented in bar graphs. **(C)** H&E staining was performed on the superior lobes of the right lung at four weeks post-infection to visualize the gross lung pathology. The inflamed area of the H&E-stained samples was quantified in terms of percentage and square millimeters and presented in bar graphs. **(D)** IFN-γ, IL-1α, IL-1β, IL-17A, IL-6, TNF-α, G-CSF, and BAFF levels in Mtb-infected mouse lung lysates were measured by ELISA and LEGENDplex **(E)** IL-10, IL-4, IL-5, and TGF-β levels in Mtb-infected mouse lung lysates were measured by ELISA and LEGENDplex The cytokine levels are presented in bar graphs. Pulmonary **(F)** $CD11b^{+}Ly6G^{+}$ neutrophil, **(G)** $CD11b^{+}Ly6G^{+}CXCR2^{lo}CD62L^{lo}$ immature neutrophil, and $CD11b^{+}Ly6G^{+}CXCR2^{hi}CD62L^{hi}$ mature neutrophil populations of Mtb-infected mice at four weeks post-infection. The percentages of each immune cell among lung $CD45^{+}$ cells and total cell counts are presented in bar graphs, along with flow cytometry plots. The experiment was conducted once. The data are presented as the mean ± SD of five mice in each group. The significance of differences was determined, using the One-way ANOVA test. *n.s.*, not significant. *$p < 0.05$. **$p < 0.01$.

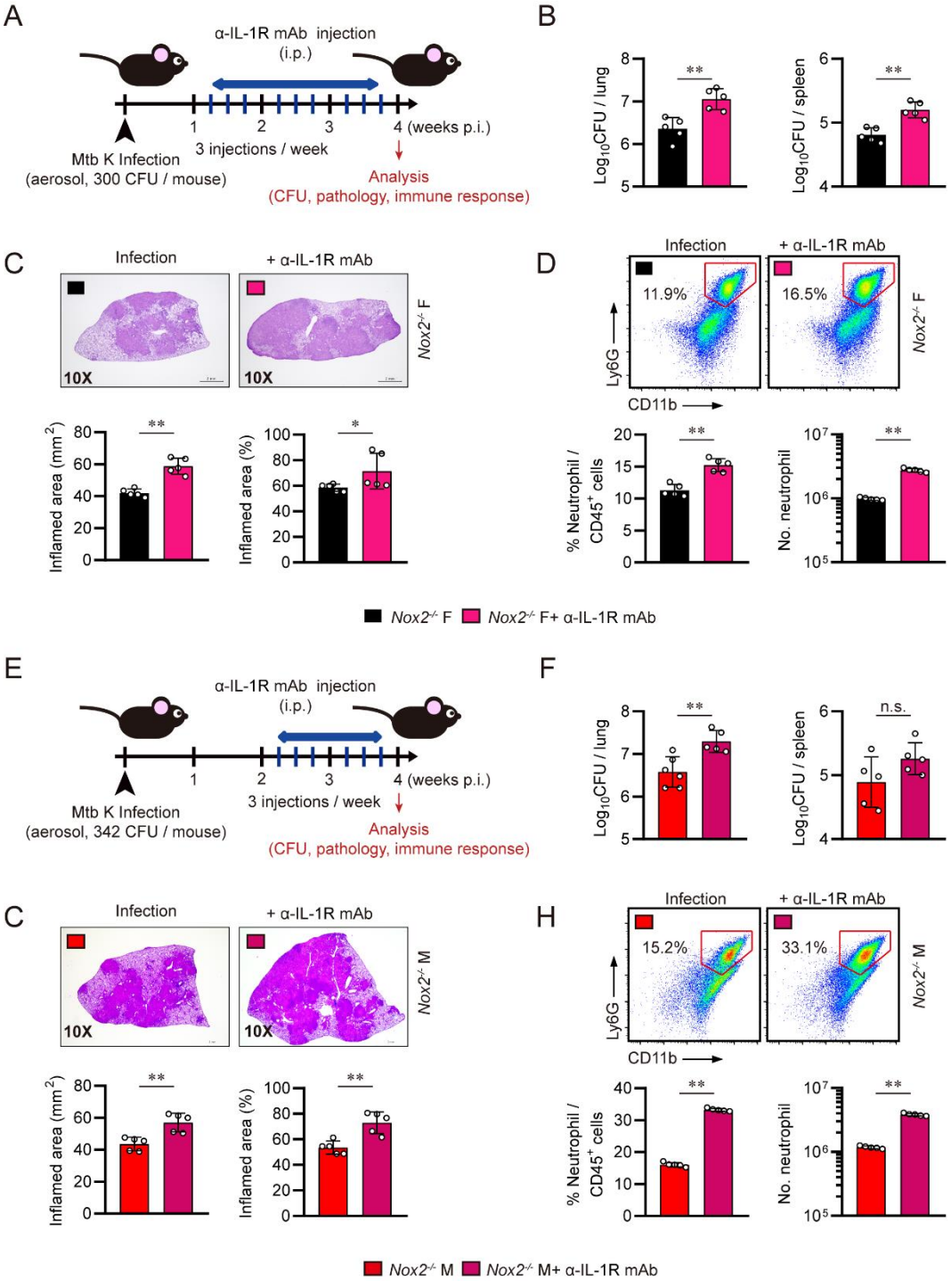

Figure 5. Blockade of IL-1R exacerbated TB pathogenesis of *Nox2*$^{-/-}$ mice. (A) Experimental design for *in vivo* blockade of IL-1R in Mtb infected female *Nox2*$^{-/-}$ mice. six-week old female *Nox2*$^{-/-}$ mice (n = 5 per group) were aerosol infected with Mtb K strain. Starting from one week post-infection, 200 μg of anti-IL-1R mAb was intraperitoneally administered to each mouse three times a week (indicated by blue bars). At four weeks post-infection, all mice were autopsied, and bacterial counting and histopathological analysis were conducted (indicated by red arrow). Initial CFU = 300. **(B)** Mycobacterial CFUs in the lungs and spleens of each group at four weeks post-infection were analyzed by calculating the number of colonies and presented in bar graphs. **(C)** H&E staining was performed on the superior lobes of the right lung at four weeks post-infection to visualize the gross lung pathology. The inflamed area of the H&E-stained samples was quantified in terms of percentage and square millimeters and presented in bar graphs. **(D)** Pulmonary $CD11b^{+}Ly6G^{+}$ neutrophil populations of Mtb-infected mice at four weeks post-infection. The percentages of neutrophils among lung $CD45^{+}$ cells and total cell counts are presented in bar graphs, along with flow cytometry plots. **(E)** Experimental design for *in vivo* blockade of IL-1R in Mtb infected male *Nox2*$^{-/-}$ mice. six-week old male *Nox2*$^{-/-}$ mice (n = 5 per group) were aerosol infected with Mtb K strain. Starting from two weeks post-infection, 200 μg of anti-IL-1R mAb was intraperitoneally administered to each mouse three times a week (indicated by blue bars). At four weeks post-infection, all mice were autopsied, and bacterial counting and histopathological analysis were conducted (indicated by red arrow). Initial CFU = 342. **(F)** Mycobacterial CFUs in the lungs and spleens of each group at four weeks post-infection were analyzed by calculating the number of colonies and presented in bar graphs. **(G)** H&E staining was performed on the superior lobes of the right lung at four weeks post-infection to visualize the gross lung pathology. The inflamed area of the H&E-stained samples was quantified in terms of percentage and square millimeters and presented in bar graphs. **(H)** Pulmonary $CD11b^{+}Ly6G^{+}$ neutrophil populations of Mtb-infected mice at four weeks post-infection. The

percentages of neutrophils among lung $CD45^+$ cells and total cell counts are presented in bar graphs, along with flow cytometry plots. The experiments were conducted once. The data are presented as the mean ± SD of five mice in each group. The significance of differences was determined, using the Mann-Whitney test. *n.s.*, not significant. *$p < 0.05$. **$p < 0.01$.

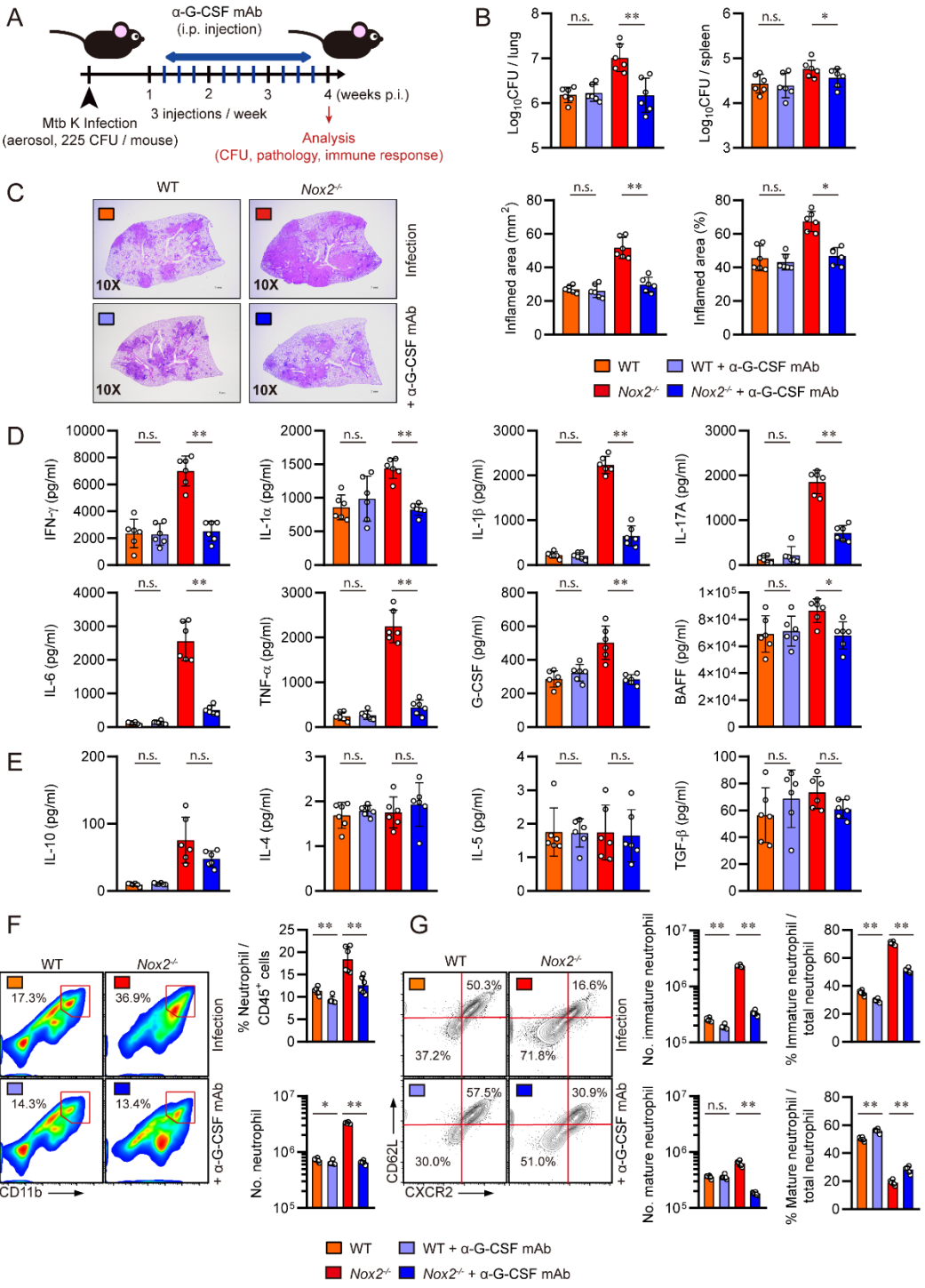

Figure 6. G-CSF neutralization ameliorated TB pathogenesis of male *Nox2*$^{-/-}$ mice by suppressing generation of immature pulmonary neutrophils. (A) Experimental design for *in vivo* neutralization of G-CSF in Mtb infected mice. Six-week old male WT and *Nox2*$^{-/-}$ mice (n = 6 per group) were aerosol infected with Mtb K strain. Starting from one week post-infection, 30 μg of anti-G-CSF mAb was intraperitoneally administered to each mouse three times a week (indicated by blue bars). At four weeks post-infection, all mice were autopsied, and immunological analysis, bacterial counting, and histopathological analysis were conducted (indicated by red arrow). Initial CFU = 225. **(B)** Mycobacterial CFUs in the lungs and spleens of each group at four weeks post-infection were analyzed by calculating the number of colonies and presented in bar graphs. **(C)** H&E staining was performed on the superior lobes of the right lung at four weeks post-infection to visualize the gross lung pathology. The inflamed area of the H&E-stained samples was quantified in terms of percentage and square millimeters and presented in bar graphs. **(D)** IFN-γ, IL-1α, IL-1β, IL-17A, IL-6, TNF-α, G-CSF, and BAFF levels in Mtb-infected mouse lung lysates were measured by ELISA and LEGENDplex. **(E)** IL-10, IL-4, IL-5, and TGF-β levels in Mtb-infected mouse lung lysates were measured by ELISA and LEGENDplex. The cytokine levels are presented in bar graphs. Pulmonary **(F)** $CD11b^{+}Ly6G^{+}$ neutrophil, **(G)** $CD11b^{+}Ly6G^{+}CXCR2^{lo}CD62L^{lo}$ immature neutrophil, and $CD11b^{+}Ly6G^{+}CXCR2^{hi}CD62L^{hi}$ mature neutrophil populations of Mtb-infected mice at four weeks post-infection. The percentages of each immune cell among lung $CD45^{+}$ cells or total neutrophils, and total cell counts are presented in bar graphs, along with flow cytometry plots. The experiment was conducted three times. The data are presented as the mean ± SD of six mice in each group. The significance of differences was determined, using the One-way ANOVA test. *n.s.*, not significant. *$p < 0.05$. **$p < 0.01$.

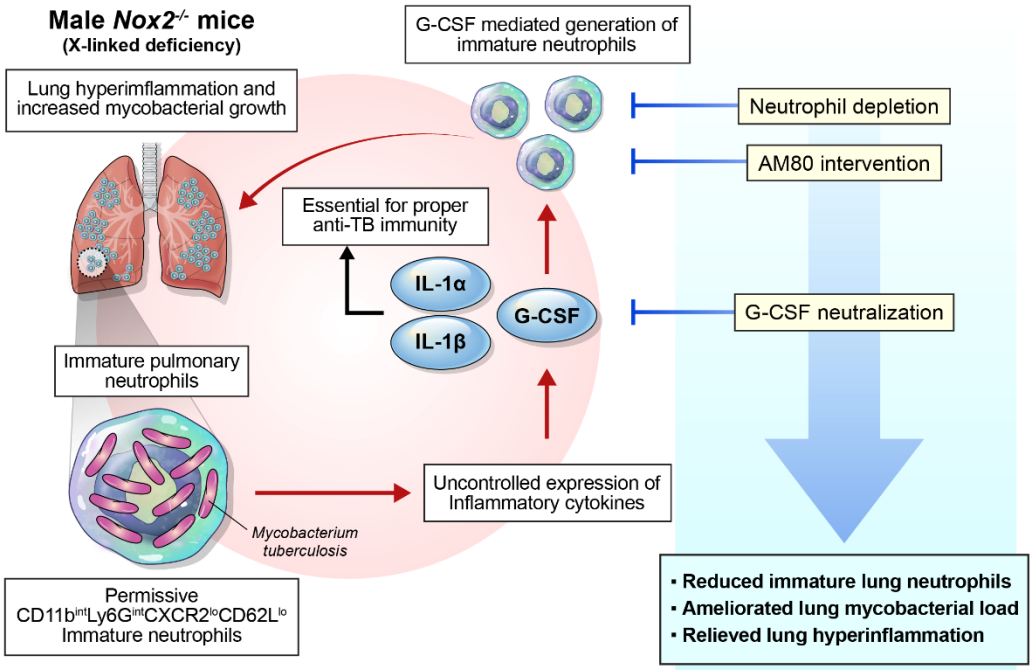

Figure 7. The results of the study are summarized in a visual abstract. $CD11b^{int}Ly6G^{int}CXCR2^{lo}CD62L^{lo}$ permissive immature pulmonary neutrophils are responsible for lung hyperinflammation and increased mycobacterial load in male *Nox2*$^{-/-}$ mice. Among the upregulated pro-inflammatory cytokines, G-CSF, rather than IL-1, plays a dominant role in generating immature neutrophils. The control of immature neutrophils through neutrophil depletion, AM80 intervention, and G-CSF neutralization has shown promising results in ameliorating TB immunopathogenesis in male *Nox2*$^{-/-}$ mice. Copyright of this image belongs to Plos Pathogens journal.

A

Step 1 : Processed in Adobe photoshop

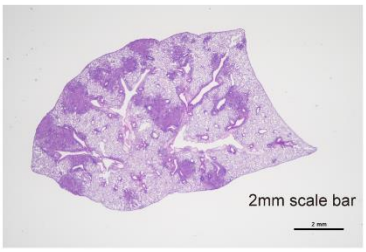

Original image with a 2mm scale bar

1mm = 211.5 pixels

$1mm^2$ = 44732.25 squre pixels

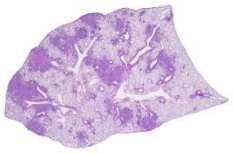

Total lung lesion isolated
(Image 1)

Total lung lesion filled with black
(Image 2)

Total lung lesion size = 2393989 square pixels

Step 2 : Processed in ImageJ

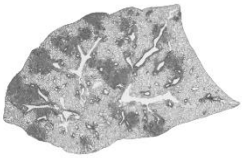

Image 1 splitted in green channel

Image 2 splitted in green channel

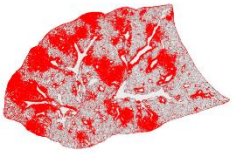

Enumeration of inflamed lesion
(15.36%)

Enumeration of total lung lesion
(38.07%)

1. Enumeration of Inflamed area (%) value =

15.36% / 38.07% = 40.35%

2. Enumeration of total lung size =

2393989 square pixels / 44732.25 square pixels = $53.52mm^2$

3. Enumeration of 'Inflamed area (mm^2) value =

$53.52mm^2$ * 40.35% = $21.59mm^2$

Figure 8. Quantification method of lung inflammation is briefly described. (A) As outlined in the Materials and Methods section, the inflamed area of the H&E-stained lung samples were quantified in terms of percentage and square millimetres. The values were calculated using Adobe Photoshop and ImageJ programs. New image files were created to determine the percentage of the inflamed (purple-stained) lesions, and the actual size of both total lung lesions and inflamed lesions was quantified in mm^2.

4. DISCUSSION

Our study aimed to identify disease-promoting factors that are responsible for triggering Mtb-induced immunopathogenesis in the absence of phagocyte oxidase. We found that pulmonary infiltration of aberrant immature neutrophils is strongly associated with increased mycobacterial burden, lung hyperinflammation, and the loss of pulmonary lymphocytes in male *Nox2*$^{-/-}$ mice. We were able to remarkably alleviate TB progression in male *Nox2*$^{-/-}$ mice by reducing immature neutrophil counts. Overall, we identified G-CSF, rather than other host factors, as the initiator of immature pulmonary neutrophil-mediated TB immunopathogenesis in male *Nox2*$^{-/-}$ mice.

Progressed from previous studies on the roles of phagocyte oxidases in TB pathogenesis, our study proposed novel advocative findings. First, we have demonstrated that both sex difference and NOX2 deficiency can affect TB susceptibility in mice. In previous studies, gp91^{phox}-deficient mice did not feature a significant increase in mycobacterial load when compared to WT mice[3,43,108,109]. Similarly, Duox1 or p47^{phox}-deficient mice did not show an increase in lung mycobacterial load around four weeks post-infection[107,126]. Moreover, Olive et al. indicated that there was no variation in TB susceptibility between male and female gp91^{phox}-deficient mice[3,43]. However, we displayed that male *Nox2*$^{-/-}$ mice exhibited a significantly higher lung mycobacterial load compared to WT mice and female *Nox2*$^{-/-}$ mice. This could be attributed to the use of the Mtb K strain, recognized for its heightened virulence in comparison to the H37Rv and H37Ra strains[127,128]. Additionally, as we focused *in vivo* analysis at the four weeks post-infection period, when TB severity in *Nox2*$^{-/-}$ mice is optimized, we were able to evaluate the exacerbated TB susceptibility of male *Nox2*$^{-/-}$ mice. This observation of time-point-dependent alterations in TB progression in *Nox2*$^{-/-}$ mice is particularly significant, as the pulmonary influx of neutrophils occurs before the explosive increase in mycobacterial CFUs. Such findings highlight the crucial role of constant pulmonary neutrophil

influx, serving as a source of uncontrolled inflammation and a superior niche for Mtb, consequently driving TB pathogenesis. Our results newly indicate that biological sex is one of the crucial factors that accelerate TB pathogenesis in mice lacking phagocyte NADPH oxidase, which is inherited in an X-linked manner. Additionally, to the best of our knowledge, our study is the first to investigate the populations and functions of pulmonary lymphocytes in *Nox2*$^{-/-}$ mice during Mtb infection. We revealed that IFN-γ-producing CD4^{+} T cells were abundant, and antigen-specific Th1 responses were highly maintained in the lungs of male *Nox2*$^{-/-}$ mice. Hence, we concluded that the TB susceptibility of male *Nox2*$^{-/-}$ mice is not solely due to the inadequacy of Th1 responses, which contributes to TB susceptibility in various mouse models[113,129,130]. Lastly, we emphasized G-CSF as the primary inducer of immature neutrophil-mediated TB pathogenesis in male *Nox2*$^{-/-}$ mice, instead of other cytokines which remain essential for proper defense against Mtb infection. Chao et al. reported that the blockade of IL-1β or IL-1R can alleviate mycobacterial infection in phagocyte oxidase-deficient mice[3,44]. However, our data indicated that both IL-1α and IL-1β are required for proper defense against Mtb. IL-1α and IL-1β act as the upstream controllers of excessive G-CSF production in *Nox2*$^{-/-}$ mouse model[50,51], but they also play protective roles of in anti-TB immunity, such as activating myeloid cells in general, beyond just neutrophils[131-133]. We suggest that such protective roles of IL-1 signaling are especially crucial in the early phases of mycobacterial infection. By demonstrating that initiating IL-1R blockade at either one week or two weeks post-infection time point exacerbates TB progression in *Nox2*$^{-/-}$ mice, we highlighted the dominance of G-CSF over IL-1 in neutrophil-mediated TB pathogenesis.

Although *Nox2*$^{-/-}$ mice are prone to autoimmune diseases such as rheumatoid arthritis[84,85], Mtb-induced lung hyperinflammation in *Nox2*$^{-/-}$ mice was not primarily associated with impaired Th1 responses or autoreactive T cells. We observed that pulmonary neutrophils are the actual cause of lung hyperminflammation, and the loss of pulmonary B cells is more closely associated with

neutrophilic inflammation rather than alterations in T cell responses. Our research may offer deeper insights into TB susceptible animal models that are not associated with altered T cell function. We explicitly characterized immature lung neutrophils and identified them as the primary drivers of TB immunopathology in male *Nox2*$^{-/-}$ mice. While various studies have emphasized the importance of neutrophils in promoting lung inflammation in *Nox2*$^{-/-}$ mice undergoing bacterial, parasitic, or fungal challenge[46,50,123,134,135], their properties were not dissected in detail. We uncovered that *Nox2*$^{-/-}$ immature pulmonary neutrophils feature CD11b^{int}Ly6G^{int} and CXCR2^{lo}CD62L^{lo} phenotypes, altered size and granularity, and increased mycobacterial permissiveness. Still, we need transcriptomic or metabolomic analysis of CD11b^{int}Ly6G^{int}CXCR2^{lo}CD62L^{lo} immature neutrophils to elucidate the precise mechanisms underlying neutrophilic inflammation and mycobacterial permissiveness. We proposed novel interventions with therapeutic potentials to enable proper control of immature neutrophils. The effectiveness of neutrophil depletion in alleviating TB pathogenesis and Mtb-induced lung hyperinflammation was formerly demonstrated in TB susceptible *Nos2*$^{-/-}$ and *TLR2*$^{-/-}$ mice[136,137], as well as in WT mice suffering from chronic TB[138]. We firstly provided the therapeutic potential of neutrophil depletion in alleviating TB pathogenesis specifically in *Nox2*$^{-/-}$ mice. We also demonstrated the effectiveness of AM80 in alleviating TB pathogenesis. While Yamada et al. illustrated that ATRA intervention mitigated TB progression by increasing pulmonary T cell counts or reducing pulmonary myeloid-derived suppressor cells (MDSCs)[139-143], AM80 has not been tested on animal models as a therapeutic agent against TB. We highlighted the efficacy of AM80 in controlling TB pathogenesis in a susceptible mouse model, focusing on its role in reducing inflammatory neutrophils rather than altering T cell or macrophage responses. We have newly revealed that AM80 intervention does not alter Mtb-specific T cell responses in *Nox2*$^{-/-}$ mice. Although AM80 may affect the phagocytic capacities of *Nox2*$^{-/-}$ macrophages, we have excluded the effects on macrophages because AM80 did not alter the

phagocytosis of *Nox2*$^{-/-}$ BMDMs in our setup studies. Since AM80 shows enhanced potency compared to ATRA and is free from the side effects associated with RAR-γ activation[144,145], AM80 intervention may offer superior outcomes for establishing host-directed TB therapies in susceptible models compared to ATRA. Furthermore, our study newly discovered that G-CSF neutralization can alleviate TB pathogenesis in *Nox2*$^{-/-}$ mice. These attempts may provide insights into controlling TB progression in susceptible animal models with excessive pulmonary granulocyte influx.

Still, our study requires discussions on the following limitations. AM80 intervention was effective at mitigating TB pathogenesis in WT mice, while G-CSF neutralization did not clearly alter TB progression in this mouse model. This is considered to be originated from two different reasons. Firstly, unlike male *Nox2*$^{-/-}$ mouse model, WT mice do not show excessive and constant G-CSF production in response to Mtb infection. Therefore, Mtb infected WT mice may have an insufficient amount of circulating G-CSF which should be depleted through G-CSF neutralization. The second reason is that G-CSF and AM80 promotes myeloid cell generation via independent signaling pathways. AM80 induces neutrophil differentiation and maturation through the activation of RAR, while G-CSF is not involved in RAR signaling or C/EBPβ activation, rapidly generating immature neutrophils[146]. Therefore, we conclude that AM80 featured therapeutic capacity in both mouse strains, while G-CSF neutralization specifically showed potency in male *Nox2*$^{-/-}$ mouse model. While anti-Ly6G mAb injection successfully removed pulmonary neutrophils in WT mice, it failed to fully eliminate the cells in *Nox2*$^{-/-}$ mice. This outcome is thought to stem from the nature of the intraperitoneal injection of anti-Ly6G mAb (1A8). Boivin et al. noted that intraperitoneal injection of anti-GR1 or Ly6G monoclonal antibodies may not fully eliminate neutrophils, as newly synthesized young neutrophils can replenish the blood or organs even after depletion[147]. Furthermore, anti-Ly6G mAb mediates slow neutrophil depletion through Fc-dependent opsonization and phagocytosis of neutrophils by macrophages. Considering that NOX2 deficiency leads to both G-

CSF mediated constant neutrophil production and macrophage malfunction, we conclude that these two factors contributed to the incomplete depletion of pulmonary neutrophils in male *Nox2*$^{-/-}$ mice. A similar explanation can be given for the persistence pro-inflammatory cytokines in the lungs, even after mAb-mediated cytokine neutralization. This inefficiency is likely due to the nature of intraperitoneal injections, which effectively target circulating cells or cytokines but may not completely reach lung-residing targets. Additionally, since *Nox2*$^{-/-}$ neutrophils are inflammatory, they are likely the source of the cytokines that were still detected after intraperitoneal depletion. To optimally deplete such targets, a combination of intraperitoneal and intratracheal injections is likely necessary to effectively target and deplete cytokines residing in the lung. The disparity in the effects of IL-1R blockade on *Nox2*$^{-/-}$ mice also warrants discussion. Despite following protocols from Olive et al.[3], initiating IL-1R blockade from two weeks post-infection exacerbated TB in male *Nox2*$^{-/-}$ mice. We conclude that differences in the infection model system contributed to this discrepancy. Specifically, our study differed from previous ones in terms of the mycobacterial strain virulence, initial infectious doses, and the ages of the mice used. IL-1R blockade may suppress neutrophil-mediated TB pathogenesis in a less severe infection model, but it was ineffective in our system, which involved a severe infection with a high dose of the highly virulent Mtb K strain.

Despite the abundance of T cell responses, male *Nox2*$^{-/-}$ mice displayed severe TB progression. Accumulating evidences suggest that disrupted T cell responses during Mtb infection may diminish protection against the infection. For instance, the deficiency of the T cell inhibitory receptor PD-1 leads to a significant enhancement of T cell responses and an increase in the pulmonary mycobacterial burden[148,149]. Given that neutrophil depletion and G-CSF neutralization decreased the pulmonary levels of IFN-γ and IL-17A in male *Nox2*$^{-/-}$ mice, maintaining the balance between immune activation and suppression might be more crucial for the proper control of TB than the amount of cytokines produced. To gain a deeper understanding of TB pathogenesis, it is crucial to

identify immunologic factors that disrupt the proper activation of Th1 responses. The absence of pulmonary B cells in the presence of BAFF, TNF-α, and IL-6, which are B cell activating cytokines, remains a question to be solved. As pulmonary B cells play crucial roles in suppressing neutrophil-mediated lung inflammation through direct interaction[150,151], their absence may contribute to TB susceptibility in *Nox2*$^{-/-}$ mice. Thus, elucidating the association between the increase in neutrophils and the decrease in B cells may contribute to a better understanding of anti-TB immunity. We investigated the impacts of AM80 intervention at four weeks post-infection. However, considering the broad roles of retinoic acids in modulating macrophage and T cell responses[139,141], understanding the significance of non-neutrophil factors affected by AM80, such as T cell responses, recruited macrophage functions, and alveolar macrophage functions at early stages of Mtb infection, can significantly enhance our understanding of the pathogenesis of TB in susceptible animal models.

5. CONCLUSION

Collectively, our study revealed that phagocyte NADPH oxidase deficiency contributes to exacerbated TB immunopathogenesis in a sex-dependent manner. This is attributed to the excessive pulmonary infiltration of immature neutrophils in the presence of sufficient Th1 responses. Therapeutic interventions targeting the generation of G-CSF driven immature pulmonary neutrophils successfully ameliorated TB immunopathogenesis in male *Nox2*$^{-/-}$ mice. Our study provides a comprehensive understanding of TB pathogenesis and highlights potential therapeutic targets for proper TB control in the absence of phagocyte-specific NADPH oxidase.

Chapter IV

Cholesterol 25-hydroxylase suppresses the optimal activation of dendritic cell-$CD4^+$ T cell axis and disrupts the induction of durable anti-tuberculosis immunity in BCG-vaccinated mice

1. INTRODUCTION

Tuberculosis (TB) is a detrimental pulmonary infectious disease caused by *Mycobacterium tuberculosis* (Mtb). TB remains a significant public health concern worldwide, causing approximately 1.5 million casualties every year. It is estimated that 25% of the world's population has latent Mtb infection, with approximately five to ten percent of those individuals at risk of developing active TB at some point during their lifetime[96,159]. While prevention and therapy against Mtb infection rely heavily on Bacillus Calmette–Guérin (BCG) vaccination and antibiotic treatment, respectively, the understanding of optimal protective immune responses against TB has not been fully elucidated. As the precise roles and contributions of various host factors on anti-TB immunity is a core factor for development of effective vaccines, deeper and more comprehensive studies aimed at identifying anti-TB immunity and host factors are necessary to clearly understand the underlying mechanisms of TB pathogenesis and to establish novel and effective protection or prevention strategies for TB.

Cholesterol is a lipid molecule that plays a variety of vital functions in both humans and animals. Cholesterol physiologically and chemically controls the plasma membrane of cells and acts as a

precursor for crucial compounds such as steroid hormones, bile acids, and neurosteroids[160,161]. Various cholesterol derivatives play crucial roles in mediating immune responses such as inflammation, immune cell differentiation, and immune cell migration[162,163]. Oxidized derivatives of cholesterol, known as oxysterols, are also crucial in regulating immune reactions such as apoptosis, autophagy, and inflammation[164,165].

Among various oxysterols, 25-hydroxycholesterol (25-HC) is widely known due to its multifunctional aspects in the immune system[166,167]. The production of 25-HC is mediated by cholesterol 25-hydroxylase (CH25H), an oxidative enzyme predominantly located in the endoplasmic reticulum (ER) of innate cells and is expressed in response to pathogen-related signals[168-170]. This enzyme was firstly identified in the 1970s while characterizing various enzymes involved in cholesterol metabolism[171,172]. While 25-HC was traditionally believed to be involved solely in cholesterol homeostasis, since the 2000s, it has been recognized for its critical roles in antiviral immunity[173,174]. They showed that CH25H-mediated production of 25-HC plays pivotal roles in blocking the membrane fusion of viruses onto the cell membranes of the host. Moreover, researchers revealed that 25-HC can suppress DNA replication in virus-infected cells. Such antiviral activities of 25-HC have been widely reported in various viral infection models, including HIV, Ebola virus, and SARS-CoV-2[175-177]. Researches further demonstrated that the expression of CH25H is highly dependent on type I interferon (type I IFN) signaling and the JAK/STAT1 pathway, which are essential factors for initiating antiviral immune responses[178-181]. Interestingly, other inflammatory signals, such as IFN-γ, can also upregulate the expression of CH25H in innate cells, suggesting that CH25H may act as an immune suppressive factor[180,182,183].

However, over the past decade, researches on CH25H have reached a critical turning point as studies have revealed that CH25H and 25-HC can influence immune responses against bacterial infections. While CH25H primarily serves protective roles in antiviral immunity, recent studies

suggest that it may exacerbate the pathogenesis of bacterial infections. For instance, CH25H expression in macrophages is triggered by *Listeria monocytogenes* infection in a type I IFN-dependent manner, which promotes the survival of this intracellular pathogen[184]. In a murine model of *Streptococcus pneumoniae* infection, an extracellular bacteria, CH25H-deficient mice displayed enhanced phagocytosis and bacterial clearance, resulting in reduced lung damage compared to wild-type (WT) mice[185].

Subsequent researches have further revealed that CH25H acts as a crucial immune modulator in inflammatory responses. Studies have shown that CH25H restricts the proper activation of inflammatory responses in bacterial infection models. According to Reboldi et al., CH25H regulated IL-1 and inflammasome-mediated inflammation in the model of septic shock, experimental autoimmune encephalomyelitis (EAE), and *Listeria monocytogenes* infection, acting downstream of type I IFN signaling[186]. Dang et al. reported that lipopolysaccharide (LPS) stimulation or *Listeria monocytogenes* infection induces the expression of CH25H, which in turn suppresses sterol regulatory element-binding protein 2 (SREBP2) and reduces inflammasome activation in macrophages[187]. These reports suggest that CH25H may function as an immune regulatory enzyme, expressed in response to pathogen-mediated inflammatory signals like type I IFN, and could potentially hinder the induction of appropriate innate immune responses against intracellular bacteria.

However, additional researches have uncovered controversial roles of CH25H, leading to various outcomes across different tissues and disease models. For instance, Xiao et al. reported that CH25H primarily suppresses the expression of inflammatory cytokines, such as IL-1β in macrophages, leading to immune reprogramming and the development of immunosuppressive macrophages[188]. In a mouse model of autoreactive skin inflammation, CH25H also played regulatory roles in suppressing T cell-mediated inflammation[189]. In contrast, Fesseler et al. suggested that exogenous

25-HC can accelerate pathogenesis and induce inflammation in a mouse model of SARS-CoV-2 infection[190]. Furthermore, various reports in neural disease models have demonstrated that CH25H and 25-HC promote inflammatory responses. Exogenous 25-HC can activate the NLRP3 inflammasome in a model of X-linked adrenoleukodystrophy[191] and amplify IL-1β production in microglial cells[192]. Additionally, CH25H and 25-HC accelerates neuroinflammation in a mouse model of tauopathy by activating pro-inflammatory signaling pathways[193]. Thus, since CH25H plays controversial roles across different tissues and disease models, understanding its function in a cell-type or tissue-specific manner is crucial for accurately dissecting its role in immune modulation.

Recent studies on the roles of CH25H and 25-HC in mycobacterial infections also emphasize their roles in disease progression. CH25H and 25-HC were upregulated in Mtb-infected macrophages and mouse lungs[194,195]. Zhou et al. recently discovered that pulmonary *Mycobacterium marinum* infection in mice upregulates CH25H, leading to the formation of pathogenic foam cells and the progression of lung pathology[196]. Furthermore, clinical reports provide clues about the impacts of CH25H and 25-HC in the progression of pulmonary infections including TB. 25-HC was increased in bronchoalveolar lavage fluid from asthma patients and was associated with the infiltration of eosinophils, neutrophils, and lymphocytes into the lungs[197]. CH25H expression was upregulated in the lungs of patients suffering from chronic obstructive pulmonary disease[198]. Bartlett et al. even suggested that G-protein coupled receptor 183 (GPR183)-7α,25-dihydroxycholesterol (7α,25-OHC) axis might play a significant role in TB development[199].

However, despite the growing interest in the role of CH25H in immune responses against Mtb, no studies have specifically addressed its critical function in altering dendritic cell (DC) activity during mycobacterial infections. As key modulators of anti-TB immune responses in both infection and vaccine-mediated protection models, DCs play a vital role[200,201]. Therefore, our study adopts a novel approach to investigate how CH25H deficiency impacts the functional properties of DCs, with a

focus on immune responses to mycobacterial stimulation.

Publications on the role of CH25H in modifying adaptive immune responses suggest that Mtb-induced type I IFN signaling and subsequent CH25H upregulation may impair the necessary responses for effective anti-TB immunity, such as Th1 responses. Chalmin et al. proposed that CH25H deficiency attenuated EAE progression by suppressing the trafficking of pathogenic autoimmune $CD4^+$ lymphocytes to the central nervous system. Such migration of lymphocytes was highly dependent on CH25H-mediated EBI2 activity[202]. Research conducted by Wu et al. demonstrated that 25-HC suppressed SIV antigen-specific $CD4^+$ lymphocytes, impairing IL-2 and TNF-α production [177]. While studies on the role of CH25H in mycobacterial infections have primarily focused on its impacts on innate immunity, given that Mtb-specific $CD4^+$ T cells are considered crucial for anti-TB immunity[203,204], CH25H may disrupt the optimal induction of Mtb-specific adaptive immune responses.

Thus, considering the immune regulatory role of CH25H and its status as an interferon stimulated gene (ISG) regulated by type I IFN signaling, a crucial factor in TB pathogenesis[205,206], we hypothesized that CH25H expression would restrict adequate Mtb-specific immune responses. In order to dissect the precise mechanisms of how CH25H restricts anti-TB immunity, we adapted *Ch25h*$^{-/-}$ mice, which are widely used in immune-related studies but not a common model for studying TB. Considering that *Ch25h*$^{-/-}$ mice feature clear modifications in immune responses, such as enhanced IL-1 responses and improved SREBP2-dependent IgA production[186,192,207], we hypothesized that *Ch25h*$^{-/-}$ mice might feature adjusted anti-TB immune responses, which show a clear correlation to defense against Mtb.

In this study, we first proposed that CH25H can modulate immune responses against Mtb infection by affecting the T cell activating properties of DCs. *Ch25h*$^{-/-}$ bone marrow-derived DCs (BMDCs) exhibited higher expression of co-stimulatory molecules CD80 and CD86, and produced higher

levels of IL-12p70 after stimulation. Moreover, we demonstrated that *Ch25h*$^{-/-}$ T cells alone cannot display enhanced proliferation and cytokine production, whereas T cells co-cultured with *Ch25h*$^{-/-}$ DCs successfully underwent rapid proliferation and cytokine expression, including superior IL-2 production *in vitro*. Although *Ch25h*$^{-/-}$ mice did not show clear resistance against Mtb infection and enhanced Th1 response at the four weeks post-infection period, we found that BCG vaccination in *Ch25h*$^{-/-}$ mice induced a robust memory response in an Mtb antigen-specific manner, along with enhanced IL-2 production. BCG-vaccinated *Ch25h*$^{-/-}$ mice showed significantly lower mycobacterial load and lung inflammation compared to BCG-vaccinated WT mice at six weeks post-infection. The increase in IL-2-producing effector memory T cells and IL-2 production was sustained, contributing to the maintenance of Mtb-specific immune memory. Furthermore, while the efficacies of BCG vaccination were not significantly sustained until twelve weeks post-infection point in WT mice, BCG-vaccinated *Ch25h*$^{-/-}$ mice showed a greater reduction of pulmonary CFUs, revealing that CH25H deficiency contributes to the induction of a durable, potent protective immunity against Mtb infection. Our data suggest that CH25H deficiency can induce proper immune responses to BCG *in vivo*, regulating DC activation and Th1 cell induction. These findings may provide further potential for developing novel strategies targeting 25HC or oxysterol production, which might act as crucial augmentations for improving vaccine efficacies.

2. MATERIALS AND METHODS

2.1. Ethics statements and study approval

All animal experiments followed the regulations set by the Korean Food and Drug Administration. The Ethics Committee and Institutional Animal Care and Use Committee (2018-0196; C57BL/6J, BALB/C, *Ch25h*$^{-/-}$, 2021-0159; C57BL/6J, BALB/C, *Ch25h*$^{-/-}$, P25 TCR-Tg) at Yonsei University Health System (Seoul, Korea) granted approval for each experimental protocol.

2.2. Mice

Six- to seven-week-old female C57BL/6J and BALB/C mice were obtained from Japan SLC, Inc. (Shizuoka, Japan). Six- to seven-week-old female *Ch25h*$^{-/-}$ mice were obtained from Jackson Laboratory (Sacramento, CA, USA). Six- to seven-week-old female P25 TCR-Tg mice were kindly gifted from professor Sang-Jun Ha. The mice were housed in a specific pathogen-free (SPF) environment with barriered conditions at the Yonsei University Medical Research Center SPF facility.

2.3. Bone marrow-derived cell culture

Murine BMDCs were prepared and cultured following a previously described protocol[208]. Bone marrow cells were plated in Petri dishes and cultured at 37℃ in a 5% CO2 environment. The RPMI 1640 medium was supplemented with 100 units/ml penicillin/streptomycin, 10% fetal bovine serum (FBS), 50 μM mercaptoethanol, 20 ng/ml Granulocyte-Macrophage Colony-Stimulating Factor (GM-CSF), and 5 ng/ml IL-4. In some experiments aiming for highly purified populations, DCs were labeled with bead-conjugated anti-CD11c monoclonal antibodies, followed by positive selection using paramagnetic columns (LS columns) according to the manufacturer's instructions

(Miltenyi Biotech, Bergisch Gladbach, Germany). The culture of murine bone marrow-derived macrophages (BMDMs) was conducted following a previously described protocol[209]. Isolated mouse bone marrow cells were maintained with L929-conditioned DMEM supplemented with 10% FBS and 100 units/ml of penicillin/streptomycin at 37℃ in a 5% CO2 environment for 6 days.

2.4. Mycobacterial culture and antigens

Mycobacterium bovis BCG Pasteur 1137P2 was kindly gifted from Dr. Roland Brosch. Mtb H37Rv was obtained from American Type Culture Collection (ATCC, Manassas, VA, USA). These strains were cultured in 7H9 broth supplemented with 10% oleic acid-albumin-dextrose-catalase (OADC; Difco Laboratories, Franklin Lakes, NJ, USA) for 4 weeks at 37℃. Following cultivation, all bacteria were washed three times with 10 mM phosphate-buffered saline (PBS; pH 7.4). For single-cell preparation, the mycobacterial culture was centrifuged at 3500 rpm for 20 minutes at room temperature. The supernatant was carefully discarded, and the pellet was washed twice with PBS. The pellet was resuspended in PBS, followed by bath sonication to ensure complete dispersion of the bacterial cells. The suspension was incubated in a stationary position at 36℃ for 1 hour. After incubation, the supernatant was carefully collected and passed through disposable Falcon cell strainers (Corning, Corning, NY, USA) to eliminate aggregation. The prepared suspension was aliquoted into small volumes and stored at -80℃ until further use. The detailed procedures previously described were followed meticulously[110,111,210]. Mycobacterial antigens PPD[211] and Ag85B[113] were used for stimulus, while LPS (from E. coli O111: B4) purchased from InvivoGen (San Diego, CA, USA) served as a control[116].

2.5. BCG vaccination and Mtb infection

Mice were vaccinated with BCG via subcutaneous injection (1.0×10^6 CFUs/mouse). Ten weeks after vaccination, the vaccinated mice were euthanized and autopsied for assessing immunological features or aerogenically challenged with the Mtb H37Rv strain as previously described[212]. Aerosol infection was performed using a Glas-Col aerosol apparatus (Glas-Col, Terre Haute, IN, USA) for 70 minutes, adjusted to achieve an initial infectious dose of 200 CFUs. At four, six, and twelve weeks post-challenge, mice from each group were euthanized for analysis of the bacterial load, histopathology, and immunological assays.

2.6. Preparation of single cell suspensions from mice

The mice undergoing *in vivo* analysis of immune responses and TB progression were euthanized via inhalation of carbon dioxide. Lungs and spleens of autopsied mice were obtained in order to assess bacterial load, inflammation, and immune cell distribution. According to the methods illustrated in previous studies[113,114], single-cell suspensions were harvested from the lung tissue and went through flow cytometry analysis or co-culture with DCs.

2.7. Enumeration of mycobacterial CFU and assessment of pulmonary inflammation

The lungs and spleens of Mtb-infected mice were harvested after autopsy. To enumerate mycobacterial growth, lung and spleen tissues were plated onto Middlebrook 7H10 agar (BD, Franklin Lakes, NJ, USA) after homogenization, following preparation methods from previous studies[113,116]. After a four-week incubation period at 37℃, mycobacterial colonies were counted. To enumerate lung inflammation, the right superior lobes of the lungs were kept in 10% formalin overnight for preservation and later embedded in paraffin. To perform histopathologic analysis, the lungs were sectioned at 4-5 μm and stained with hematoxylin and eosin (H&E). The degree of lung

inflammation was quantified using the ImageJ program (National Institutes of Health, USA), according to previously described references[115,213].

2.8. BMDC activation and quantification of T cell responses via DC-T cell co-culture

Splenocytes from C57BL/6J, *Ch25h*$^{-/-}$ and BALB/C mice were used for allogenic DC-T cell co-cultures. Splenocytes from P25 TCR-Tg mice and BCG-vaccinated WT mice (sacrificed ten weeks post-vaccination) were used to enumerate Mtb antigen-specific T cell proliferation and activation. CD90.2^{+} T cells were isolated from spleen cell suspensions using a MACS column. Splenic T cells were then stained with 1 μM carboxyfluorescein succinimidyl ester (CFSE) (Invitrogen, Waltham, MA, USA) according to previously described methods[208]. Subsequently, the CFSE-labeled T cells were cultured with stimulated BMDCs. The DCs were stimulated with LPS (100 ng/ml), PPD (1 μg/ml), Ag85B protein (5 μg/ml), and Ag85B peptide (1 μg/ml) with a cell ratio of 2×10^5 DCs per well, at a DC: T cell ratio of 1:10. After three days of co-culture, the T cells were stained with monoclonal antibodies against CD90.2, CD4, CD8 and CD44 and the cell proliferation rate was analyzed using a CytoFLEX S Flow cytometer (Beckman Coulter, Indianapolis, IN). Supernatants were harvested, and cytokine production from splenic T cells were quantified using mouse IFN-γ, TNF-α, IL-2, and IL-17A ELISA kits (Invitrogen, Waltham, MA, USA) as well as a mouse IL-10 ELISA kit (Biolegend, San Diego, CA, USA).

2.9. Antibodies and flow cytometry

Flow cytometry analysis of immune cells was conducted using the subsequent antibodies. LIVE/DEAD® Fixable Near-IR Dead Cell Stain Kit, Green Dead Cell Stain Kit, and Aqua Dead Cell Stain Kit were purchased from Molecular Probes (Carlsbad, CA, USA). Brilliant violet (BV) 605-conjugated mAb against Thy1.2 and CD19; Allophycocyanin (APC)-conjugated mAb against

CD45R; BV 421-conjugated mAb against CD45; APC-R700-conjugated mAb against Siglec-F; Fluorescein isothiocyanate (FITC)-conjugated mAb against CD45.2; Alexa Fluor 488-conjugated mAb against IL-17A; and V450- conjugated mAb against Ly6G were purchased from (BD, Franklin Lakes, NJ, USA). BV 421-conjugated mAb against CD86, MHC-II, KLRG1, CD44, and CD62L; BV 785-conjugated mAb against CD8; Phycoerythrin (PE)-conjugated mAb against CD80, CD64, and IFN-γ, and; Peridinin chlorophyll (PerCP)-Cy5.5-conjugated mAb against CD4 and CD11b; APC-conjugated mAb against TNF-α, Ki-67, and CD103; PE-Cy7-conjugated mAb against PD-1; APC-Cy7-conjugated mAb against MHC-II; PE-Cy7-conjugated mAb against IL-2; Alexa fluor 700-conjugated mAb against CD62L; and PE-Dazzle conjugated mAb against CD11c and CD69 were purchased from Biolegend (San Diego, CA, USA). PE-conjugated anti Ag85B specific tetramers were kindly obtained from the NIH tetramer core facility at Emory University. Surface and intracellular staining processes were executed according to the referenced study[112].

2.10. Analysis of multifunctional T cell responses

Mouse lung cells and splenocytes containing T cells were stimulated with PPD (1 μg/ml) or Ag85B (5 μg/ml) for 12 hours at 37℃. Following stimulation, supernatants and cell pellets were harvested for ELISA and flow cytometry analysis. Cell pellets underwent Fc-receptor blockade using anti-CD16/32 antibody (Biolegend, San Diego, CA, USA) before being surface-stained with BV 605-conjugated mAb against Thy1.2, PerCP-Cy5.5-conjugated mAb against CD4, BV 786-conjugated mAb against CD8, Alexa Fluor 700-conjugated mAb against CD62L, and BV 421-conjugated mAb against CD44. After surface staining, cells were permeabilized with BD Perm/Fix solution (BD, Franklin Lakes, NJ, USA) and intracellularly stained with PE-conjugated anti-IFN-γ, APC-conjugated mAb against TNF-α, and PE-Cy7-conjugated mAb against IL-2. Post-staining, cells were fixed with IC fixation buffer (Invitrogen, Waltham, MA, USA) and analyzed using a

CytoFLEX S Flow cytometer (Beckman Coulter, Brea, CA, USA). The collected supernatants were used to quantify secreted IFN-γ, TNF-α, IL-2, IL-17A, and IL-10. The analysis of cytokine secretion from the supernatants was performed using the mouse ELISA kits listed below.

2.11. Measurement of cytokines and IgG responses

For the analysis of T cell cytokines, lung single cell suspensions were stimulated with two different Mtb antigens, PPD and Ag85B according to the referenced studies[112,114]. To detect cytokines, ELISA kits were utilized. Mouse IFN-γ, TNF-α, IL-1β, IL-2, IL-12p70, and IL-17A ELISA kits were purchased from Invitrogen (Waltham, MA, USA). Mouse IL-10 ELISA kit was purchased from Biolegend (San Diego, CA, USA). For the analysis of serum IgGs, biotin-conjugated anti-mouse total IgG antibody was purchased from Sigma-Aldrich (Burlington, MA, USA). Biotin-conjugated anti-mouse IgG1 and IgG2c antibodies were obtained from Biowest (Bradenton, FL, USA). Anti-biotin HRP and substrate solution were purchased from Invitrogen (Waltham, MA, USA).

2.12. Statistical analyses

The results were presented as the mean ± standard deviation (SD). To analyze the significance of differences between two selected groups, unpaired *t*-test and Mann-Whitney U test was conducted. To analyze the significance of differences between more than two selected groups, ANOVA test was conducted. GraphPad Prism version 8 for Windows (GraphPad Software, La Jolla, CA, USA, www.graphpad.com) was adapted for statistical analysis. The statistical significance was determined using the following definitions: *n.s.*: not significant, *$p < 0.05$, **$p < 0.01$, **$p <0.01$, ***$p < 0.001$, ****$p < 0.0001$.

3. RESULTS

3.1. *Ch25h*$^{-/-}$ *DCs* feature more activated phenotype with Th1-inducing characteristics

We first aimed to investigate the impact of CH25H deficiency in DCs *in vitro*. BMDCs from both WT and *Ch25h*$^{-/-}$ mice were generated with GM-CSF stimulation. After 8 days of culture, the cells were harvested and stimulated with LPS or mycobacterial antigens PPD and Ag85B to assess the expression of surface markers and cytokine production **(Figure 1A)**. Harvested BMDCs were gated and analyzed according to the gating strategies attached **(Figure 2A, 2B)**. We confirmed that CH25H deficiency does not affect the differentiation of BMDCs, as the purity of BMDCs was not significantly altered **(Figure 1B)**. Remarkably, *Ch25h*$^{-/-}$ BMDCs displayed increased expression of co-stimulatory molecules CD80 and CD86 compared to WT BMDCs after stimulation with LPS, Mtb antigens PPD and Ag85B, and BCG **(Figure 1C)**. On the other hand, the expression of MHC-I and MHC-II did not notably increase in *Ch25h*$^{-/-}$ BMDCs after stimulation **(Figure 1D)**. Additionally, stimulated *Ch25h*$^{-/-}$ BMDCs displayed increased secretion of IL-12p70, IL-1 α, and IL-1β, coupled with decreased production of IL-10, indicating the potential to influence T cells toward Th1 phenotypes **(Figure 1E)**. Meanwhile, the secretion of TNF-α, IL-6, IL-23, and TGF- β were not significantly altered in stimulated *Ch25h*$^{-/-}$ BMDCs **(Figure 2C)**. Furthermore, although stimulated *Ch25h*$^{-/-}$ BMDMs produced more IL-1β compared to WT BMDMs as previously reported[186], they did not exhibit decreased IL-10 production and did not produce IL-12p70 in response to antigen stimulation **(Figure 2D)**. Therefore, we hypothesize that DCs, rather than macrophages, are the primary immune cells responsible for significantly altering adaptive immune responses in Mtb-infected *Ch25h*$^{-/-}$ mice. Our findings suggest that CH25H deficiency strongly affects DC responses to antigen stimulation, potentially directing naïve T cells toward Th1 cell differentiation.

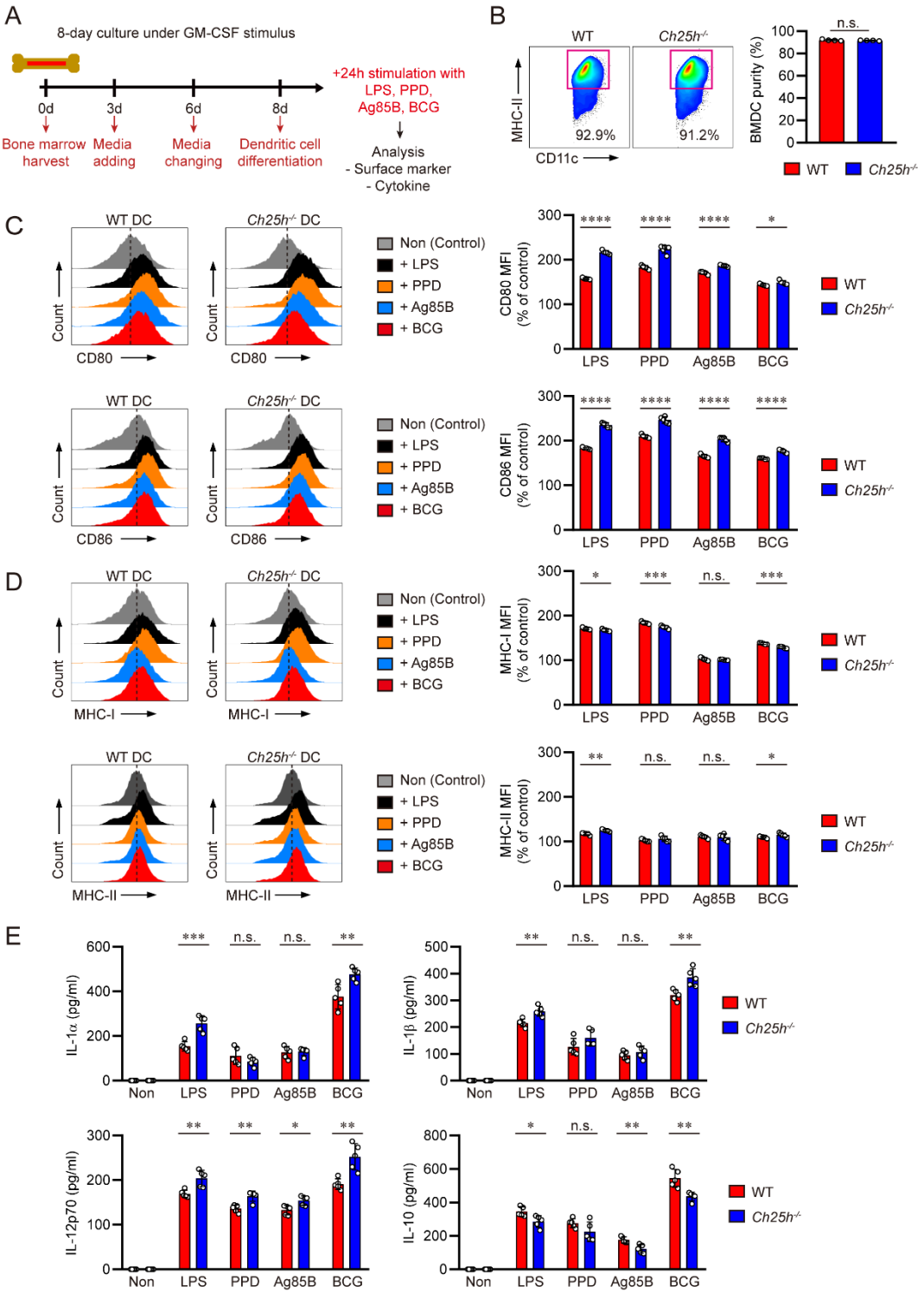

Figure 1. Comparative expression profiles of co-stimulatory molecules and cytokine productions in BMDCs from *Ch25h*$^{-/-}$ and WT mice in response to BCG and mycobacterial antigens. (A) Experimental design for *in vitro* analysis of BMDC differentiation with WT and *Ch25h*$^{-/-}$ mice. **(B)** The purity of harvested CD11c^{+}MHC-II^{+} BMDCs. **(C)** Relative Mean Fluorescence Intensity (MFI) values (% of unstimulated controls) of CD80 and CD86 in BMDCs. **(D)** Relative MFI values (% of unstimulated controls) of MHC-I and MHC-II in BMDCs after stimulation. **(E)** The expression levels of IL-1α, IL-1β, IL-12p70, and IL-10 in supernatants of stimulated BMDCs are. The data are presented as the mean ± SD of five mice in each group. The significance of differences was determined, using an unpaired *t*-test. *n.s.*; not significant, **p* <0.05, ***p* <0.01, ****p* < 0.001, *****p* < 0.0001

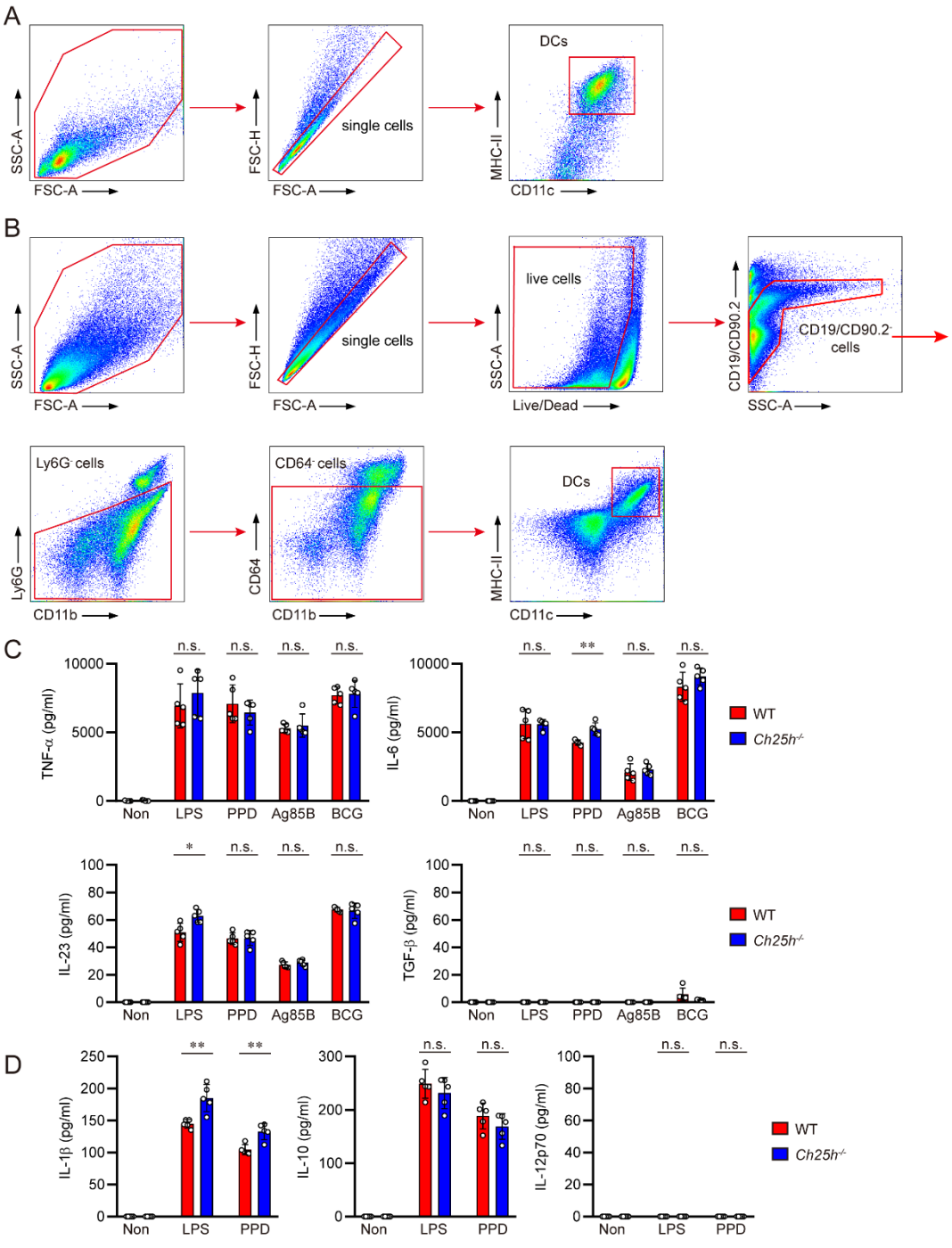

Figure 2. Gating strategies for DCs and additional properties of *Ch25h*$^{-/-}$ BMDCs and BMDMs.

(A) *In vitro* flow cytometry gating strategy for BMDCs. **(B)** *In vivo* flow cytometry gating strategy for pulmonary DCs. **(C)** The expression levels of TNF-α, IL-6, IL-23 and TGF-β in the supernatants of stimulated BMDCs. **(D)** The expression levels of IL-1β, IL-10, and IL-12p70 in the supernatants of stimulated BMDCs. The data are presented as the mean ± SD of four mice in each group. The significance of differences was determined, using an unpaired *t*-test. *n.s.*; not significant, **p* <0.05, ***p* <0.01

3.2. CH25H deficiency in DCs, rather than in T cells, has the potential to induce rapid proliferation and Th1 polarization of $CD4^+$ T cells

We observed that *Ch25h*$^{-/-}$ DCs feature enhanced expression of co-stimulatory molecules and cytokine production in response to antigenic stimulus. To confirm whether *Ch25h*$^{-/-}$ DCs can polarize T cells into Th1 type and whether CH25H deficiency can alter T cell responses independently from DC functions, we conducted co-culture experiments using DCs and T cells from allogeneic mice. BMDCs and splenic T cells were obtained from WT, *Ch25h*$^{-/-}$, and BALB/c mice. In the first experiment, WT and *Ch25h*$^{-/-}$ BMDCs were co-cultured with BALB/c splenic T cells to initiate allogeneic T cell responses. In the second experiment, WT and *Ch25h*$^{-/-}$ splenic T cells were co-cultured with BALB/c BMDCs. DCs were stimulated with PPD for 24 hours before co-culturing with allogeneic T cells, which were stained with CFSE. After 3 days of co-culture, cells and supernatants were harvested to investigate T cell proliferation and cytokine production **(Figure 3A)**. Co-cultured T cells were gated and analyzed according to the gating strategies attached **(Figure 4).** Compared to WT DCs, *Ch25h*$^{-/-}$ DCs more induced spontaneous proliferation of BALB/C T cells. $CD4^+$ and $CD8^+$ T cells incubated with *Ch25h*$^{-/-}$ DCs exhibited a greater proliferation than WT DCs. **(Figure 3B)**. Furthermore, BALB/c T cells incubated with *Ch25h*$^{-/-}$ DCs produced more IFN-γ, TNF-α, and IL-2 after co-culture, while IL-10 production was not significantly different from T cells incubated with WT DCs. **(Figure 3C)**. In contrast, there was no clear difference in proliferation between WT and *Ch25h*$^{-/-}$ T cells incubated with BALB/c DCs **(Figure 3D)**. In addition, *Ch25h*$^{-/-}$ T cells incubated with BALB/C DCs did not show significant upregulation of Th1 cytokines compared to WT T cells **(Figure 3E)**. We also determined that unstimulated *Ch25h*$^{-/-}$ DCs are not capable of inducing T cell proliferation and Th1 cytokine production, suggesting that antigenic stimulus is essential for the initiation of DC-mediated T cell activation in CH25H-deficient conditions **(Figure 5)**. In addition, we confirmed that *Ch25h*$^{-/-}$ BMDCs treated with BCG can also facilitate T cell

proliferation and Th1 cytokine production **(Figure 6)**. Therefore, we concluded that CH25H deficiency in DCs is crucial for the rapid Th1 polarization of naïve T cells, rather than CH25H deficiency in T cells themselves.

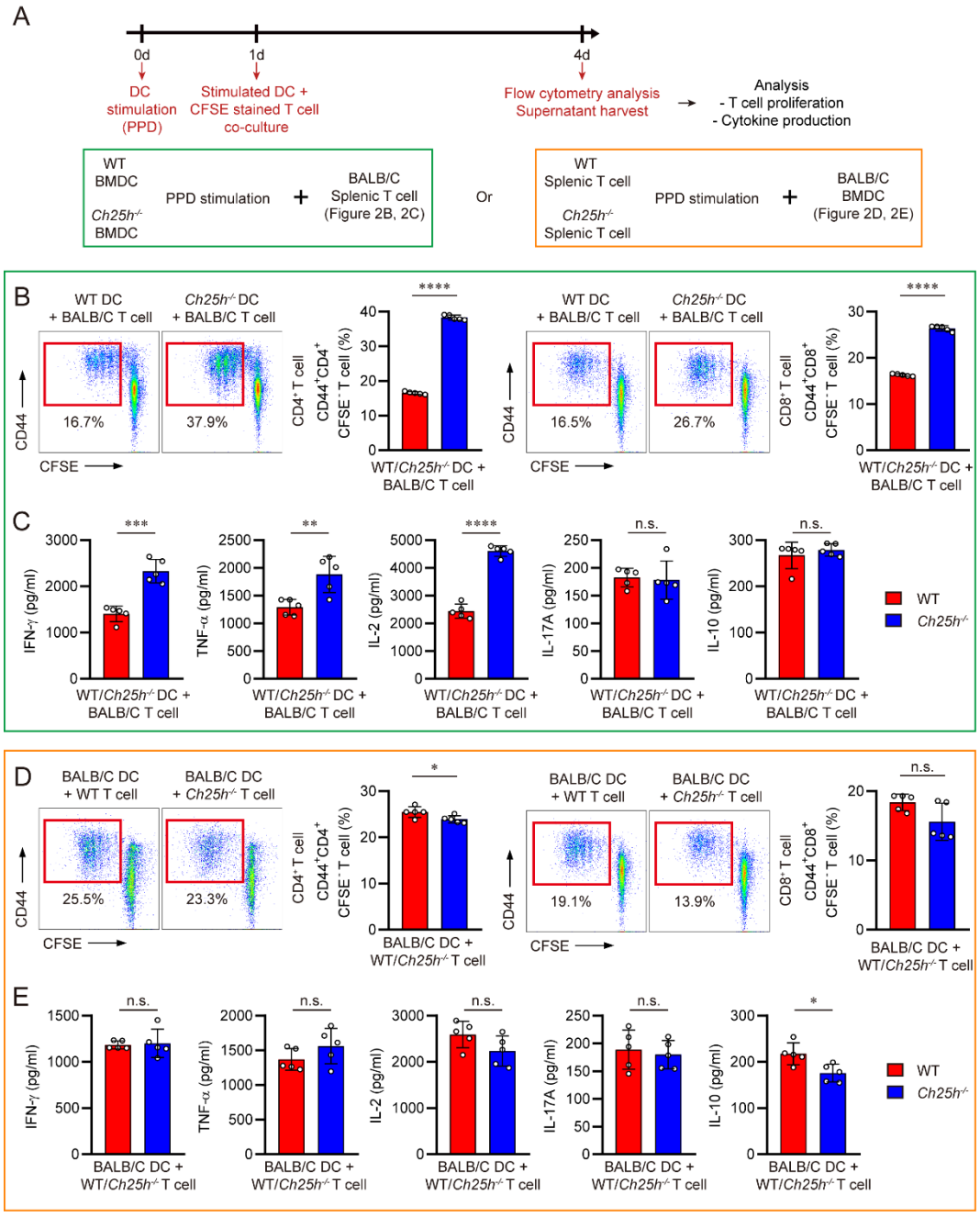

Figure 3. T cell proliferation and cytokine production status of splenic T cells co-cultured with stimulated WT and *Ch25h*$^{-/-}$ BMDCs. (A) Experimental scheme for DC-T cell co-culture assay. WT and *Ch25h*$^{-/-}$ BMDCs were stimulated with Ag85B and co-cultured with CFSE stained splenic T cells. After three days of co-culture, flow cytometry analysis and ELISA were performed. **(B)** $CD4^+$ and $CD8^+$ T cell proliferation status in BALB/C splenic T cells incubated with WT BMDC or *Ch25h*$^{-/-}$ BMDCs. **(C)** The expression levels of IFN-γ, TNF-α, IL-2, IL-17A, and IL-10 in supernatants of BALB/C splenic T cells incubated with WT BMDC or *Ch25h*$^{-/-}$ BMDCs. **(D)** $CD4^+$ and $CD8^+$ T cell proliferation status in BALB/C BMDCs incubated with WT splenic T cells or *Ch25h*$^{-/-}$ splenic T cells. **(E)** The expression levels of IFN-γ, TNF-α, IL-2, IL-17A, and IL-10 in supernatants of BALB/C BMDCs incubated with WT splenic T cells or *Ch25h*$^{-/-}$ splenic T cells. The data are presented as the mean ± SD of five mice in each group. The significance of differences was determined, using unpaired *t*-test. *n.s.*, not significant. **p* <0.05, ***p* <0.01, ****p* < 0.001, *****p* < 0.0001

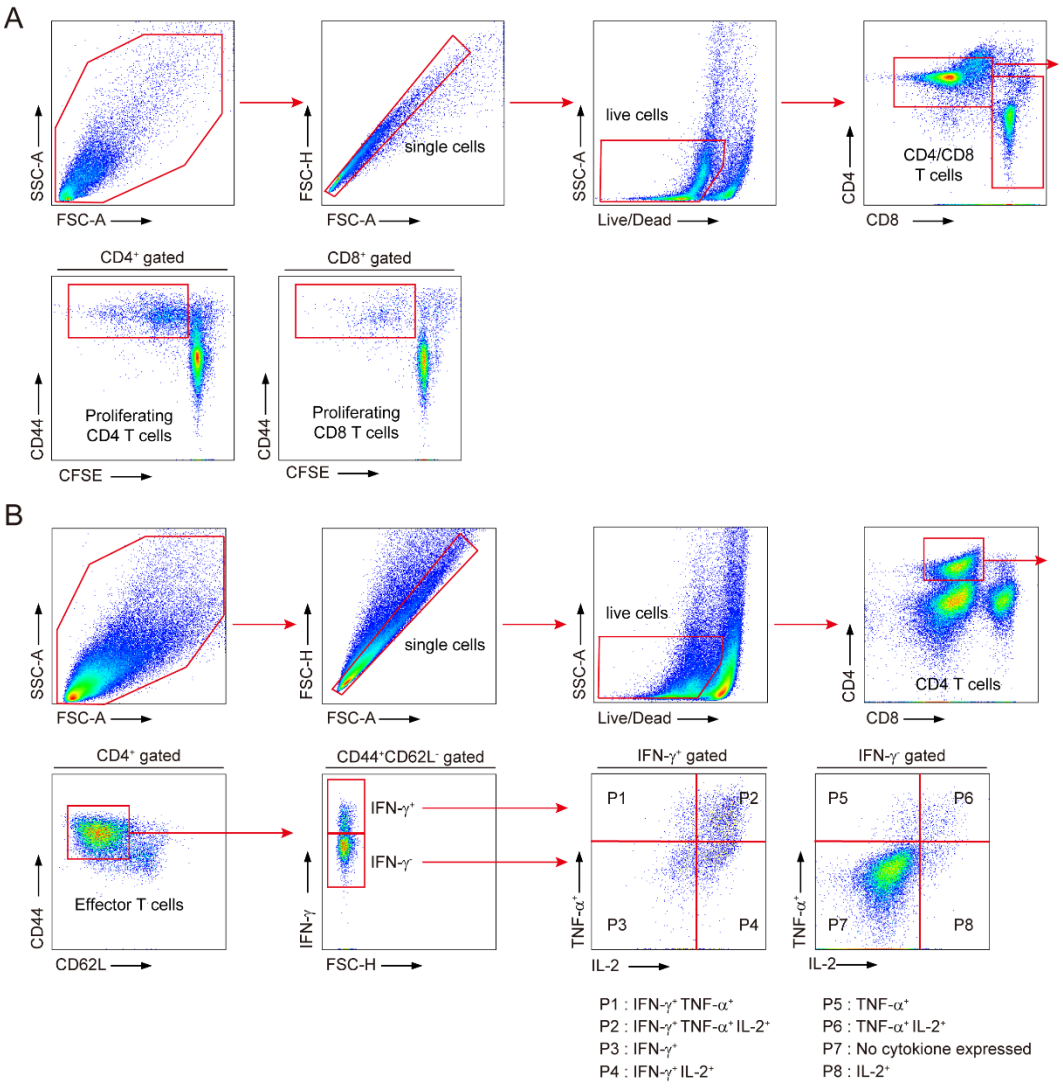

Figure 4. Gating strategies for T cells. (A) *In vitro* flow cytometry gating strategy for T cells co-cultured with BMDCs. **(B)** *In vivo* flow cytometry gating strategy for pulmonary cytokine producing T cells.

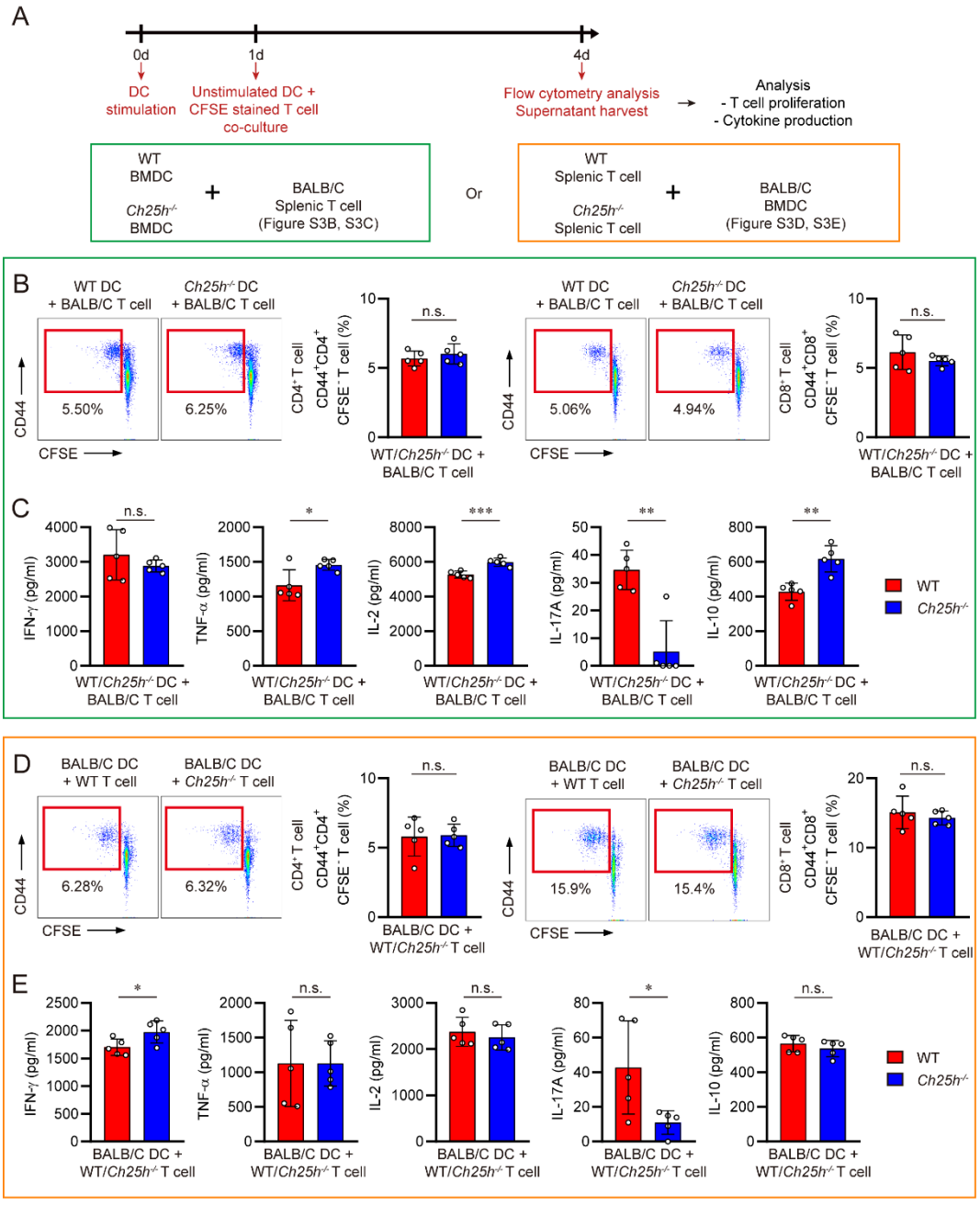

Figure 5. T cell proliferation and cytokine production status of splenic T cells co-cultured with unstimulated WT and *Ch25h*$^{-/-}$ DCs. (A) Experimental scheme for unstimulated DC-T cell co-culture assay is. Unstimulated WT and *Ch25h*$^{-/-}$ BMDCs were co-cultured with CFSE stained splenic T cells. After three days of co-culture, flow cytometry analysis and ELISA were performed. **(B)** $CD4^+$ and $CD8^+$ T cell proliferation status in BALB/C splenic T cells incubated with WT BMDC or *Ch25h*$^{-/-}$ BMDCs. **(C)** The expression levels of IFN-γ, TNF-α, IL-2, IL-17A, and IL-10 in supernatants of BALB/C splenic T cells incubated with WT BMDC or *Ch25h*$^{-/-}$ BMDCs. **(D)** $CD4^+$ and $CD8^+$ T cell proliferation status in BALB/C BMDCs incubated with WT splenic T cells or *Ch25h*$^{-/-}$ splenic T cells. **(E)** The expression levels of IFN-γ, TNF-α, IL-2, IL-17A, and IL-10 in supernatants of BALB/C BMDCs incubated with WT splenic T cells or *Ch25h*$^{-/-}$ splenic T cells. The data are presented as the mean ± SD of five mice in each group. The significance of differences was determined, using unpaired *t*-test. *n.s.*, not significant. **p* <0.05. ***p* <0.01, ****p* < 0.001

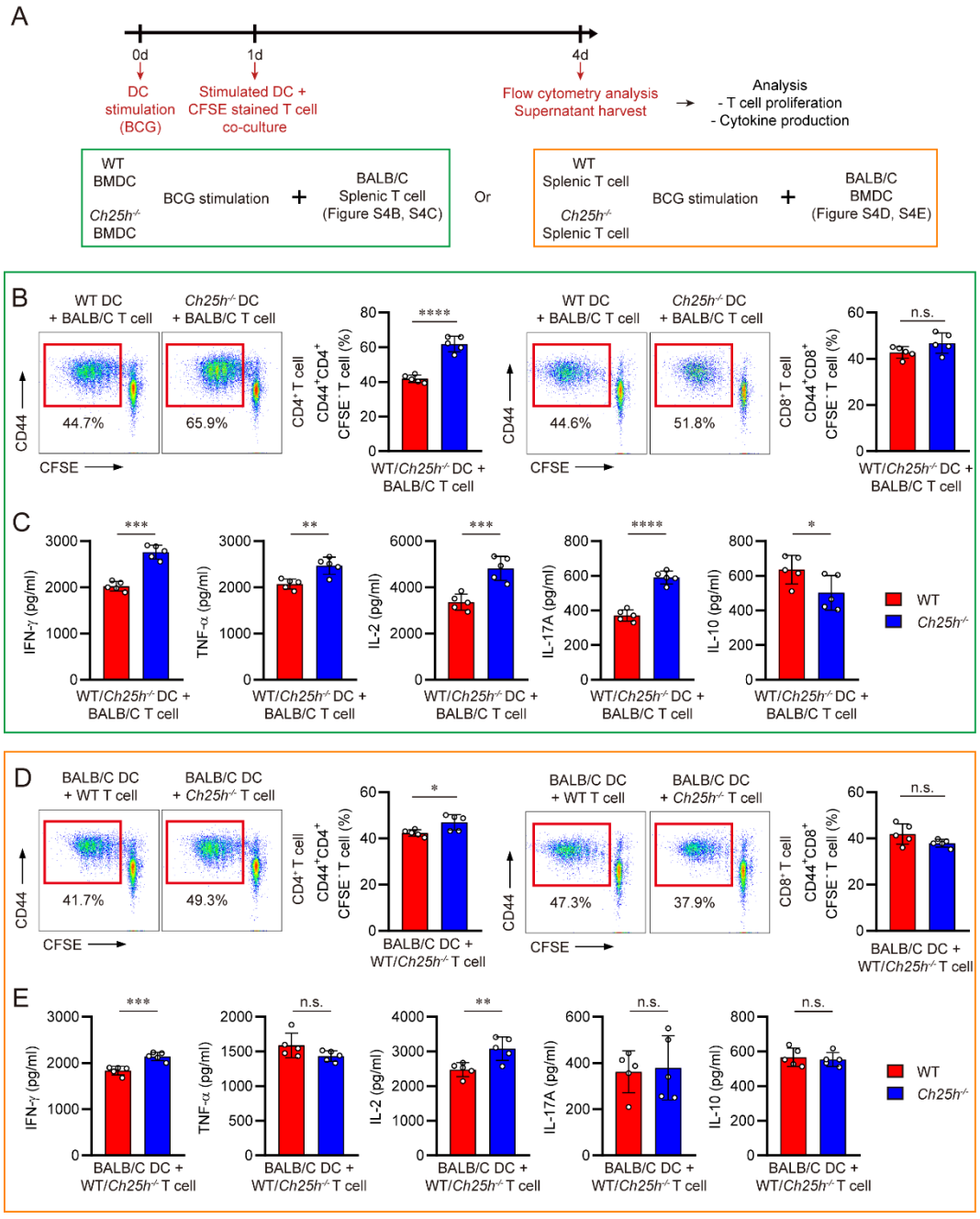

Figure 6. T cell proliferation and cytokine production status of splenic T cells co-cultured with BCG-infected WT and *Ch25h*$^{-/-}$ BMDCs. (A) Experimental scheme for DC-T cell co-culture assay. WT and *Ch25h*$^{-/-}$ BMDCs were stimulated with BCG and co-cultured with CFSE stained splenic T cells. After three days of co-culture, flow cytometry analysis and ELISA were performed. **(B)** $CD4^+$ and $CD8^+$ T cell proliferation status in BALB/C splenic T cells incubated with WT BMDC or *Ch25h*$^{-/-}$ BMDCs. **(C)** The expression levels of IFN-γ, TNF-α, IL-2, IL-17A, and IL-10 in supernatants of BALB/C splenic T cells incubated with WT BMDC or *Ch25h*$^{-/-}$ BMDCs are represented. **(D)** $CD4^+$ and $CD8^+$ T cell proliferation status in BALB/C BMDCs incubated with WT splenic T cells or *Ch25h*$^{-/-}$ splenic T cells. **(E)** The expression levels of IFN-γ, TNF-α, IL-2, IL-17A, and IL-10 in supernatants of BALB/C BMDCs incubated with WT splenic T cells or *Ch25h*$^{-/-}$ splenic T cells. The data are presented as the mean ± SD of five mice in each group. The significance of differences was determined, using unpaired *t*-test. *n.s.*, not significant. **p* <0.05, ***p* <0.01, ****p* < 0.001, *****p* < 0.0001

3.3. CH25H-deficient DCs are highly effective at inducing T cell proliferation and Th1 polarization of Mtb-specific CD4$^+$ T cells

Since we discovered that CH25H deficiency in DCs is crucial for inducing Th1 polarization and T cell proliferation through allogenic DC-T cell co-culture assays, we aimed to determine whether CH25H-deficient DCs can also activate Mtb-specific T cells. To assess whether *Ch25h*$^{-/-}$ DCs can activate Mtb-specific T cells, we designed two independent DC-T cell co-culture assay models. In the first model, we utilized P25 TCR-Tg mice, which contain CD4$^+$ T cells expressing a transgenic T cell antigen receptor that recognizes peptide 25 (aa 240-254) of the Mtb antigen Ag85B[201,214]. Splenic T cells from P25 TCR-Tg mice were co-cultured with WT and *Ch25h*$^{-/-}$ BMDCs activated with the Ag85B peptide. In the second model, we harvested splenic T cells from BCG-vaccinated WT mice ten weeks post-vaccination. BCG-challenged splenic T cells were co-cultured with WT and *Ch25h*$^{-/-}$ BMDCs stimulated with PPD. Splenic T cells were stained with CFSE and co-cultured with the stimulated DCs for 3 days. Cells and supernatants were harvested to assess T cell proliferation and cytokine production **(Figure 7A).** We found that *Ch25h*$^{-/-}$ DCs induced spontaneous proliferation of P25 CD4$^+$ T cells **(Figure 7B)** and upregulated the expression of IFN-γ, IL-2, and IL-17A while downregulating the expression of IL-10 **(Figure 7C)**. Similar results were observed when *Ch25h*$^{-/-}$ DCs were co-cultured with splenic T cells from BCG-vaccinated mice. *Ch25h*$^{-/-}$ DCs significantly increased the proliferation of BCG-vaccinated CD4$^+$ T cells **(Figure 7D)**, upregulated IFN-γ, IL-2, and IL-17A expression, and downregulated IL-10 expression **(Figure 7E)**. In conclusion, we demonstrated that CH25H-deficient DCs are highly effective at promoting T cell proliferation and Th1 polarization of Mtb-specific T cells.

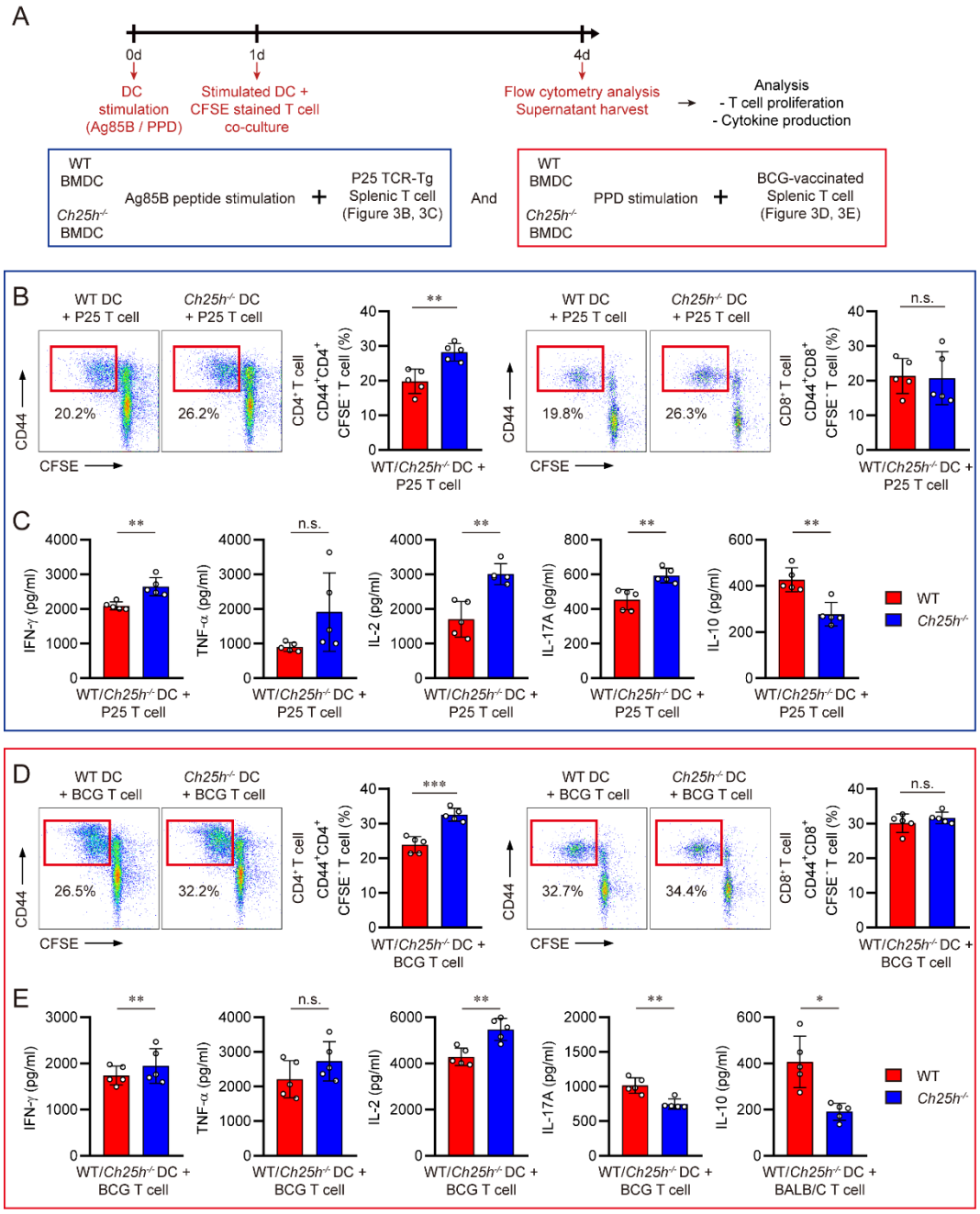

Figure 7. T cell proliferation and cytokine production status of Mtb-specific splenic T cells co-cultured with stimulated WT and *Ch25h*$^{-/-}$ BMDCs. (A) Experimental scheme for DC-T cell co-culture assay. WT and *Ch25h*$^{-/-}$ BMDCs were stimulated with Ag85B peptide or PPD and co-cultured with CFSE stained splenic T cells from P25 TCR-Tg mice or BCG-vaccinated WT mice (sacrificed at ten weeks post-vaccination). After three days of co-culture, flow cytometry analysis and ELISA were performed. **(B)** $CD4^+$ and $CD8^+$ T cell proliferation status in P25 TCR-Tg splenic T cells incubated with WT BMDC or *Ch25h*$^{-/-}$ BMDCs. **(C)** The expression levels of IFN-γ, TNF-α, IL-2, IL-17A, and IL-10 in supernatants of P25 TCR-Tg splenic T cells incubated with WT BMDC or *Ch25h*$^{-/-}$ BMDCs. **(D)** $CD4^+$ and $CD8^+$ T cell proliferation status in BCG-vaccinated WT splenic T cells incubated with WT BMDC or *Ch25h*$^{-/-}$ BMDCs. **(E)** The expression levels of IFN-γ, TNF-α, IL-2, IL-17A, and IL-10 in supernatants of BCG-vaccinated WT splenic T cells incubated with WT BMDC or *Ch25h*$^{-/-}$ BMDCs. The data are presented as the mean ± SD of five mice in each group. The significance of differences was determined, using unpaired *t*-test. *n.s.*, not significant. **p* <0.05, ***p* <0.01, ****p* < 0.001

0.001

3.4. BCG vaccination elicits greater antigen-specific T cell responses in *Ch25h*$^{-/-}$ mice than WT mice

Based on above results, we first explored whether the immunological changes induced by CH25H deficiency can enhance anti-TB immune responses during the course of Mtb infection by comparing WT and *Ch25h*$^{-/-}$ mice after infection with the Mtb H37Rv strain. At four weeks post-infection, the mice were euthanized to assess the severity of TB and immune functions. We observed that pulmonary bacterial load, spleen bacterial load, and lung inflammation were not significantly altered in Mtb-infected *Ch25h*$^{-/-}$ mice at this time point **(Figure 8)**. While the numbers of pulmonary DCs and CD86 expression were upregulated in *Ch25h*$^{-/-}$ mice, there was no significant difference in antigen-specific immune responses against mycobacterial antigens PPD and Ag85B. The proportions of multifunctional (IFN-γ^+ TNF-α^+, IFN-γ^+ IL-2^+, IFN-γ^+ TNF-α^+ IL-2^+) pulmonary $CD4^+$ T cells**,** the numbers of IFN-γ, TNF-α, and IL-2 positive $CD4^+$ T cells, and the expression of cytokines including IFN-γ, TNF-α, IL-2, and IL-10 were not significantly increased in the lungs of Mtb infected *Ch25h*$^{-/-}$ mice **(Figure 9)**. Even more surprisingly, although CH25H is reported to be a remarkable ISG, and the expression of ISGs is correlated with the progression of TB in various studies[205,206], induction of type I IFN signaling through intratracheal Poly I:C treatment still exacerbated TB in *Ch25h*$^{-/-}$ mice **(Figure 10)**. These results indicated that type I IFN-mediated expression of CH25H does not significantly affect disease progression in the model of pulmonary Mtb infection. Although *Ch25h*$^{-/-}$ mice failed to demonstrate enhanced protection against Mtb at four weeks post-infection, we hypothesized that *Ch25h*$^{-/-}$ DCs may have the potential to induce more robust antigen-specific Th1-type T-cell immune memory against Mtb *in vivo*, as they were able to induce a greater T cell proliferation and Th1 cytokine productions than WT DCs as shown in Figure 2 and 3. Particularly, distinct upregulation of IL-2 from T cells activated by *Ch25h*$^{-/-}$ DCs provided us novel clues about the role of CH25H deficiency in boosting anti-TB immunity. Considering that

IL-2 plays a significant role in anti-TB immunity, particularly in activating and proliferating Mtb-specific $CD4^+$ T cells [215,216], we hypothesized that enhanced DC functions and DC-mediated memory T cell activation might contribute to effective protection against Mtb. We also postulated that enhanced Th1 responses via DC activation reinforced by CH25H deficiency may enhance the efficacy of BCG vaccination, as suggested by studies emphasizing the role of IL-2 in maintaining strong vaccination-induced antigen-specific immune responses[217-219]. To confirm whether CH25H deficiency alters memory responses induced by BCG vaccination, we subcutaneously vaccinated both WT and *Ch25h*$^{-/-}$ mice with BCG. At ten weeks post-vaccination, the mice were euthanized to assess the severity of TB and immune functions **(Figure 11A)**. We observed that BCG-vaccinated *Ch25h*$^{-/-}$ mice exhibited an increased number of pulmonary $CD44^{hi}CD62L^{lo}$ effector T cells, featuring higher expression of CD44 **(Figure 11B)**. We also figured out that Ag85B-specific $CD4^+$ T cells and $CD69^+CD103^+$ residential memory $CD4^+$ T cells were increased in the lungs of BCG-vaccinated *Ch25h*$^{-/-}$ mice **(Figure 11C)**. Furthermore, effector T cells from BCG-vaccinated *Ch25h*$^{-/-}$ mice exhibited increased Ki-67 expression, a potential marker indicating heightened T cell proliferation[220,221]. They also featured decreased KLRG1 expression, another characteristic of highly proliferative T cells[222,223] **(Figure 11D)**. Pulmonary T cells of BCG-vaccinated *Ch25h*$^{-/-}$ mice also displayed significant differences in cytokine-producing profiles in response to mycobacterial antigens PPD and Ag85B. The proportions of multifunctional (IFN-γ^+TNF-α^+, IFN-γ^+IL-2^+, IFN-γ^+TNF-α^+IL-2^+) pulmonary $CD4^+$ T cells **(Figure 11E)** and the numbers of IFN-γ, TNF-α, and IL-2 positive $CD4^+$ T cells **(Figure 11F)** were increased in BCG-vaccinated *Ch25h*$^{-/-}$ mice. Induction of Mtb-specific immune responses were also observed in a cytokine level, as the expression of IFN-γ, TNF-α, and IL-2 were increased in lung cells as well. Notably, IL-2 production was significantly upregulated in *Ch25h*$^{-/-}$ mice, suggesting its potential role in the rapid proliferation of antigen-specific multifunctional T cells. However, the expression of IL-10 was decreased in *Ch25h*$^{-/-}$ mice

(Figure 11G). Meanwhile, although the number of pulmonary DCs and CD86 expression on DCs increased in BCG-vaccinated vaccinated *Ch25h*$^{-/-}$ mice, CD80 expression was not significantly altered **(Figure 12A)**. Humoral responses against Mtb antigens were not strongly induced in BCG vaccinated *Ch25h*$^{-/-}$ mice, as the induction of PPD and Ag85B specific IgGs were not significantly increased **(Figure 12B)**. These findings suggest that CH25H restricts the optimal induction of anti-TB immune memory in response to BCG vaccination.

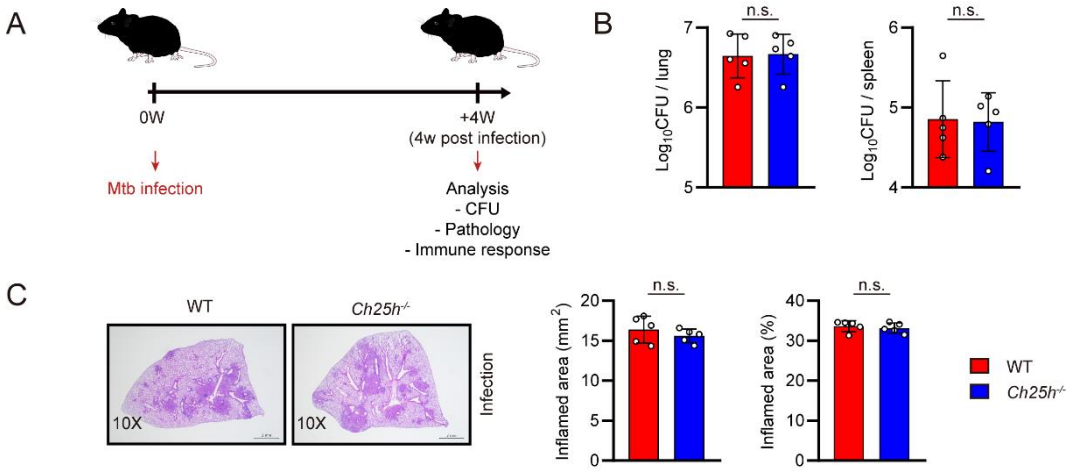

Figure 8. Status of TB progression in WT and *Ch25h*$^{-/-}$ mice, represented by lung inflammation and mycobacterial load at four weeks post-infection. (A) Experimental scheme for *in vivo* Mtb challenge. **(B)** CFUs of lungs and spleen and **(C)** lung pathology of Mtb-infected WT and *Ch25h*$^{-/-}$ mice. H&E staining was performed on the superior lobes of the right lung at four weeks post-infection to visualize the gross lung pathology. The data are presented as the mean ± SD of five mice in each group. The significance of differences was determined, using the Mann-Whitney U test. *n.s.*, not significant.

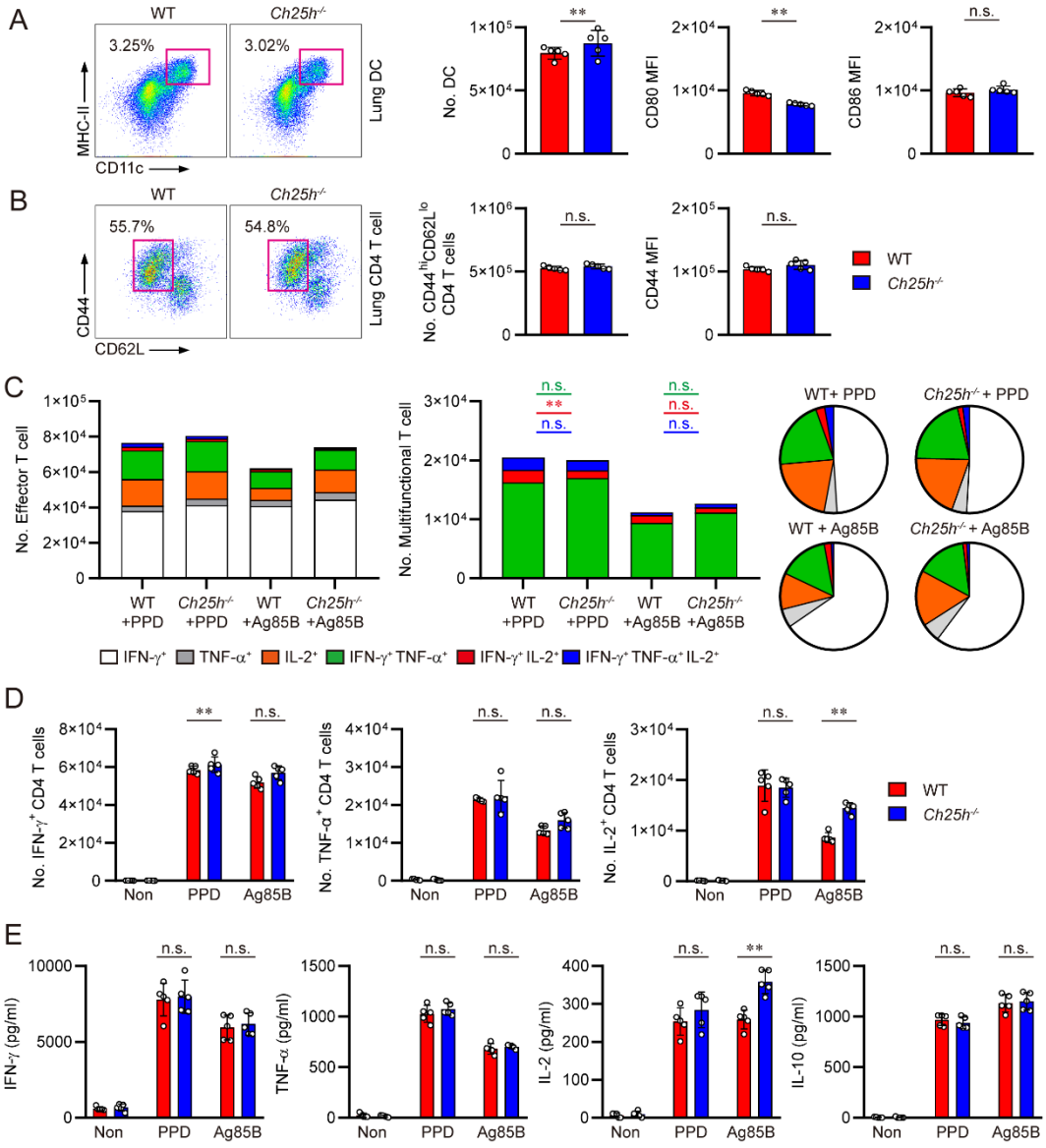

Figure 9. Immunological profiles of pulmonary DCs and CD4$^+$ T cells in WT and *Ch25h*$^{-/-}$ mice analysed at four weeks post-infection. (A) Flow cytometry analysis of pulmonary DCs of Mtb-infected at four weeks post-infection. **(B)** Flow cytometry analysis of pulmonary effector CD4$^+$ T cells. **(C)** The frequencies of Mtb-specific pulmonary multifunctional T cells, represented by the percent of each cytokine positive T cell among the total cytokine positive T cells. Green bars indicate statistical significance between IFN-γ$^+$ TNF-α$^+$ CD4$^+$ T cells, red bars indicate statistical significance between IFN-γ$^+$ IL-2$^+$ CD4$^+$ T cells, and blue bars indicate statistical significance between IFN-γ$^+$ TNF-α$^+$ IL-2$^+$ CD4$^+$ T cells. **(D)** The numbers of Mtb-specific IFN-γ$^+$, TNF-α$^+$, and IL-2$^+$ CD4$^+$ T cells. **(E)** The levels of IFN-γ, TNF-α, IL-2, IL-17A, and IL-10 in the supernatant of antigen stimulated Mtb-infected lung cells in WT and *Ch25h*$^{-/-}$ mice. The data are presented as the mean ± SD of five mice in each group. The significance of differences was determined, using the Mann-Whitney U test. *n.s.*, not significant. ***p* <0.01

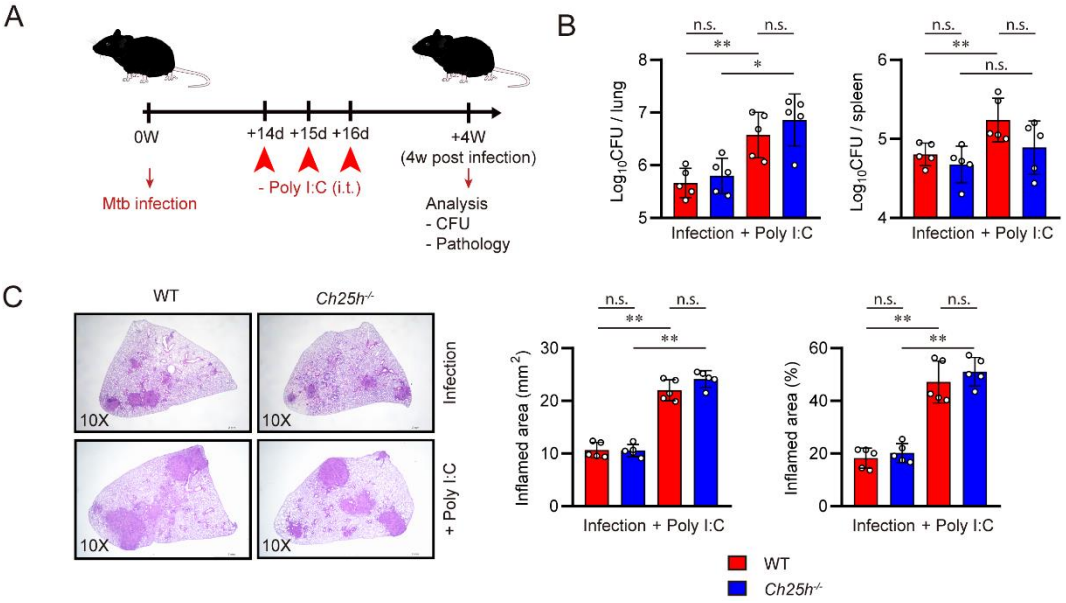

Figure 10. Status of TB progression in WT and *Ch25h*$^{-/-}$ mice treated with Poly I:C, represented by lung inflammation and mycobacterial load at four weeks post-infection. (A) The experimental scheme for *in vivo* Poly I:C treatment in Mtb-infected mice. Starting at fourteen days post-infection, 200 μg of Poly I:C was administered intratracheally to the mice. The injections were performed once daily for a total of three treatments, from fourteen to sixteen days post-infection. **(B)** CFUs of lungs and spleen and **(C)** lung pathology of Mtb-infected WT and *Ch25h*$^{-/-}$ mice. H&E staining was performed on the superior lobes of the right lung at four weeks post-infection to visualize the gross lung pathology. The data are presented as the mean ± SD of five mice in each group. The significance of differences was determined, using the ANOVA test. *n.s.*, not significant, **p* <0.05, ***p* <0.01

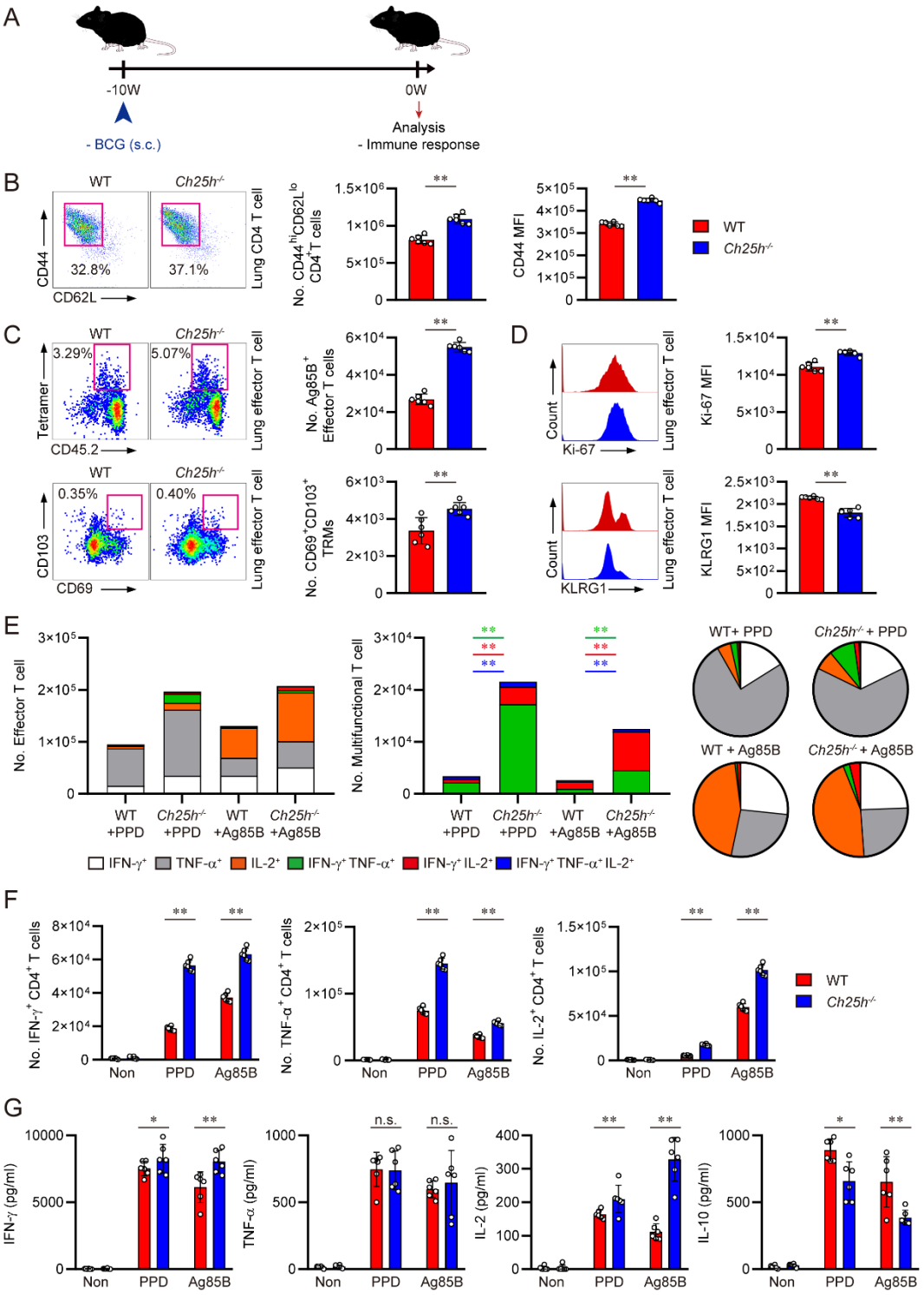

Figure 11. Immunological profiles of pulmonary CD4$^+$ T cells in BCG-vaccinated, uninfected WT and *Ch25h*$^{-/-}$ mice. (A) Experimental scheme for *in vivo* vaccination of BCG. **(B)** Flow cytometry analysis of pulmonary effector CD4$^+$ T cells. **(C)** Flow cytometry analysis of pulmonary Ag85B-specific CD4$^+$ T cells and CD69$^+$CD103$^+$ TRMs. **(D)** MFI values of Ki-67 and KLRG1 in pulmonary effector T cells. **(E)** The frequencies of Mtb-specific pulmonary multifunctional T cells, represented as.the percent of each cytokine positive T cell among the total cytokine positive T cells. Green bars indicate the statistical significance between IFN-γ$^+$ TNF-α$^+$ CD4$^+$ T cells, red bars indicate the statistical significance between IFN-γ$^+$ IL-2$^+$ CD4$^+$ T cells, and blue bars indicate the statistical significance between IFN-γ$^+$ TNF-α$^+$ IL-2$^+$ CD4$^+$ T cells. **(F)** The numbers of Mtb-specific IFN-γ$^+$, TNF-α$^+$, and IL-2$^+$ CD4$^+$ T cells. **(G)** The levels of IFN-γ, TNF-α, IL-2, IL-17A, and IL-10 in the supernatant of antigen stimulated Mtb-infected lung cells in WT and *Ch25h*$^{-/-}$ mice. The data are presented as the mean ± SD of six mice in each group. The significance of differences was determined, using the Mann-Whitney U test. *n.s.*, not significant. **p* <0.05, ***p* <0.01

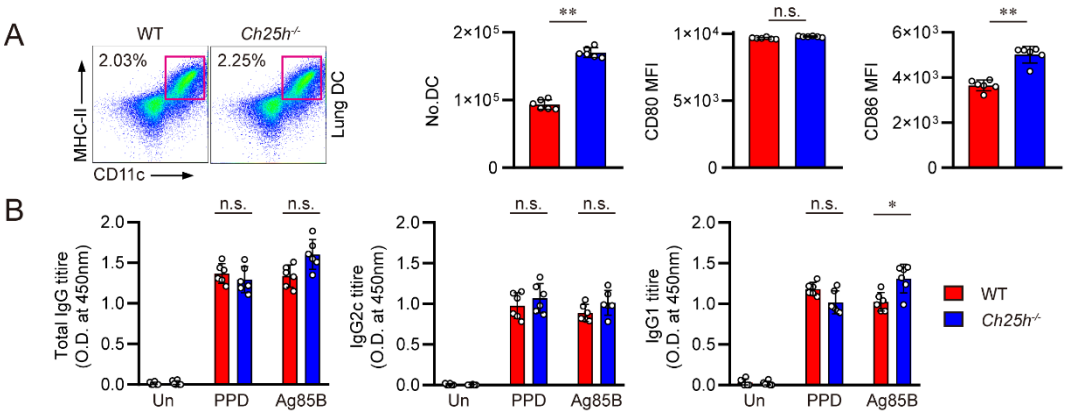

Figure 12. Additional immune profiles of BCG-vaccinated WT and *Ch25h*$^{-/-}$ mice. (A) Flow cytometry analysis of pulmonary DCs. **(B)** Total IgG, IgG1, and IgG2c status in BCG vaccinated mice. The data are presented as the mean ± SD of six mice in each group. The significance of differences was determined, using Mann-Whitney U test. *n.s.*, not significant, **p* <0.05, ***p* <0.01

3.5. BCG vaccination-induced Mtb-specific lung effector T cells provide improved protection against Mtb in *Ch25h*$^{-/-}$ mice at six weeks post-infection

We confirmed that BCG vaccination can induce intact immune memory against Mtb in *Ch25h*$^{-/-}$ mice. We aimed to investigate whether CH25H deficiency enhances the protective efficacy of BCG vaccination *in vivo*, and whether it contributes to the long-term maintenance of protection against Mtb. As clinical reports indicate that the efficacy of BCG diminishes during the later stages of Mtb infection[224,225], we infected BCG-vaccinated WT and *Ch25h*$^{-/-}$ mice with Mtb at ten weeks post-vaccination and assessed the degree of TB progression and immune responses at two different time points. We initially aimed to determine whether BCG-vaccinated *Ch25h*$^{-/-}$ mice exhibit improved protection against at six weeks post-infection, which represents a comparatively earlier time point. At this time point, the mice were euthanized to assess the severity of TB and immune functions **(Figure 13A)**. While no discernible disparity in TB progression was observed between unvaccinated WT and *Ch25h*$^{-/-}$ mice, a notable reduction in CFU and lung inflammation were evident in BCG-vaccinated *Ch25h*$^{-/-}$ mice compared to WT mice. Mycobacterial CFUs in the lungs and spleens **(Figure 13B)** and lung inflammation **(Figure 13C)** in BCG-vaccinated *Ch25h*$^{-/-}$ mice were decreased when compared to WT mice. The number of pulmonary effector T cells was still increased in *Ch25h*$^{-/-}$ mice **(Figure 14A)**. Intact Mtb-specific T cell responses were also maintained, represented by the induction of multifunctional (IFN-γ^{+}TNF-α^{+}, IFN-γ^{+}IL-2^{+}, IFN-γ^{+}TNF-α^{+}IL-2^{+}) pulmonary $CD4^{+}$ T cells **(Figure 14B)** and increased numbers of IFN-γ, TNF-α, and IL-2-positive $CD4^{+}$ T cells **(Figure 14C)**. The increase in IFN-γ, TNF-α, and IL-2 production and the decrease in IL-10 production were also observed **(Figure 14D)**. Taken together, we concluded that the induction of Mtb-specific pulmonary T cells mediated by CH25H deficiency contributes to enhanced protection against Mtb *in vivo*.

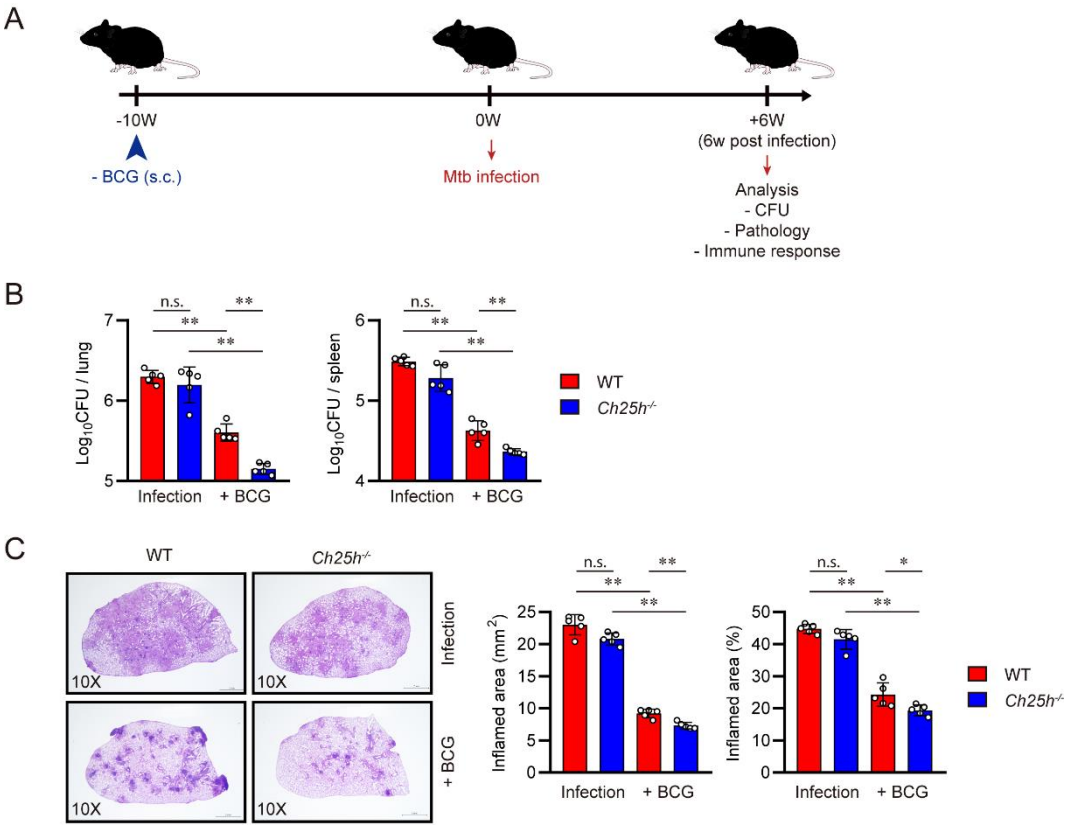

Figure 13. Status of TB progression in WT and *Ch25h*$^{-/-}$ mice, represented by lung inflammation and mycobacterial load at six weeks post-infection. (A) Experimental scheme for *in vivo* Mtb challenge in BCG-vaccinated mice. **(B)** CFUs of lungs and spleen and **(C)** lung pathology of Mtb-infected WT and *Ch25h*$^{-/-}$ mice. H&E staining was performed on the superior lobes of the right lung at six weeks post-infection to visualize the gross lung pathology. The data are presented as the mean ± SD of five mice in each group. The significance of differences was determined, using the ANOVA test and Mann-Whitney U test. *n.s.*, not significant. *p <0.05, **p <0.01

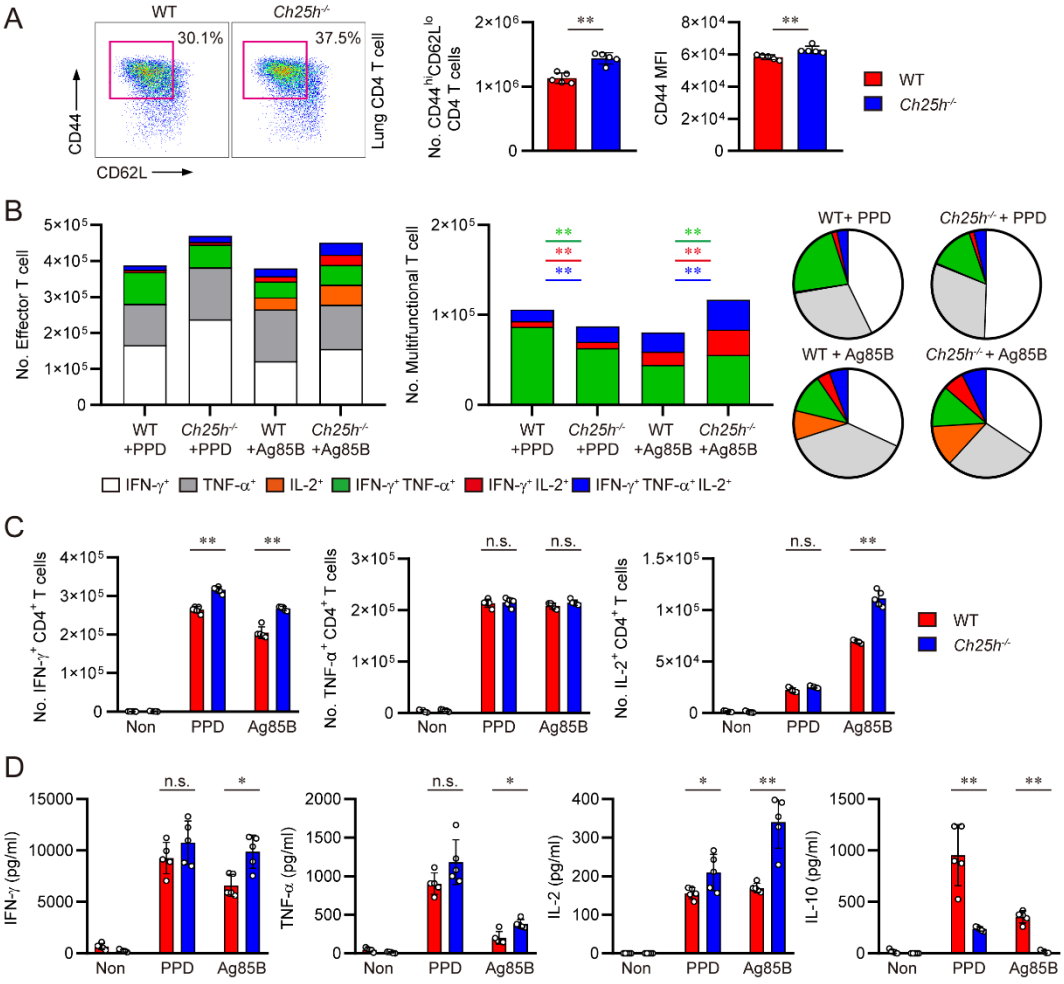

Figure 14. Immunological profiles of pulmonary CD4$^+$ T cells in BCG-vaccinated WT and *Ch25h*$^{-/-}$ mice analysed at six weeks post-infection. (A) Flow cytometry analysis of pulmonary effector CD4$^+$ T cells. **(B)** The frequencies of Mtb-specific pulmonary multifunctional T cells, represented as the percent of each cytokine positive T cell among the total cytokine positive T cells. Green bars indicate the statistical significance between IFN-γ$^+$ TNF-α$^+$ CD4$^+$ T cells, red bars indicate the statistical significance between IFN-γ$^+$ IL-2$^+$ CD4$^+$ T cells, and blue bars indicate the statistical significance between IFN-γ$^+$ TNF-α$^+$ IL-2$^+$ CD4$^+$ T cells. **(C)** The numbers of Mtb-specific IFN-γ$^+$, TNF-α$^+$, and IL-2$^+$ CD4$^+$ T cells. **(D)** The levels of IFN-γ, TNF-α, IL-2, IL-17A, and IL-10 in the supernatant of antigen stimulated Mtb-infected lung cells in WT and *Ch25h*$^{-/-}$ mice. The data are presented as the mean ± SD of five mice in each group. The significance of differences was determined, using the Mann-Whitney U test. *n.s.*, not significant. **p* <0.05, ***p* <0.01

3.6. CH25H deficiency contributes to the long-term maintenance of BCG-induced Mtb-specific Th1 cells for up to twelve weeks post-infection

To ascertain whether the improved protection against Mtb in BCG-vaccinated *Ch25h*$^{-/-}$ mice can be sustained beyond six weeks post-infection, we planned to evaluate the impact of CH25H deficiency on TB progression in *Ch25h*$^{-/-}$ mice at a later time point. Given that the efficacy of BCG vaccination is reported to diminish after 60 days in WT mice[226,227], we planned to conduct analysis at a time point beyond this threshold. At twelve weeks post-infection, the mice were euthanized to assess the severity of TB and immune functions **(Figure 15A)**. Interestingly, while BCG-vaccinated WT mice did not show a significant reduction in pulmonary CFUs in comparison to unvaccinated WT mice, BCG vaccinated *Ch25h*$^{-/-}$ mice showed a clear reduction in CFUs **(Figure 15B)** and lung inflammation **(Figure 15C)** at ten weeks post-infection. Furthermore, we could observe sustainment of intact Th1 responses against Mtb. Although the number of pulmonary effector T cells was not significantly altered **(Figure 16A)**, multifunctional (IFN-γ^+ TNF-α^+, IFN-γ^+IL-2^+, IFN-γ^+TNF-α^+IL-2^+) pulmonary $CD4^+$ T cells **(Figure 16B)** and IFN-γ, TNF-α, and IL-2-positive $CD4^+$ T cells **(Figure 16C)** were strongly induced in the lungs of BCG-vaccinated *Ch25h*$^{-/-}$ mice. In addition, although the expression of IFN-γ and TNF-α were not significantly altered in BCG-vaccinated *Ch25h*$^{-/-}$ mice, the expression of IL-2 was significantly sustained, along with the reduction of IL-10 expression **(Figure 16D)**. Taken together, we found that CH25H deficiency is potent at maintaining the efficacies of BCG-induced Mtb-specific immune memory *in vivo*. Our data suggest a novel immunologic mechanism initiated by CH25H deficiency, which enables optimal activation of DCs stimulated with mycobacterial antigens. We also revealed that CH25H deficiency in DCs, not T cells is the key factor for enhancing proliferation and Th1 polarization of T cells. Although CH25H deficiency does not directly alter anti-TB immune responses at four weeks post-infection, we found that BCG vaccination can induce rapidly proliferating and highly reactive Th1 cells in the lungs of

Ch25h$^{-/-}$ mice. These Th1 cells and their robust responses were sustained until twelve weeks post-infection, correlating with the enhanced efficacy of BCG vaccination *in vivo*. Collectively, our findings suggest that an intensified protective connection between DC and CD4^{+} T cell axis is the crucial immunological factor contributing to the long-term maintenance of anti-TB immunity in BCG-vaccinated *Ch25h*$^{-/-}$ mice **(Figure 17)**.

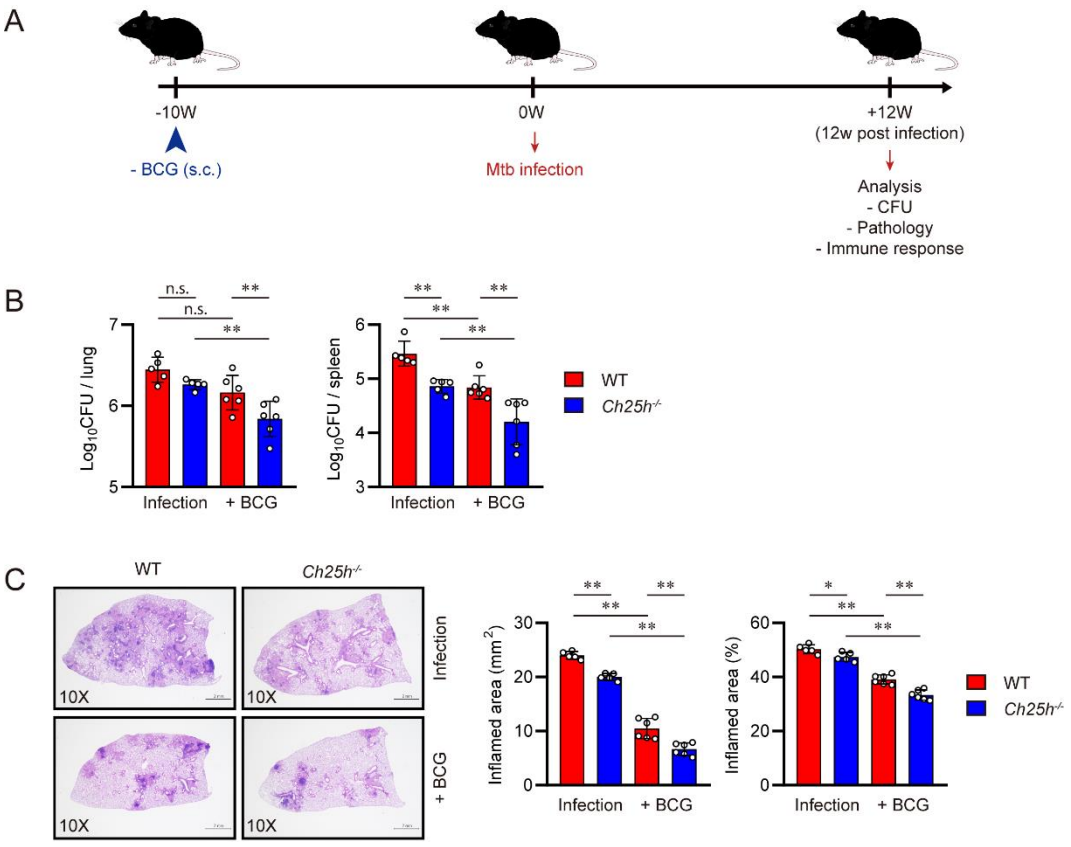

Figure 15. Status of TB progression in WT and *Ch25h*$^{-/-}$ mice, represented by lung inflammation and mycobacterial load at twelve weeks post-infection. (A) Experimental scheme for *in vivo* Mtb challenge in BCG-vaccinated mice. **(B)** CFUs of lungs and spleen and **(C)** lung pathology of Mtb-infected WT and *Ch25h*$^{-/-}$ mice. H&E staining was performed on the superior lobes of the right lung at ten weeks post-infection to visualize the gross lung pathology. The data are presented as the mean ± SD of six mice in each group. The significance of differences was determined, using the ANOVA test and Mann-Whitney U test. *n.s.*, not significant. *p <0.05. **p <0.01

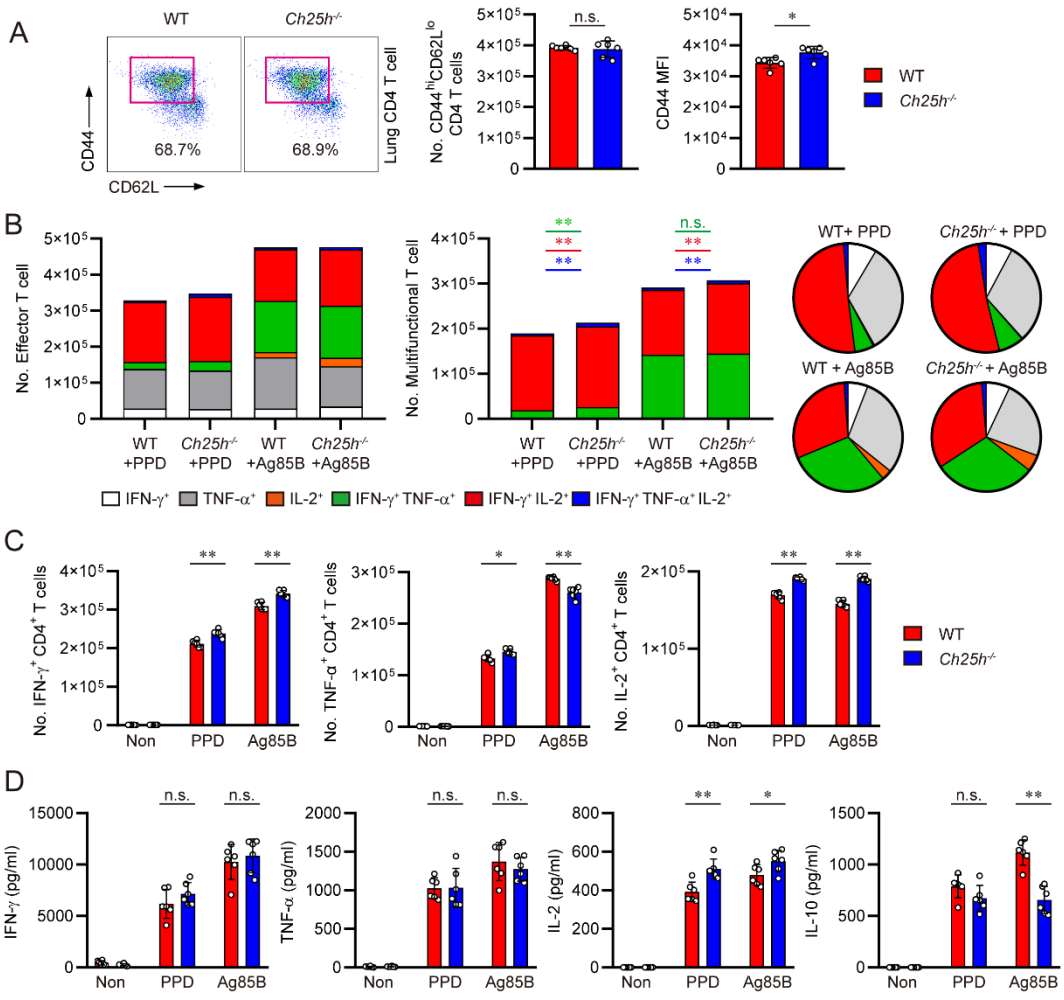

Figure 16. Immunological profiles of pulmonary CD4$^+$ T cells in BCG-vaccinated WT and *Ch25h*$^{-/-}$ mice analysed at twelve weeks post-infection. **(A)** Experimental scheme for *in vivo* Mtb challenge in BCG-vaccinated mice. **(B)** CFUs of lungs and spleen and **(C)** lung pathology of Mtb-infected WT and *Ch25h*$^{-/-}$ mice. H&E staining was performed on the superior lobes of the right lung at ten weeks post-infection to visualize the gross lung pathology. **(D)** Flow cytometry analysis of pulmonary effector CD4$^+$ T cells. **(E)** The frequencies of Mtb-specific pulmonary multifunctional T cells, represented as the percent of each cytokine positive T cell among the total cytokine positive T cells. Green bars indicate the statistical significance between IFN-γ$^+$ TNF-α$^+$ CD4$^+$ T cells, red bars indicate the statistical significance between IFN-γ$^+$ IL-2$^+$ CD4$^+$ T cells, and blue bars indicate the statistical significance between IFN-γ$^+$ TNF-α$^+$ IL-2$^+$ CD4$^+$ T cells. **(F)** The numbers of Mtb-specific IFN-γ$^+$, TNF-α$^+$, and IL-2$^+$ CD4$^+$ T cells. **(G)** The levels of IFN-γ, TNF-α, IL-2, IL-17A, and IL-10 in the supernatant of antigen stimulated Mtb-infected lung cells in WT and *Ch25h*$^{-/-}$ mice. The data are presented as the mean ± SD of six mice in each group. The significance of differences was determined, using the Mann-Whitney U test. *n.s.*, not significant. **p* <0.05. ***p* <0.01

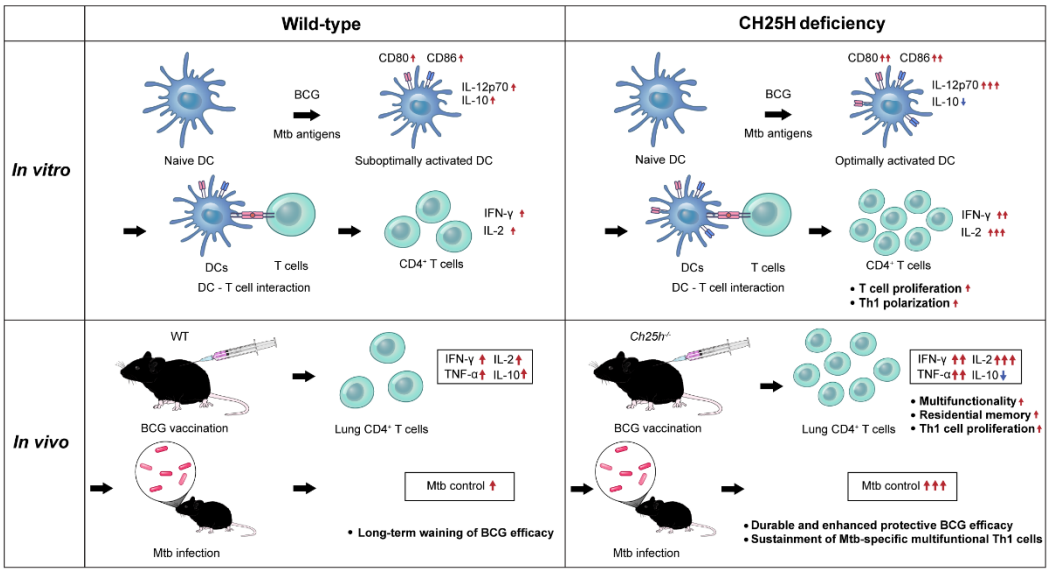

Figure 17. A graphical abstract with influence of CH25H deficiency on altering anti-TB immune responses with emphasis on the interaction between DCs and T cells. *Ch25h*$^{-/-}$ DCs exhibited heightened capacity to stimulate T cell proliferation and activation, characterized by elevated expression levels of CD80 and CD86, as well as augmented production of IL-12p70 and reduced secretion of IL-10. Notably, *Ch25h*$^{-/-}$ DCs demonstrated proficiency in eliciting T cell-mediated immune responses against Mtb. Despite the lack of apparent resistance to TB in *Ch25h*$^{-/-}$ mice, the induction of Mtb-specific Th1 responses in BCG-vaccinated *Ch25h*$^{-/-}$ mice. Taken together, the establishment and persistence of such immune memory facilitated enhanced resistance against Mtb infection in BCG-vaccinated *Ch25h*$^{-/-}$ mice.

4. DISCUSSION

BCG, the only licensed vaccine against TB, is suboptimal due to its waning protection over time. As BCG loses its effectiveness after adolescence[228], developing a new vaccine against TB requires the ability to trigger and sustain a strong, long-term Mtb-specific immune response. Proper immunological priming is crucial for generating durable Th1 protective responses against Mtb infection through vaccination. While CH25H-deficient macrophages exhibit heightened inflammatory reactions[186,189], the role of CH25H in DCs, which are key innate cells bridging T cell polarization, has not been fully elucidated particularly in the context of vaccine-mediated T cell immunity against intracellular bacterial infections including TB.

In this study, we, to the best of our knowledge, for the first time investigated the impacts of CH25H deficiency on anti-TB immunity, with a focus on DC-T cell axis. First, we observed that *Ch25h*$^{-/-}$ DCs can induce T cell proliferation and activation through high expression of CD80 and CD86, along with marked increased IL-12p70 production and decreased IL-10 production. Secondly, we demonstrated that CH25H deficiency in DCs, rather than in T cells, can trigger rapid T cell proliferation and Th1 cytokine production *in vitro*. Third, we found that highly proliferative Mtb-specific multifunctional T cells were induced in BCG-vaccinated *Ch25h*$^{-/-}$ mice. Lastly, our findings demonstrated that these multifunctional T cells were sustained in the lungs of BCG-vaccinated *Ch25h*$^{-/-}$ mice up to twelve weeks post-infection, correlating with enhanced protection against Mtb. Collectively, our study suggests that CH25H deficiency contributes to the long-term maintenance of Mtb-specific immune responses by activating the DC-CD4^{+} Th1 cell axis. Our research firstly examined the impact of CH25H on vaccine efficacy, revealing detailed mechanisms by which it enhances and sustains strong immune memory against antigens. Notably, we demonstrated that CH25H deficiency is essential not only for inducing robust immune memory but also for maintaining

long-term antigen-specific responses. Such novel findings may provide valuable insights for a broad range of vaccine-related studies targeting multiple pathogens, extending beyond TB vaccines.

Our study is the first investigation into the protective effects of CH25H deficiency on immune responses against Mtb. Although Bohrer et al. explored the impact of CH25H on anti-TB immunity, their research primarily focused on the roles of CH25H and the oxysterol receptor GPR183 in eosinophil recruitment. They suggested that eosinophils in *Ch25h*$^{-/-}$ mice exhibit impaired recruitment to tissues due to the inability of alveolar macrophages to produce 25-HC[229]. Zhou et al. highlighted the role of 25-HC in *Mycobacterium marinum* infection by showing that *Ch25h*$^{-/-}$ mice display reduced formation of foam cells and less severe lung pathology[196]. However, these studies did not elucidate the precise mechanisms by which CH25H regulates protective immune responses against mycobacterial infections. They neither focused on the involvement of CH25H in modulating adaptive immune responses against Mtb nor utilized vaccination-related *in vivo* models. Building on previous studies that primarily addressed innate immune responses, we delved into the regulatory roles of CH25H, which impedes the induction of pathogen-specific immune memory by impairing the optimal activation of DC-T cell axis. Additionally, we proposed specific immune mechanisms explaining how CH25H deficiency supports the maintenance of intact Mtb-specific Th1 responses, which are crucial immunological factors in defense against Mtb[117,204], both *in vivo* and *in vitro*. Our study broadened insights into the impacts of CH25H, extending from its role in innate cells to its further influence on adaptive immune responses against Mtb.

Furthermore, our findings contribute additional novelty by demonstrating that CH25H deficiency significantly upregulates IL-12p70 production in DCs challenged with mycobacterial antigens. Although IL-12p70 is a crucial immunological factor for mediating Th1 differentiation, its induction *in vivo* is reported to be challenging in various vaccine models[230-232]. As we highlighted that CH25H deficiency alters IL-12p70 expression in DCs, our research could serve as a starting point for

identifying factors that contribute to the upregulation of IL-12p70 in immune cells. Moreover, our study may also provide insights for developing IL-12p70-related therapeutic interventions for various diseases beyond TB, including RNA cancer vaccines, which require robust induction of IL-12p70 to enhance their efficacy[233,234].

Building on previous studies related to CH25H, we focused on its role in modulating cytokine production and the expression of co-stimulatory markers in DCs. The role of CH25H in altering inflammatory responses is well established, with most research focusing on its impact on macrophages[186,189]. Although Lu et al. assessed the role of CH25H in altering DC functions, they primarily focused on the impaired cross-presentation of tumor antigens in *Ch25h*$^{-/-}$ DCs. This deficiency in antigen cross-presentation within the tumor microenvironment ultimately contributed to lung cancer progression in *Ch25h*$^{-/-}$ DCs[168]. In contrast, our findings revealed that CH25H deficiency induces the expression of CD80 and CD86, as well as the upregulation of IL-12p70 and downregulation of IL-10. We suggest a novel avenue for research into the roles of CH25H in innate immune cells, highlighting its impact on the functional properties of DCs.

Our observations are particularly noteworthy as we revealed that CH25H deficiency in DCs, rather than in T cells, is crucial for the establishment of intact Mtb-specific Th1 responses. While CH25H primarily suppresses inflammatory responses in innate cells[185,189], it has been reported to promote T cell-mediated inflammation in various models of neuroinflammation[192,193]. Although prior studies suggest that CH25H deficiency in T cells may suppress the expression of inflammatory cytokines, we found that *Ch25h*$^{-/-}$ T cells do not exhibit altered Th1 cytokine production or proliferation in response to stimulated DCs. We emphasize that CH25H deficiency in T cells is not a critical factor in modulating immune responses against Mtb or BCG. Furthermore, we highlight that DCs are the specific cell type affected by CH25H deficiency and are responsible for providing enhanced protection against Mtb.

While the induction of Th1 response is crucial for defense against Mtb at four weeks post-infection, it remains unclear why *Ch25h*$^{-/-}$ mice did not feature enhanced protection at this time point. We hypothesize that this phenomenon may arise from the altered responses of *Ch25h*$^{-/-}$ DCs to Mtb and BCG, which are distinct pathogens with different virulence profiles. According to Kim et al., highly virulent Mtb strains stimulate DCs to produce more IL-10, leading to impaired Th1 polarization and decreased T cell proliferation[235]. We propose that exposure to Mtb may lead to increased IL-10 production and decreased IL-12p70 production in *Ch25h*$^{-/-}$ DCs, potentially compromising their protective efficacy *in vivo*. Conversely, when challenged with BCG, *Ch25h*$^{-/-}$ DCs may successfully induce Th1 polarization, facilitated by decreased IL-10 production and increased IL-12p70 production. This suggests that CH25H deficiency in innate cells may yield different outcomes depending on the type of pathogens encountered, in a manner that is influenced by virulence. We hypothesize that the distinct immune responses of *Ch25h*$^{-/-}$ DCs to Mtb and BCG confer protective immunity specifically in BCG-vaccinated *Ch25h*$^{-/-}$ mice.

We confirmed that BCG vaccination induces rapidly proliferating and less exhausted effector T cells in the lungs of *Ch25h*$^{-/-}$ mice. This is likely attributed to IL-2, which is a key factor in promoting T cell proliferation and preventing T cell exhaustion[236,237]. Meanwhile, it is uncertain which immunological factors strongly upregulate IL-2 in T cells, aside from DC activation. We hypothesize that the autocrine expression of IL-2 in Th1 cells may be critical for its distinct upregulation, given the autocrine nature of IL-2 in enhancing its own expression within T cells[238,239]. This autocrine IL-2 is also considered essential for the long-term sustainment of Mtb-specific Th1 cells, as IL-2-positive T cells were abundant in the lungs of BCG-vaccinated *Ch25h*$^{-/-}$ mice up to twelve weeks post-infection, a time point at which DCs stimulated with BCG may be diminished. Pro-inflammatory signatures of *Ch25h*$^{-/-}$ innate cells are considered another factor that can promote

IL-2 production in T cells, as inflammatory cytokines such as IL-1, IL-15, and TNF-α are crucial for upregulating IL-2 expression in T cells[240].

While CH25H deficiency modulates humoral immune responses, these factors are not as critical as the DC-T cell axis in anti-TB immunity. Although inflammatory lymphocyte accumulation, plasma cell differentiation, and antibody production are described as key features of *Ch25h*$^{-/-}$ mice in colitis models[207,241,242], we did not observe a strong induction of antigen-specific IgG responses in our TB models. We concluded that while CH25H may influence humoral immune responses, its contribution to anti-TB immunity appears to be less critical than the DC-mediated Th1 responses in our model of Mtb infection.

Our study underscores the need for further research and the development of innovative approaches, such as designing new adjuvant candidates which restrict CH25H expression or 25-HC activation. Given that various adjuvants used in TB vaccines aim to enhance Mtb-specific Th1 responses[243,244], molecules that can downregulate 25-HC production or CH25H expression may have the potential to enhance the efficacy of TB vaccines. While similar approaches have not yet been applied in TB vaccine research, studies have already suggested the potential of cholesterol-modulating drugs to enhance the efficacy of cancer vaccines. For instance, the combination of a Kras peptide cancer vaccine with avasimibe, a drug that modifies cholesterol levels in T cells, resulted in an increased number of antigen-specific IFN-γ positive $CD8^+$ T cells successfully preventing lung tumor progression in mice [67]. These challenges further emphasize the value of our research, suggesting that modulators of CH25H or 25-HC could serve as potential adjuvants, particularly in vaccines that require enhanced Th1 responses. We anticipate that our study will provide valuable insights for the development of novel adjuvants for TB vaccines.

Furthermore, we hypothesize that the *Ch25h*$^{-/-}$ mouse model may be well-suited for adapting various forms of TB vaccines, including mucosal immunization, subunit vaccination, or adjuvants

that enhance DC functions. Considering that additional impacts of CH25H deficiency on adaptive immune responses, such as increased IgA production at mucosal sites[207] have the potential to alter vaccine efficacy[245,246], we believe that utilizing *Ch25h*$^{-/-}$ mouse model in various TB vaccine-related studies will be beneficial for broadening understandings on vaccine related immune responses.

However, we acknowledge several limitations in our study that require discussion. Firstly, although we uncovered the impact of CH25H on modulating functional properties of DCs after antigen stimulation, the detailed mechanisms by which CH25H influences the expression of co-stimulatory molecules and cytokines remain unclear. Secondly, we did not precisely investigate whether the 25-HC derived from CH25H plays a crucial role in suppressing immune responses against Mtb or whether exogenous 25-HC can modulate DC functions. Lastly, it remains unclear whether CH25H deficiency enhances the efficacy only of subcutaneous BCG vaccination or if it can also improve the efficacy of other vaccination forms and routes of administration.

Despite the limitations, our study is novel as it is the first to propose that CH25H deficiency can alter anti-TB immune responses both *in vivo* and *in vitro*. We also firstly proposed that DC-CD4^{+} T cell axis, reinforced by CH25H deficiency, is responsible for the long-term preservation of BCG efficacy. Furthermore, our research is the first to reveal that host factors can potentially suppress BCG efficacy. Conventional approaches to TB vaccines have primarily focused on developing new vaccine candidates or adjuvants that intensify immune responses against Mtb. However, our study introduces a novel approach by targeting a detrimental host factor that interferes with the induction of optimal anti-TB immunity. By identifying CH25H as a host factor capable of suppressing proper immune responses against Mtb, we propose that modulating such host factors can serve as a novel strategy to enhance vaccine efficacy. Our findings may also encourage further researches to identify additional detrimental host factors that hinder the optimal activation of pathogen-specific immune memory induced by vaccination.

5. CONCLUSION

Our research offers new insights into the role of CH25H in regulating immune memory against Mtb. By analyzing the properties of *Ch25h*$^{-/-}$ DCs, we discovered that CH25H deficiency enables the optimal activation of stimulated DCs, leading to enhanced T cell proliferation and Th1 cytokine production. Our findings indicate that while CH25H deficiency does not significantly impact TB pathogenesis, it contributes to the induction of BCG-mediated immune memory. We demonstrated that BCG vaccination induces highly reactive Mtb-specific Th1 cells, which provide long-term resistance against Mtb infection in *Ch25h*$^{-/-}$ mice, lasting up to twelve weeks post-infection. Our results provide a critical foundation for further understanding anti-TB immunity and developing innovative strategies for protective interventions against Mtb.

References

1. Zhang Y, Murugesan P, Huang K, Cai H. NADPH oxidases and oxidase crosstalk in cardiovascular diseases: novel therapeutic targets. Nat Rev Cardiol 2020;17:170-94.
2. Peng JJ, Liu B, Xu JY, Peng J, Luo XJ. NADPH oxidase: its potential role in promotion of pulmonary arterial hypertension. Naunyn Schmiedebergs Arch Pharmacol 2017;390:331-8.
3. Olive AJ, Smith CM, Kiritsy MC, Sassetti CM. The Phagocyte Oxidase Controls Tolerance to Mycobacterium tuberculosis Infection. J Immunol 2018;201:1705-16.
4. Miller JL, Velmurugan K, Cowan MJ, Briken V. The type I NADH dehydrogenase of Mycobacterium tuberculosis counters phagosomal NOX2 activity to inhibit TNF-alpha-mediated host cell apoptosis. PLoS Pathog 2010;6:e1000864.
5. Brandes RP, Weissmann N, Schröder K. Nox family NADPH oxidases: Molecular mechanisms of activation. Free Radic Biol Med 2014;76:208-26.
6. Panday A, Sahoo MK, Osorio D, Batra S. NADPH oxidases: an overview from structure to innate immunity-associated pathologies. Cell Mol Immunol 2015;12:5-23.
7. Sies H, Jones DP. Reactive oxygen species (ROS) as pleiotropic physiological signalling agents. Nat Rev Mol Cell Biol 2020;21:363-83.
8. Xiao X, Bu H, Li Z, Li Z, Bai Q, Wang Z, et al. NADPH-Oxidase 2 Promotes Autophagy in Spinal Neurons During the Development of Morphine Tolerance. Neurochem Res 2021;46:2089-96.
9. Munnamalai V, Weaver CJ, Weisheit CE, Venkatraman P, Agim ZS, Quinn MT, et al. Bidirectional interactions between NOX2-type NADPH oxidase and the F-actin

cytoskeleton in neuronal growth cones. J Neurochem 2014;130:526-40.

10. Anjani G, Vignesh P, Joshi V, Shandilya JK, Bhattarai D, Sharma J, et al. Recent advances in chronic granulomatous disease. Genes Dis 2020;7:84-92.
11. Xu Q, Wang Q, Hu LT, Lin J, Jiang N, Peng XD, et al. NADPH oxidase 2 plays a protective role in experimental Aspergillus fumigatus keratitis in mice through killing fungi and limiting the degree of inflammation. Int J Ophthalmol 2022;15:1044-52.
12. Taylor JP, Tse HM. The role of NADPH oxidases in infectious and inflammatory diseases. Redox Biol 2021;48:102159.
13. Rojas Márquez JD, Li T, McCluggage ARR, Tan JMJ, Muise A, Higgins DE, et al. Cutting Edge: NOX2 NADPH Oxidase Controls Infection by an Intracellular Bacterial Pathogen through Limiting the Type 1 IFN Response. J Immunol 2021;206:323-8.
14. Kohn DB, Booth C, Kang EM, Pai SY, Shaw KL, Santilli G, et al. Lentiviral gene therapy for X-linked chronic granulomatous disease. Nat Med 2020;26:200-6.
15. Bustamante J, Arias AA, Vogt G, Picard C, Galicia LB, Prando C, et al. Germline CYBB mutations that selectively affect macrophages in kindreds with X-linked predisposition to tuberculous mycobacterial disease. Nat Immunol 2011;12:213-21.
16. Conti F, Lugo-Reyes SO, Blancas Galicia L, He J, Aksu G, Borges de Oliveira E, Jr., et al. Mycobacterial disease in patients with chronic granulomatous disease: A retrospective analysis of 71 cases. J Allergy Clin Immunol 2016;138:241-8.e3.
17. Segal AW. How neutrophils kill microbes. Annu Rev Immunol 2005;23:197-223.
18. Lv J, He X, Wang H, Wang Z, Kelly GT, Wang X, et al. TLR4-NOX2 axis regulates the phagocytosis and killing of Mycobacterium tuberculosis by macrophages. BMC Pulm Med 2017;17:194.
19. Nguyen GT, Green ER, Mecsas J. Neutrophils to the ROScue: Mechanisms of NADPH

Oxidase Activation and Bacterial Resistance. Front Cell Infect Microbiol 2017;7:373.

20. Roos D, van Bruggen R, Meischl C. Oxidative killing of microbes by neutrophils. Microbes Infect 2003;5:1307-15.

21. Segal BH, Grimm MJ, Khan AN, Han W, Blackwell TS. Regulation of innate immunity by NADPH oxidase. Free Radic Biol Med 2012;53:72-80.

22. Winkelstein JA, Marino MC, Johnston RB, Jr., Boyle J, Curnutte J, Gallin JI, et al. Chronic granulomatous disease. Report on a national registry of 368 patients. Medicine (Baltimore) 2000;79:155-69.

23. Matute JD, Arias AA, Wright NA, Wrobel I, Waterhouse CC, Li XJ, et al. A new genetic subgroup of chronic granulomatous disease with autosomal recessive mutations in p40 phox and selective defects in neutrophil NADPH oxidase activity. Blood 2009;114:3309-15.

24. Hajjar J, Restrepo A, Javeri H, Wiederhold NP, Papanastassiou AM, Patterson TF. Multiple Brain Abscesses Caused by Trichosporon inkin in a Patient with X-Linked Chronic Granulomatous Disease (CGD) Successfully Treated with Antifungal Therapy. J Clin Immunol 2017;37:519-23.

25. Falcone EL, Holland SM. Invasive fungal infection in chronic granulomatous disease: insights into pathogenesis and management. Curr Opin Infect Dis 2012;25:658-69.

26. Bassiri-Jahromi S, Doostkam A. Fungal infection and increased mortality in patients with chronic granulomatous disease. J Mycol Med 2012;22:52-7.

27. Buvelot H, Posfay-Barbe KM, Linder P, Schrenzel J, Krause KH. Staphylococcus aureus, phagocyte NADPH oxidase and chronic granulomatous disease. FEMS Microbiol Rev 2017;41:139-57.

28. Dotis J, Roilides E. Osteomyelitis due to Aspergillus species in chronic granulomatous

disease: an update of the literature. Mycoses 2011;54:e686-96.

29. Speert DP, Bond M, Woodman RC, Curnutte JT. Infection with Pseudomonas cepacia in chronic granulomatous disease: role of nonoxidative killing by neutrophils in host defense. J Infect Dis 1994;170:1524-31.

30. Porter LA, Goldberg JB. Influence of neutrophil defects on Burkholderia cepacia complex pathogenesis. Front Cell Infect Microbiol 2011;1:9.

31. King J, Henriet SSV, Warris A. Aspergillosis in Chronic Granulomatous Disease. J Fungi (Basel) 2016;2.

32. Camanni G, Sgrelli A, Ferraro L. Aspergillus myofasciitis in a chronic granulomatous disease patient: first case report. Infez Med 2017;25:270-3.

33. Van Woensel J, Leers MP, Mostard RL. Invasive Pulmonary Aspergillosis with Marked Eosinophilia as a Unique Presentation of Chronic Granulomatous Disease. Eur J Case Rep Intern Med 2022;9:003423.

34. Skrzypek MS, Binkley J, Binkley G, Miyasato SR, Simison M, Sherlock G. The Candida Genome Database (CGD): incorporation of Assembly 22, systematic identifiers and visualization of high throughput sequencing data. Nucleic Acids Res 2017;45:D592-d6.

35. Aratani Y. [Role of myeloperoxidase in the host defense against fungal infection]. Nihon Ishinkin Gakkai Zasshi 2006;47:195-9.

36. Jabado N, Casanova JL, Haddad E, Dulieu F, Fournet JC, Dupont B, et al. Invasive pulmonary infection due to Scedosporium apiospermum in two children with chronic granulomatous disease. Clin Infect Dis 1998;27:1437-41.

37. Dotis J, Pana ZD, Roilides E. Non-Aspergillus fungal infections in chronic granulomatous disease. Mycoses 2013;56:449-62.

38. García B, León-Lara X, Espinosa S, Blancas-Galicia L. [Mycobacterial disease in patients

with chronic granulomatous disease]. Rev Alerg Mex 2021;68:117-27.

39. Ohga S, Ikeuchi K, Kadoya R, Okada K, Miyazaki C, Suita S, et al. Intrapulmonary Mycobacterium avium infection as the first manifestation of chronic granulomatous disease. J Infect 1997;34:147-50.

40. Deffert C, Schäppi MG, Pache JC, Cachat J, Vesin D, Bisig R, et al. Bacillus calmette-guerin infection in NADPH oxidase deficiency: defective mycobacterial sequestration and granuloma formation. PLoS Pathog 2014;10:e1004325.

41. Ying W, Sun J, Liu D, Hui X, Yu Y, Wang J, et al. Clinical characteristics and immunogenetics of BCGosis/BCGitis in Chinese children: a 6 year follow-up study. PLoS One 2014;9:e94485.

42. Soyak Aytekin E, Keskin A, Tan C, Yalçın E, Dogru D, Ozcelik U, et al. Differential diagnosis of primary immunodeficiency in patients with BCGitis and BCGosis: A single-centre study. Scand J Immunol 2021;94:e13084.

43. Thomas SM, Olive AJ. High Lethality of Mycobacterium tuberculosis Infection in Mice Lacking the Phagocyte Oxidase and Caspase1/11. Infect Immun 2023; doi:10.1128/iai.00060-23.e0006023.

44. Chao WC, Yen CL, Hsieh CY, Huang YF, Tseng YL, Nigrovic PA, et al. Mycobacterial infection induces higher interleukin-1β and dysregulated lung inflammation in mice with defective leukocyte NADPH oxidase. PLoS One 2017;12:e0189453.

45. Heyworth PG, Cross AR, Curnutte JT. Chronic granulomatous disease. Curr Opin Immunol 2003;15:578-84.

46. Segal BH, Han W, Bushey JJ, Joo M, Bhatti Z, Feminella J, et al. NADPH oxidase limits innate immune responses in the lungs in mice. PLoS One 2010;5:e9631.

47. Singel KL, Segal BH. NOX2-dependent regulation of inflammation. Clin Sci (Lond)

2016;130:479-90.

48. Liao YC, Wu SY, Huang YF, Lo PC, Chan TY, Chen CA, et al. NOX2-Deficient Neutrophils Facilitate Joint Inflammation Through Higher Pro-Inflammatory and Weakened Immune Checkpoint Activities. Front Immunol 2021;12:743030.

49. Wang J, Ma MW, Dhandapani KM, Brann DW. Regulatory role of NADPH oxidase 2 in the polarization dynamics and neurotoxicity of microglia/macrophages after traumatic brain injury. Free Radic Biol Med 2017;113:119-31.

50. Bagaitkar J, Pech NK, Ivanov S, Austin A, Zeng MY, Pallat S, et al. NADPH oxidase controls neutrophilic response to sterile inflammation in mice by regulating the IL-1α/G-CSF axis. Blood 2015;126:2724-33.

51. Song Z, Bhattacharya S, Huang G, Greenberg ZJ, Yang W, Bagaitkar J, et al. NADPH oxidase 2 limits amplification of IL-1β-G-CSF axis and an immature neutrophil subset in murine lung inflammation. Blood Adv 2023;7:1225-40.

52. Keller CW, Kotur MB, Mundt S, Dokalis N, Ligeon LA, Shah AM, et al. CYBB/NOX2 in conventional DCs controls T cell encephalitogenicity during neuroinflammation. Autophagy 2021;17:1244-58.

53. Nauseef WM. Biological roles for the NOX family NADPH oxidases. J Biol Chem 2008;283:16961-5.

54. Zeng MY, Miralda I, Armstrong CL, Uriarte SM, Bagaitkar J. The roles of NADPH oxidase in modulating neutrophil effector responses. Mol Oral Microbiol 2019;34:27-38.

55. Trevelin SC, Shah AM, Lombardi G. Beyond bacterial killing: NADPH oxidase 2 is an immunomodulator. Immunol Lett 2020;221:39-48.

56. Baruah S, Murthy S, Keck K, Galvan I, Prichard A, Allen LH, et al. TREM-1 regulates neutrophil chemotaxis by promoting NOX-dependent superoxide production. J Leukoc

Biol 2019;105:1195-207.

57. Carneiro MBH, Roma EH, Ranson AJ, Doria NA, Debrabant A, Sacks DL, et al. NOX2-Derived Reactive Oxygen Species Control Inflammation during Leishmania amazonensis Infection by Mediating Infection-Induced Neutrophil Apoptosis. J Immunol 2018;200:196-208.

58. Ranson AJ, Carneiro MB, Perks B, Penner R, Melo L, Canton J, et al. C3/CD11b-Mediated Leishmania major Internalization by Neutrophils Induces Intraphagosomal NOX2-Mediated Respiratory Burst but Fails to Eliminate Parasites and Induces a State of Stalled Apoptosis. J Immunol 2023;211:103-17.

59. Li J, Cho J. Ser/Thr protein kinase Bβ-NADPH oxidase 2 signaling in thromboinflammation. Curr Opin Hematol 2017;24:460-6.

60. Yan JB, Nie YM, Xu SM, Zhang S, Chen ZY. Pure total flavonoids from citrus alleviate oxidative stress and inflammation in nonalcoholic fatty liver disease by regulating the miR-137-3p/NOXA2/NOX2 pathway. Phytomedicine 2023;118:154944.

61. Pintard C, Ben Khemis M, Liu D, Dang PM, Hurtado-Nedelec M, El-Benna J. Apocynin prevents GM-CSF-induced-ERK1/2 activation and -neutrophil survival independently of its inhibitory effect on the phagocyte NADPH oxidase NOX2. Biochem Pharmacol 2020;177:113950.

62. Nadesalingam A, Chen JHK, Farahvash A, Khan MA. Hypertonic Saline Suppresses NADPH Oxidase-Dependent Neutrophil Extracellular Trap Formation and Promotes Apoptosis. Front Immunol 2018;9:359.

63. Hook JS, Cao M, Potera RM, Alsmadi NZ, Schmidtke DW, Moreland JG. Nox2 Regulates Platelet Activation and NET Formation in the Lung. Front Immunol 2019;10:1472.

64. Hook JS, Patel PA, O'Malley A, Xie L, Kavanaugh JS, Horswill AR, et al. Lipoproteins

from Staphylococcus aureus Drive Neutrophil Extracellular Trap Formation in a TLR2/1- and PAD-Dependent Manner. J Immunol 2021;207:966-73.

65. Yu HH, Yang YH, Chiang BL. Chronic Granulomatous Disease: a Comprehensive Review. Clin Rev Allergy Immunol 2021;61:101-13.

66. Barrett JP, Henry RJ, Villapol S, Stoica BA, Kumar A, Burns MP, et al. NOX2 deficiency alters macrophage phenotype through an IL-10/STAT3 dependent mechanism: implications for traumatic brain injury. J Neuroinflammation 2017;14:65.

67. Hegdekar N, Sarkar C, Bustos S, Ritzel RM, Hanscom M, Ravishankar P, et al. Inhibition of autophagy in microglia and macrophages exacerbates innate immune responses and worsens brain injury outcomes. Autophagy 2023;19:2026-44.

68. Idol RA, Bhattacharya S, Huang G, Song Z, Huttenlocher A, Keller NP, et al. Neutrophil and Macrophage NADPH Oxidase 2 Differentially Control Responses to Inflammation and to Aspergillus fumigatus in Mice. J Immunol 2022;209:1960-72.

69. Goebel WS, Mark LA, Billings SD, Meyers JL, Pech N, Travers JB, et al. Gene correction reduces cutaneous inflammation and granuloma formation in murine X-linked chronic granulomatous disease. J Invest Dermatol 2005;125:705-10.

70. Yu JE, Azar AE, Chong HJ, Jongco AM, 3rd, Prince BT. Considerations in the Diagnosis of Chronic Granulomatous Disease. J Pediatric Infect Dis Soc 2018;7:S6-s11.

71. Wolach B, Gavrieli R, de Boer M, van Leeuwen K, Berger-Achituv S, Stauber T, et al. Chronic granulomatous disease: Clinical, functional, molecular, and genetic studies. The Israeli experience with 84 patients. Am J Hematol 2017;92:28-36.

72. Nauseef WM, Clark RA. Intersecting Stories of the Phagocyte NADPH Oxidase and Chronic Granulomatous Disease. Methods Mol Biol 2019;1982:3-16.

73. Savina A, Jancic C, Hugues S, Guermonprez P, Vargas P, Moura IC, et al. NOX2 controls

phagosomal pH to regulate antigen processing during crosspresentation by dendritic cells. Cell 2006;126:205-18.

74. Mantegazza AR, Savina A, Vermeulen M, Pérez L, Geffner J, Hermine O, et al. NADPH oxidase controls phagosomal pH and antigen cross-presentation in human dendritic cells. Blood 2008;112:4712-22.

75. Sena LA, Li S, Jairaman A, Prakriya M, Ezponda T, Hildeman DA, et al. Mitochondria are required for antigen-specific T cell activation through reactive oxygen species signaling. Immunity 2013;38:225-36.

76. Kwon BI, Kim TW, Shin K, Kim YH, Yuk CM, Yuk JM, et al. Enhanced Th2 cell differentiation and function in the absence of Nox2. Allergy 2017;72:252-65.

77. Gu F, Krüger A, Roggenkamp HG, Alpers R, Lodygin D, Jaquet V, et al. Dual NADPH oxidases DUOX1 and DUOX2 synthesize NAADP and are necessary for Ca(2+) signaling during T cell activation. Sci Signal 2021;14:eabe3800.

78. Sugamata R, Donko A, Murakami Y, Boudreau HE, Qi CF, Kwon J, et al. Duox1 Regulates Primary B Cell Function under the Influence of IL-4 through BCR-Mediated Generation of Hydrogen Peroxide. J Immunol 2019;202:428-40.

79. Campbell AM, Kashgarian M, Shlomchik MJ. NADPH oxidase inhibits the pathogenesis of systemic lupus erythematosus. Sci Transl Med 2012;4:157ra41.

80. McCarthy MK, Reynoso GV, Winkler ES, Mack M, Diamond MS, Hickman HD, et al. MyD88-dependent influx of monocytes and neutrophils impairs lymph node B cell responses to chikungunya virus infection via Irf5, Nos2 and Nox2. PLoS Pathog 2020;16:e1008292.

81. Dasoveanu DC, Park HJ, Ly CL, Shipman WD, Chyou S, Kumar V, et al. Lymph node stromal CCL2 limits antibody responses. Sci Immunol 2020;5.

82. Lambeth JD, Neish AS. Nox enzymes and new thinking on reactive oxygen: a double-edged sword revisited. Annu Rev Pathol 2014;9:119-45.

83. Bronsart L, Nguyen L, Habtezion A, Contag C. Reactive Oxygen Species Imaging in a Mouse Model of Inflammatory Bowel Disease. Mol Imaging Biol 2016;18:473-8.

84. Zhong J, Olsson LM, Urbonaviciute V, Yang M, Bäckdahl L, Holmdahl R. Association of NOX2 subunits genetic variants with autoimmune diseases. Free Radic Biol Med 2018;125:72-80.

85. Lee K, Won HY, Bae MA, Hong JH, Hwang ES. Spontaneous and aging-dependent development of arthritis in NADPH oxidase 2 deficiency through altered differentiation of CD11b+ and Th/Treg cells. Proc Natl Acad Sci U S A 2011;108:9548-53.

86. Kim JM, Kim HK, Im YN, Bae YS, Im SY, Lee HK. FcγR/ROS/CK2α Is the Key Inducer of NF-κB Activation in a Murine Model of Asthma. Int Arch Allergy Immunol 2018;175:16-25.

87. Rada B, Leto TL. Oxidative innate immune defenses by Nox/Duox family NADPH oxidases. Contrib Microbiol 2008;15:164-87.

88. Hu CF, Wu SP, Lin GJ, Shieh CC, Hsu CS, Chen JW, et al. Microglial Nox2 Plays a Key Role in the Pathogenesis of Experimental Autoimmune Encephalomyelitis. Front Immunol 2021;12:638381.

89. Ravelli KG, Santos GD, Dos Santos NB, Munhoz CD, Azzi-Nogueira D, Campos AC, et al. Nox2-dependent Neuroinflammation in An EAE Model of Multiple Sclerosis. Transl Neurosci 2019;10:1-9.

90. Hahn J, Euler M, Kilgus E, Kienhöfer D, Stoof J, Knopf J, et al. NOX2 mediates quiescent handling of dead cell remnants in phagocytes. Redox Biol 2019;26:101279.

91. León-Lara X, Rodríguez-D'Cid R, Rioja-Valencia R, Ayala-Alvirde A, Aliaga-Taipe IL,

Espinosa-Padilla S, et al. [Clinical and molecular inflammatory alterations in chronic granulomatous disease]. Rev Alerg Mex 2020;67:370-80.

92. Marciano BE, Zerbe CS, Falcone EL, Ding L, DeRavin SS, Daub J, et al. X-linked carriers of chronic granulomatous disease: Illness, lyonization, and stability. J Allergy Clin Immunol 2018;141:365-71.

93. Angelino G, De Angelis P, Faraci S, Rea F, Romeo EF, Torroni F, et al. Inflammatory bowel disease in chronic granulomatous disease: An emerging problem over a twenty years' experience. Pediatr Allergy Immunol 2017;28:801-9.

94. Sobrino S, Magnani A, Semeraro M, Martignetti L, Cortal A, Denis A, et al. Severe hematopoietic stem cell inflammation compromises chronic granulomatous disease gene therapy. Cell Rep Med 2023;4:100919.

95. Wong RL, Sackey S, Brown D, Senadheera S, Masiuk K, Quintos JP, et al. Lentiviral gene therapy for X-linked chronic granulomatous disease recapitulates endogenous CYBB regulation and expression. Blood 2023;141:1007-22.

96. WHO. Global Tuberculosis Report 2022: World Health Organization; 2022.

97. Das S, Marin ND, Esaulova E, Ahmed M, Swain A, Rosa BA, et al. Lung Epithelial Signaling Mediates Early Vaccine-Induced CD4(+) T Cell Activation and Mycobacterium tuberculosis Control. mBio 2021;12:e0146821.

98. Fu H, Lewnard JA, Frost I, Laxminarayan R, Arinaminpathy N. Modelling the global burden of drug-resistant tuberculosis avertable by a post-exposure vaccine. Nat Commun 2021;12:424.

99. Smith CM, Proulx MK, Olive AJ, Laddy D, Mishra BB, Moss C, et al. Tuberculosis Susceptibility and Vaccine Protection Are Independently Controlled by Host Genotype. mBio 2016;7.

100. Neyrolles O, Quintana-Murci L. Sexual inequality in tuberculosis. PLoS Med 2009;6:e1000199.

101. Nhamoyebonde S, Leslie A. Biological differences between the sexes and susceptibility to tuberculosis. J Infect Dis 2014;209 Suppl 3:S100-6.

102. Dibbern J, Eggers L, Schneider BE. Sex differences in the C57BL/6 model of Mycobacterium tuberculosis infection. Sci Rep 2017;7:10957.

103. Zhao Y, Ying H, Demei J, Xie J. Tuberculosis and sexual inequality: the role of sex hormones in immunity. Crit Rev Eukaryot Gene Expr 2012;22:233-41.

104. Chandra P, Grigsby SJ, Philips JA. Immune evasion and provocation by Mycobacterium tuberculosis. Nat Rev Microbiol 2022;20:750-66.

105. Kotzé LA, Young C, Leukes VN, John V, Fang Z, Walzl G, et al. Mycobacterium tuberculosis and myeloid-derived suppressor cells: Insights into caveolin rich lipid rafts. EBioMedicine 2020;53:102670.

106. Xu W, Snell LM, Guo M, Boukhaled G, Macleod BL, Li M, et al. Early innate and adaptive immune perturbations determine long-term severity of chronic virus and Mycobacterium tuberculosis coinfection. Immunity 2021;54:526-41.e7.

107. Cooper AM, Segal BH, Frank AA, Holland SM, Orme IM. Transient loss of resistance to pulmonary tuberculosis in p47(phox-/-) mice. Infect Immun 2000;68:1231-4.

108. Jung YJ, LaCourse R, Ryan L, North RJ. Virulent but not avirulent Mycobacterium tuberculosis can evade the growth inhibitory action of a T helper 1-dependent, nitric oxide Synthase 2-independent defense in mice. J Exp Med 2002;196:991-8.

109. Ng VH, Cox JS, Sousa AO, MacMicking JD, McKinney JD. Role of KatG catalase-peroxidase in mycobacterial pathogenesis: countering the phagocyte oxidative burst. Mol Microbiol 2004;52:1291-302.

110. Shin SJ, Lee BS, Koh WJ, Manning EJ, Anklam K, Sreevatsan S, et al. Efficient differentiation of Mycobacterium avium complex species and subspecies by use of five-target multiplex PCR. J Clin Microbiol 2010;48:4057-62.

111. Kim WS, Kim JS, Cha SB, Kim H, Kwon KW, Kim SJ, et al. Mycobacterium tuberculosis Rv3628 drives Th1-type T cell immunity via TLR2-mediated activation of dendritic cells and displays vaccine potential against the hyper-virulent Beijing K strain. Oncotarget 2016;7:24962-82.

112. Kwon KW, Aceves-Sánchez MJ, Segura-Cerda CA, Choi E, Bielefeldt-Ohmann H, Shin SJ, et al. BCGΔBCG1419c increased memory CD8(+) T cell-associated immunogenicity and mitigated pulmonary inflammation compared with BCG in a model of chronic tuberculosis. Sci Rep 2022;12:15824.

113. Kang TG, Kwon KW, Kim K, Lee I, Kim MJ, Ha SJ, et al. Viral coinfection promotes tuberculosis immunopathogenesis by type I IFN signaling-dependent impediment of Th1 cell pulmonary influx. Nat Commun 2022;13:3155.

114. Lee JM, Park J, Reed SG, Coler RN, Hong JJ, Kim LH, et al. Vaccination inducing durable and robust antigen-specific Th1/Th17 immune responses contributes to prophylactic protection against Mycobacterium avium infection but is ineffective as an adjunct to antibiotic treatment in chronic disease. Virulence 2022;13:808-32.

115. Jeon BY, Kim SC, Eum SY, Cho SN. The immunity and protective effects of antigen 85A and heat-shock protein X against progressive tuberculosis. Microbes Infect 2011;13:284-90.

116. Kwon KW, Kim LH, Kang SM, Lee JM, Choi E, Park J, et al. Host-directed anti-mycobacterial activity of colchicine, an anti-gout drug, via strengthened host innate resistance reinforced by the IL-1β/PGE(2) axis. Br J Pharmacol 2022;179:3951-69.

117. Choi HG, Kwon KW, Choi S, Back YW, Park HS, Kang SM, et al. Antigen-Specific IFN-γ/IL-17-Co-Producing CD4(+) T-Cells Are the Determinants for Protective Efficacy of Tuberculosis Subunit Vaccine. Vaccines (Basel) 2020;8.

118. Qin S, Chen R, Jiang Y, Zhu H, Chen L, Chen Y, et al. Multifunctional T cell response in active pulmonary tuberculosis patients. Int Immunopharmacol 2021;99:107898.

119. Pfirschke C, Engblom C, Gungabeesoon J, Lin Y, Rickelt S, Zilionis R, et al. Tumor-Promoting Ly-6G(+) SiglecF(high) Cells Are Mature and Long-Lived Neutrophils. Cell Rep 2020;32:108164.

120. Rice CM, Davies LC, Subleski JJ, Maio N, Gonzalez-Cotto M, Andrews C, et al. Tumour-elicited neutrophils engage mitochondrial metabolism to circumvent nutrient limitations and maintain immune suppression. Nat Commun 2018;9:5099.

121. Kim MH, Yang D, Kim M, Kim SY, Kim D, Kang SJ. A late-lineage murine neutrophil precursor population exhibits dynamic changes during demand-adapted granulopoiesis. Sci Rep 2017;7:39804.

122. Evrard M, Kwok IWH, Chong SZ, Teng KWW, Becht E, Chen J, et al. Developmental Analysis of Bone Marrow Neutrophils Reveals Populations Specialized in Expansion, Trafficking, and Effector Functions. Immunity 2018;48:364-79.e8.

123. Endo D, Fujimoto K, Hirose R, Yamanaka H, Homme M, Ishibashi KI, et al. Genetic Phagocyte NADPH Oxidase Deficiency Enhances Nonviable Candida albicans-Induced Inflammation in Mouse Lungs. Inflammation 2017;40:123-35.

124. Moreira-Teixeira L, Stimpson PJ, Stavropoulos E, Hadebe S, Chakravarty P, Ioannou M, et al. Type I IFN exacerbates disease in tuberculosis-susceptible mice by inducing neutrophil-mediated lung inflammation and NETosis. Nat Commun 2020;11:5566.

125. Lovewell RR, Baer CE, Mishra BB, Smith CM, Sassetti CM. Granulocytes act as a niche

for Mycobacterium tuberculosis growth. Mucosal Immunol 2021;14:229-41.

126. Gupta T, Sarr D, Fantone K, Ashtiwi NM, Sakamoto K, Quinn FD, et al. Dual oxidase 1 is dispensable during Mycobacterium tuberculosis infection in mice. Front Immunol 2023;14:1044703.

127. Kim WS, Kim JS, Cha SB, Han SJ, Kim H, Kwon KW, et al. Virulence-Dependent Alterations in the Kinetics of Immune Cells during Pulmonary Infection by Mycobacterium tuberculosis. PLoS One 2015;10:e0145234.

128. Kim WS, Kim H, Kwon KW, Cho SN, Shin SJ. Immunogenicity and Vaccine Potential of InsB, an ESAT-6-Like Antigen Identified in the Highly Virulent Mycobacterium tuberculosis Beijing K Strain. Front Microbiol 2019;10:220.

129. Barbosa Bomfim CC, Pinheiro Amaral E, Santiago-Carvalho I, Almeida Santos G, Machado Salles É, Hastreiter AA, et al. Harmful Effects of Granulocytic Myeloid-Derived Suppressor Cells on Tuberculosis Caused by Hypervirulent Mycobacteria. J Infect Dis 2021;223:494-507.

130. Scanga CA, Bafica A, Feng CG, Cheever AW, Hieny S, Sher A. MyD88-deficient mice display a profound loss in resistance to Mycobacterium tuberculosis associated with partially impaired Th1 cytokine and nitric oxide synthase 2 expression. Infect Immun 2004;72:2400-4.

131. Silvério D, Gonçalves R, Appelberg R, Saraiva M. Advances on the Role and Applications of Interleukin-1 in Tuberculosis. mBio 2021;12:e0313421.

132. Juffermans NP, Florquin S, Camoglio L, Verbon A, Kolk AH, Speelman P, et al. Interleukin-1 signaling is essential for host defense during murine pulmonary tuberculosis. J Infect Dis 2000;182:902-8.

133. Mayer-Barber KD, Andrade BB, Oland SD, Amaral EP, Barber DL, Gonzales J, et al. Host-

directed therapy of tuberculosis based on interleukin-1 and type I interferon crosstalk. Nature 2014;511:99-103.

134. Gonzalez A, Hung CY, Cole GT. Absence of phagocyte NADPH oxidase 2 leads to severe inflammatory response in lungs of mice infected with Coccidioides. Microb Pathog 2011;51:432-41.

135. Felmy B, Songhet P, Slack EM, Müller AJ, Kremer M, Van Maele L, et al. NADPH oxidase deficient mice develop colitis and bacteremia upon infection with normally avirulent, TTSS-1- and TTSS-2-deficient Salmonella Typhimurium. PLoS One 2013;8:e77204.

136. Gopalakrishnan A, Dietzold J, Verma S, Bhagavathula M, Salgame P. Toll-like Receptor 2 Prevents Neutrophil-Driven Immunopathology during Infection with Mycobacterium tuberculosis by Curtailing CXCL5 Production. Infect Immun 2019;87.

137. Mishra BB, Lovewell RR, Olive AJ, Zhang G, Wang W, Eugenin E, et al. Nitric oxide prevents a pathogen-permissive granulocytic inflammation during tuberculosis. Nat Microbiol 2017;2:17072.

138. Scott NR, Swanson RV, Al-Hammadi N, Domingo-Gonzalez R, Rangel-Moreno J, Kriel BA, et al. S100A8/A9 regulates CD11b expression and neutrophil recruitment during chronic tuberculosis. J Clin Invest 2020;130:3098-112.

139. Bahlool AZ, Grant C, Cryan SA, Keane J, O'Sullivan MP. All trans retinoic acid as a host-directed immunotherapy for tuberculosis. Curr Res Immunol 2022;3:54-72.

140. O'Connor G, Krishnan N, Fagan-Murphy A, Cassidy J, O'Leary S, Robertson BD, et al. Inhalable poly(lactic-co-glycolic acid) (PLGA) microparticles encapsulating all-trans-Retinoic acid (ATRA) as a host-directed, adjunctive treatment for Mycobacterium tuberculosis infection. Eur J Pharm Biopharm 2019;134:153-65.

141. Yamada H, Mizuno S, Ross AC, Sugawara I. Retinoic acid therapy attenuates the severity

of tuberculosis while altering lymphocyte and macrophage numbers and cytokine expression in rats infected with Mycobacterium tuberculosis. J Nutr 2007;137:2696-700.

142. Mourik BC, Leenen PJ, de Knegt GJ, Huizinga R, van der Eerden BC, Wang J, et al. Immunotherapy Added to Antibiotic Treatment Reduces Relapse of Disease in a Mouse Model of Tuberculosis. Am J Respir Cell Mol Biol 2017;56:233-41.

143. Knaul JK, Jörg S, Oberbeck-Mueller D, Heinemann E, Scheuermann L, Brinkmann V, et al. Lung-residing myeloid-derived suppressors display dual functionality in murine pulmonary tuberculosis. Am J Respir Crit Care Med 2014;190:1053-66.

144. Tobita T, Takeshita A, Kitamura K, Ohnishi K, Yanagi M, Hiraoka A, et al. Treatment with a new synthetic retinoid, Am80, of acute promyelocytic leukemia relapsed from complete remission induced by all-trans retinoic acid. Blood 1997;90:967-73.

145. Watanabe H, Bi J, Murata R, Fujimura R, Nishida K, Imafuku T, et al. A synthetic retinoic acid receptor agonist Am80 ameliorates renal fibrosis via inducing the production of alpha-1-acid glycoprotein. Sci Rep 2020;10:11424.

146. Li L, Qi X, Sun W, Abdel-Azim H, Lou S, Zhu H, et al. Am80-GCSF synergizes myeloid expansion and differentiation to generate functional neutrophils that reduce neutropenia-associated infection and mortality. EMBO Mol Med 2016;8:1340-59.

147. Boivin G, Faget J, Ancey PB, Gkasti A, Mussard J, Engblom C, et al. Durable and controlled depletion of neutrophils in mice. Nat Commun 2020;11:2762.

148. Barber DL, Mayer-Barber KD, Feng CG, Sharpe AH, Sher A. CD4 T cells promote rather than control tuberculosis in the absence of PD-1-mediated inhibition. J Immunol 2011;186:1598-607.

149. Ahmed M, Tezera LB, Elkington PT, Leslie AJ. The paradox of immune checkpoint inhibition re-activating tuberculosis. Eur Respir J 2022;60.

150. Kim JH, Podstawka J, Lou Y, Li L, Lee EKS, Divangahi M, et al. Aged polymorphonuclear leukocytes cause fibrotic interstitial lung disease in the absence of regulation by B cells. Nat Immunol 2018;19:192-201.

151. Podstawka J, Sinha S, Hiroki CH, Sarden N, Granton E, Labit E, et al. Marginating transitional B cells modulate neutrophils in the lung during inflammation and pneumonia. J Exp Med 2021;218.

152. Ding W, Shimada H, Li L, Mittal R, Zhang X, Shudo K, et al. Retinoid agonist Am80-enhanced neutrophil bactericidal activity arising from granulopoiesis in vitro and in a neutropenic mouse model. Blood 2013;121:996-1007.

153. Naskar D, Teng F, Felix KM, Bradley CP, Wu HJ. Synthetic Retinoid AM80 Ameliorates Lung and Arthritic Autoimmune Responses by Inhibiting T Follicular Helper and Th17 Cell Responses. J Immunol 2017;198:1855-64.

154. Tomita A, Kiyoi H, Naoe T. Mechanisms of action and resistance to all-trans retinoic acid (ATRA) and arsenic trioxide (As2O 3) in acute promyelocytic leukemia. Int J Hematol 2013;97:717-25.

155. Cai W, Wang J, Hu M, Chen X, Lu Z, Bellanti JA, et al. All trans-retinoic acid protects against acute ischemic stroke by modulating neutrophil functions through STAT1 signaling. J Neuroinflammation 2019;16:175.

156. Basu S, Dunn A, Ward A. G-CSF: function and modes of action (Review). Int J Mol Med 2002;10:3-10.

157. Manz MG, Boettcher S. Emergency granulopoiesis. Nat Rev Immunol 2014;14:302-14.

158. Basu S, Hodgson G, Zhang HH, Katz M, Quilici C, Dunn AR. "Emergency" granulopoiesis in G-CSF-deficient mice in response to Candida albicans infection. Blood 2000;95:3725-33.

159. Rojano B, Caminero JA, Hayek M. Curving Tuberculosis: Current Trends and Future Needs. Ann Glob Health 2019;85.

160. Schade DS, Shey L, Eaton RP. Cholesterol Review: A Metabolically Important Molecule. Endocr Pract 2020;26:1514-23.

161. Hansen SB, Wang H. The shared role of cholesterol in neuronal and peripheral inflammation. Pharmacol Ther 2023;249:108486.

162. Huang B, Song BL, Xu C. Cholesterol metabolism in cancer: mechanisms and therapeutic opportunities. Nat Metab 2020;2:132-41.

163. Aguilar-Ballester M, Herrero-Cervera A, Vinué Á, Martínez-Hervás S, González-Navarro H. Impact of Cholesterol Metabolism in Immune Cell Function and Atherosclerosis. Nutrients 2020;12.

164. Daugvilaite V, Arfelt KN, Benned-Jensen T, Sailer AW, Rosenkilde MM. Oxysterol-EBI2 signaling in immune regulation and viral infection. Eur J Immunol 2014;44:1904-12.

165. Hofmaenner DA, Kleyman A, Press A, Bauer M, Singer M. The Many Roles of Cholesterol in Sepsis: A Review. Am J Respir Crit Care Med 2022;205:388-96.

166. Cyster JG, Dang EV, Reboldi A, Yi T. 25-Hydroxycholesterols in innate and adaptive immunity. Nat Rev Immunol 2014;14:731-43.

167. Cao Q, Liu Z, Xiong Y, Zhong Z, Ye Q. Multiple Roles of 25-Hydroxycholesterol in Lipid Metabolism, Antivirus Process, Inflammatory Response, and Cell Survival. Oxid Med Cell Longev 2020;2020:8893305.

168. Lu Z, McBrearty N, Chen J, Tomar VS, Zhang H, De Rosa G, et al. ATF3 and CH25H regulate effector trogocytosis and anti-tumor activities of endogenous and immunotherapeutic cytotoxic T lymphocytes. Cell Metab 2022;34:1342-58.e7.

169. Choi WS, Lee G, Song WH, Koh JT, Yang J, Kwak JS, et al. The CH25H-CYP7B1-RORα

axis of cholesterol metabolism regulates osteoarthritis. Nature 2019;566:254-8.

170. Canfrán-Duque A, Rotllan N, Zhang X, Andrés-Blasco I, Thompson BM, Sun J, et al. Macrophage-Derived 25-Hydroxycholesterol Promotes Vascular Inflammation, Atherogenesis, and Lesion Remodeling. Circulation 2023;147:388-408.

171. Kandutsch AA, Chen HW. Inhibition of sterol synthesis in cultured mouse cells by cholesterol derivatives oxygenated in the side chain. J Biol Chem 1974;249:6057-61.

172. Russell DW. Cholesterol biosynthesis and metabolism. Cardiovasc Drugs Ther 1992;6:103-10.

173. Zang R, Case JB, Yutuc E, Ma X, Shen S, Gomez Castro MF, et al. Cholesterol 25-hydroxylase suppresses SARS-CoV-2 replication by blocking membrane fusion. Proc Natl Acad Sci U S A 2020;117:32105-13.

174. Dang Y, Wang Y, Wei J, Zhang H, Yang Q, Wang B, et al. 25-Hydroxycholesterol inhibits Hantavirus infection by reprogramming cholesterol metabolism. Free Radic Biol Med 2024;224:232-45.

175. Wang S, Li W, Hui H, Tiwari SK, Zhang Q, Croker BA, et al. Cholesterol 25-Hydroxylase inhibits SARS-CoV-2 and other coronaviruses by depleting membrane cholesterol. Embo j 2020;39:e106057.

176. Qin FX, Jiang CY, Jiang T, Cheng G. New targets for controlling Ebola virus disease. Natl Sci Rev 2015;2:266-7.

177. Wu T, Ma F, Ma X, Jia W, Pan E, Cheng G, et al. Regulating Innate and Adaptive Immunity for Controlling SIV Infection by 25-Hydroxycholesterol. Front Immunol 2018;9:2686.

178. Zhao J, Chen J, Li M, Chen M, Sun C. Multifaceted Functions of CH25H and 25HC to Modulate the Lipid Metabolism, Immune Responses, and Broadly Antiviral Activities. Viruses 2020;12.

179. Wilkins C, Gale M, Jr. Sterol-izing innate immunity. Immunity 2013;38:3-5.

180. Park K, Scott AL. Cholesterol 25-hydroxylase production by dendritic cells and macrophages is regulated by type I interferons. J Leukoc Biol 2010;88:1081-7.

181. Xie T, Feng M, Dai M, Mo G, Ruan Z, Wang G, et al. Cholesterol-25-hydroxylase Is a Chicken ISG That Restricts ALV-J Infection by Producing 25-hydroxycholesterol. Viruses 2019;11.

182. Liu SY, Aliyari R, Chikere K, Li G, Marsden MD, Smith JK, et al. Interferon-inducible cholesterol-25-hydroxylase broadly inhibits viral entry by production of 25-hydroxycholesterol. Immunity 2013;38:92-105.

183. Blanc M, Hsieh WY, Robertson KA, Kropp KA, Forster T, Shui G, et al. The transcription factor STAT-1 couples macrophage synthesis of 25-hydroxycholesterol to the interferon antiviral response. Immunity 2013;38:106-18.

184. Zou T, Garifulin O, Berland R, Boyartchuk VL. Listeria monocytogenes infection induces prosurvival metabolic signaling in macrophages. Infect Immun 2011;79:1526-35.

185. Cho SJ, Pronko A, Yang J, Pagan K, Stout-Delgado H. Role of Cholesterol 25-Hydroxylase (Ch25h) in Mediating Innate Immune Responses to Streptococcus pneumoniae Infection. Cells 2023;12.

186. Reboldi A, Dang EV, McDonald JG, Liang G, Russell DW, Cyster JG. Inflammation. 25-Hydroxycholesterol suppresses interleukin-1-driven inflammation downstream of type I interferon. Science 2014;345:679-84.

187. Dang EV, McDonald JG, Russell DW, Cyster JG. Oxysterol Restraint of Cholesterol Synthesis Prevents AIM2 Inflammasome Activation. Cell 2017;171:1057-71.e11.

188. Takahashi H, Nomura H, Iriki H, Kubo A, Isami K, Mikami Y, et al. Cholesterol 25-hydroxylase is a metabolic switch to constrain T cell-mediated inflammation in the skin.

Sci Immunol 2021;6:eabb6444.

189. Xiao J, Wang S, Chen L, Ding X, Dang Y, Han M, et al. 25-Hydroxycholesterol regulates lysosome AMP kinase activation and metabolic reprogramming to educate immunosuppressive macrophages. Immunity 2024;57:1087-104.e7.

190. Fessler MB, Madenspacher JH, Baker PJ, Hilligan KL, Bohrer AC, Castro E, et al. Endogenous and Therapeutic 25-Hydroxycholesterols May Worsen Early SARS-CoV-2 Pathogenesis in Mice. Am J Respir Cell Mol Biol 2023;69:638-48.

191. Jang J, Park S, Jin Hur H, Cho HJ, Hwang I, Pyo Kang Y, et al. 25-hydroxycholesterol contributes to cerebral inflammation of X-linked adrenoleukodystrophy through activation of the NLRP3 inflammasome. Nat Commun 2016;7:13129.

192. Wong MY, Lewis M, Doherty JJ, Shi Y, Cashikar AG, Amelianchik A, et al. 25-Hydroxycholesterol amplifies microglial IL-1β production in an apoE isoform-dependent manner. J Neuroinflammation 2020;17:192.

193. Toral-Rios D, Long JM, Ulrich JD, Yu J, Strickland MR, Han X, et al. Cholesterol 25-hydroxylase mediates neuroinflammation and neurodegeneration in a mouse model of tauopathy. J Exp Med 2024;221.

194. Ahsan F, Maertzdorf J, Guhlich-Bornhof U, Kaufmann SHE, Moura-Alves P. IL-36/LXR axis modulates cholesterol metabolism and immune defense to Mycobacterium tuberculosis. Sci Rep 2018;8:1520.

195. Ngo MD, Bartlett S, Bielefeldt-Ohmann H, Foo CX, Sinha R, Arachchige BJ, et al. A Blunted GPR183/Oxysterol Axis During Dysglycemia Results in Delayed Recruitment of Macrophages to the Lung During Mycobacterium tuberculosis Infection. J Infect Dis 2022;225:2219-28.

196. Zhou S, Zhang D, Li D, Wang H, Ding C, Song J, et al. Pathogenic mycobacterium

upregulates cholesterol 25-hydroxylase to promote granuloma development via foam cell formation. iScience 2024;27:109204.

197. Shen ZJ, Hu J, Kashi VP, Kelly EA, Denlinger LC, Lutchman K, et al. Epstein-Barr Virus-induced Gene 2 Mediates Allergen-induced Leukocyte Migration into Airways. Am J Respir Crit Care Med 2017;195:1576-85.

198. Jia J, Conlon TM, Sarker RS, Taşdemir D, Smirnova NF, Srivastava B, et al. Cholesterol metabolism promotes B-cell positioning during immune pathogenesis of chronic obstructive pulmonary disease. EMBO Mol Med 2018;10.

199. Bartlett S, Gemiarto AT, Ngo MD, Sajiir H, Hailu S, Sinha R, et al. GPR183 Regulates Interferons, Autophagy, and Bacterial Growth During Mycobacterium tuberculosis Infection and Is Associated With TB Disease Severity. Front Immunol 2020;11:601534.

200. Kim H, Shin SJ. Pathological and protective roles of dendritic cells in Mycobacterium tuberculosis infection: Interaction between host immune responses and pathogen evasion. Front Cell Infect Microbiol 2022;12:891878.

201. Griffiths KL, Ahmed M, Das S, Gopal R, Horne W, Connell TD, et al. Targeting dendritic cells to accelerate T-cell activation overcomes a bottleneck in tuberculosis vaccine efficacy. Nat Commun 2016;7:13894.

202. Chalmin F, Rochemont V, Lippens C, Clottu A, Sailer AW, Merkler D, et al. Oxysterols regulate encephalitogenic CD4(+) T cell trafficking during central nervous system autoimmunity. J Autoimmun 2015;56:45-55.

203. Zeng G, Zhang G, Chen X. Th1 cytokines, true functional signatures for protective immunity against TB? Cell Mol Immunol 2018;15:206-15.

204. Lyadova IV, Panteleev AV. Th1 and Th17 Cells in Tuberculosis: Protection, Pathology, and Biomarkers. Mediators Inflamm 2015;2015:854507.

205. Bogunovic D, Byun M, Durfee LA, Abhyankar A, Sanal O, Mansouri D, et al. Mycobacterial disease and impaired IFN-γ immunity in humans with inherited ISG15 deficiency. Science 2012;337:1684-8.

206. Kimmey JM, Campbell JA, Weiss LA, Monte KJ, Lenschow DJ, Stallings CL. The impact of ISGylation during Mycobacterium tuberculosis infection in mice. Microbes Infect 2017;19:249-58.

207. Trindade BC, Ceglia S, Berthelette A, Raso F, Howley K, Muppidi JR, et al. The cholesterol metabolite 25-hydroxycholesterol restrains the transcriptional regulator SREBP2 and limits intestinal IgA plasma cell differentiation. Immunity 2021;54:2273-87.e6.

208. Kim JS, Kim WS, Choi HG, Jang B, Lee K, Park JH, et al. Mycobacterium tuberculosis RpfB drives Th1-type T cell immunity via a TLR4-dependent activation of dendritic cells. J Leukoc Biol 2013;94:733-49.

209. Choi S, Lee JM, Kim KES, Park JH, Kim LH, Park J, et al. Protein-energy restriction-induced lipid metabolism disruption causes stable-to-progressive disease shift in Mycobacterium avium-infected female mice. EBioMedicine 2024;105:105198.

210. Kwon KW, Lee A, Larsen SE, Baldwin SL, Coler RN, Reed SG, et al. Long-term protective efficacy with a BCG-prime ID93/GLA-SE boost regimen against the hyper-virulent Mycobacterium tuberculosis strain K in a mouse model. Sci Rep 2019;9:15560.

211. Kwon KW, Kim WS, Kim H, Han SJ, Hahn MY, Lee JS, et al. Novel vaccine potential of Rv3131, a DosR regulon-encoded putative nitroreductase, against hyper-virulent Mycobacterium tuberculosis strain K. Sci Rep 2017;7:44151.

212. Gröschel MI, Sayes F, Shin SJ, Frigui W, Pawlik A, Orgeur M, et al. Recombinant BCG Expressing ESX-1 of Mycobacterium marinum Combines Low Virulence with Cytosolic Immune Signaling and Improved TB Protection. Cell Rep 2017;18:2752-65.

213. Choi E, Choi HH, Kwon KW, Kim H, Ryu JH, Hong JJ, et al. Permissive lung neutrophils facilitate tuberculosis immunopathogenesis in male phagocyte NADPH oxidase-deficient mice. PLoS Pathog 2024;20:e1012500.

214. Yang JD, Mott D, Sutiwisesak R, Lu YJ, Raso F, Stowell B, et al. Mycobacterium tuberculosis-specific CD4+ and CD8+ T cells differ in their capacity to recognize infected macrophages. PLoS Pathog 2018;14:e1007060.

215. Steinbach S, Vordermeier HM, Jones GJ. Potential of the dual IFN-γ/IL-2 fluorescence-immunospot assay to distinguish different stages in bovine tuberculosis. Vet Immunol Immunopathol 2019;217:109930.

216. Mearns H, Geldenhuys HD, Kagina BM, Musvosvi M, Little F, Ratangee F, et al. H1:IC31 vaccination is safe and induces long-lived TNF-α(+)IL-2(+)CD4 T cell responses in M. tuberculosis infected and uninfected adolescents: A randomized trial. Vaccine 2017;35:132-41.

217. Granucci F, Andrews DM, Degli-Esposti MA, Ricciardi-Castagnoli P. IL-2 mediates adjuvant effect of dendritic cells. Trends Immunol 2002;23:169-71.

218. Han L, Jiang Q, Yao W, Fu T, Zeng Q. Thoracic injection of low-dose interleukin-2 as an adjuvant therapy improves the control of the malignant pleural effusions: a systematic review and meta-analysis base on Chinese patients. BMC Cancer 2018;18:725.

219. Gao X, Ren X, Zhang S, Song H, Guo X, Jia H, et al. Interleukin-2 shows high adjuvanticity for an inactivated vaccine against duck Tembusu virus disease. Poult Sci 2020;99:6454-61.

220. Mori N, Dorjkhorloo G, Shiraishi T, Erkhem-Ochir B, Okami H, Yamaguchi A, et al. A Mature Tertiary Lymphoid Structure with a Ki-67-Positive Proliferating Germinal Center Is Associated with a Good Prognosis and High Intratumoral Immune Cell Infiltration in Advanced Colorectal Cancer. Cancers (Basel) 2024;16.

221. Li LT, Jiang G, Chen Q, Zheng JN. Ki67 is a promising molecular target in the diagnosis of cancer (review). Mol Med Rep 2015;11:1566-72.

222. Voehringer D, Koschella M, Pircher H. Lack of proliferative capacity of human effector and memory T cells expressing killer cell lectinlike receptor G1 (KLRG1). Blood 2002;100:3698-702.

223. Zhang Y, Chen S, Tang X, Peng Y, Jiang T, Zhang X, et al. The role of KLRG1: a novel biomarker and new therapeutic target. Cell Commun Signal 2024;22:337.

224. Burl S, Adetifa UJ, Cox M, Touray E, Ota MO, Marchant A, et al. Delaying bacillus Calmette-Guérin vaccination from birth to 4 1/2 months of age reduces postvaccination Th1 and IL-17 responses but leads to comparable mycobacterial responses at 9 months of age. J Immunol 2010;185:2620-8.

225. Roy P, Vekemans J, Clark A, Sanderson C, Harris RC, White RG. Potential effect of age of BCG vaccination on global paediatric tuberculosis mortality: a modelling study. Lancet Glob Health 2019;7:e1655-e63.

226. Ordway DJ, Shang S, Henao-Tamayo M, Obregon-Henao A, Nold L, Caraway M, et al. Mycobacterium bovis BCG-mediated protection against W-Beijing strains of Mycobacterium tuberculosis is diminished concomitant with the emergence of regulatory T cells. Clin Vaccine Immunol 2011;18:1527-35.

227. Verrall AJ, Chaidir L, Ruesen C, Apriani L, Koesoemadinata RC, van Ingen J, et al. Lower Bacillus Calmette-Guérin Protection against Mycobacterium tuberculosis Infection after Exposure to Beijing Strains. Am J Respir Crit Care Med 2020;201:1152-5.

228. Whittaker E, Nicol MP, Zar HJ, Tena-Coki NG, Kampmann B. Age-related waning of immune responses to BCG in healthy children supports the need for a booster dose of BCG in TB endemic countries. Sci Rep 2018;8:15309.

229. Bohrer AC, Castro E, Tocheny CE, Assmann M, Schwarz B, Bohrnsen E, et al. Rapid GPR183-mediated recruitment of eosinophils to the lung after Mycobacterium tuberculosis infection. Cell Rep 2022;40:111144.

230. Zapała Ł, Wolny R, Wachowska M, Jakóbisiak M, Lasek W. Synergistic antitumor effect of JAWSII dendritic cells and interleukin 12 in a melanoma mouse model. Oncol Rep 2013;29:1208-14.

231. Gilmour BC, Corthay A, Øynebråten I. High production of IL-12 by human dendritic cells stimulated with combinations of pattern-recognition receptor agonists. NPJ Vaccines 2024;9:83.

232. Cheng EM, Tsarovsky NW, Sondel PM, Rakhmilevich AL. Interleukin-12 as an in situ cancer vaccine component: a review. Cancer Immunol Immunother 2022;71:2057-65.

233. Wang Z, Chen Y, Wu H, Wang M, Mao L, Guo X, et al. Intravenous administration of IL-12 encoding self-replicating RNA-lipid nanoparticle complex leads to safe and effective antitumor responses. Sci Rep 2024;14:7366.

234. Chen J, Madina BR, Ahmadi E, Yarovinsky TO, Krady MM, Meehan EV, et al. Cancer immunotherapy with enveloped self-amplifying mRNA CARG-2020 that modulates IL-12, IL-17 and PD-L1 pathways to prevent tumor recurrence. Acta Pharm Sin B 2024;14:335-49.

235. Kim H, Kwon KW, Kim WS, Shin SJ. Virulence-dependent induction of interleukin-10-producing-tolerogenic dendritic cells by Mycobacterium tuberculosis impedes optimal T helper type 1 proliferation. Immunology 2017;151:177-90.

236. Balkhi MY, Ma Q, Ahmad S, Junghans RP. T cell exhaustion and Interleukin 2 downregulation. Cytokine 2015;71:339-47.

237. Ross SH, Cantrell DA. Signaling and Function of Interleukin-2 in T Lymphocytes. Annu

Rev Immunol 2018;36:411-33.

238. Feau S, Arens R, Togher S, Schoenberger SP. Autocrine IL-2 is required for secondary population expansion of CD8(+) memory T cells. Nat Immunol 2011;12:908-13.

239. Redeker A, Welten SP, Baert MR, Vloemans SA, Tiemessen MM, Staal FJ, et al. The Quantity of Autocrine IL-2 Governs the Expansion Potential of CD8+ T Cells. J Immunol 2015;195:4792-801.

240. Yang Y, Lundqvist A. Immunomodulatory Effects of IL-2 and IL-15; Implications for Cancer Immunotherapy. Cancers (Basel) 2020;12.

241. Wyss A, Raselli T, Perkins N, Ruiz F, Schmelczer G, Klinke G, et al. The EBI2-oxysterol axis promotes the development of intestinal lymphoid structures and colitis. Mucosal Immunol 2019;12:733-45.

242. Bauman DR, Bitmansour AD, McDonald JG, Thompson BM, Liang G, Russell DW. 25-Hydroxycholesterol secreted by macrophages in response to Toll-like receptor activation suppresses immunoglobulin A production. Proc Natl Acad Sci U S A 2009;106:16764-9.

243. Gyu Choi H, Woong Kwon K, Jae Shin S. Importance of adjuvant selection in tuberculosis vaccine development: Exploring basic mechanisms and clinical implications. Vaccine X 2023;15:100400.

244. Kwon KW, Kang TG, Lee A, Jin SM, Lim YT, Shin SJ, et al. Protective Efficacy and Immunogenicity of Rv0351/Rv3628 Subunit Vaccine Formulated in Different Adjuvants Against Mycobacterium tuberculosis Infection. Immune Netw 2023;23:e16.

245. Abil OZ, Liu S, Yeh YW, Wu Y, Sen Chaudhuri A, Li NS, et al. A mucosal vaccine formulation against tuberculosis by exploiting the adjuvant activity of S100A4-A damage-associated molecular pattern molecule. Vaccine 2024; doi:10.1016/j.vaccine.2024.07.052.126151.

246. Ge X, Liang Z, Li K, Dong Y, Wang Y, Liu Y, et al. Selenium nanoparticles enhance mucosal immunity against Mycobacterium bovis infection. Int Immunopharmacol 2024;137:112384.

Abstract in Korean

마우스 모델에서 결핵 감수성 및 항결핵 면역 반응을 조절하는 숙주 면역 인자 연구

결핵(Tuberculosis, TB)은 *Mycobacterium tuberculosis* (Mtb) 감염으로 인하여 발생하는 높은 위험성을 지닌 폐 감염 질환으로, 전 세계적으로 매년 약 150만 명의 사망자를 지속적으로 발생시키는 극도로 위험한 질병이다. 결핵으로 인하여 야기되는 다양한 위험 인자들을 극복하기 위해서는 결핵의 병인 기전을 정확하게 이해하고 효과적인 결핵 예방 및 치료 수단을 개발할 수 있어야 하며, 그에 따라 항결핵 면역 반응 및 이러한 면역 반응의 수립에 기여하는 각각의 면역학적 요소들에 대한 심층적인 탐구가 필수적이다. *In vitro* 및 *in vivo* 실험들을 포괄하는 다양한 실험 및 연구들을 바탕으로, 결핵의 병인 기전 및 항결핵 면역 반응에 대한 이해도를 높이고 결핵에 대한 강력한 예방 및 치료 전략의 발전을 이끌어내는 것이 본 연구의 궁극적인 목표이다.

결핵 면역 병인(TB immunopathogenesis)의 맥락 하에서 결핵에 대한 면역 반응들을 깊이 이해하기 위해, 본 연구는 NADPH 산화효소 2 (NOX2) 결핍 ($Nox2^{-/-}$) 마우스 모델을 활용하는 새로운 접근법을 채택하였다. $Nox2^{-/-}$ 마우스 모델은 Mtb 감염을 통해 유도되는 면역 반응의 변화에 대한 연구를 수행하고 결핵에 대한 유전적 특이성을 지닌 환자들에게 특이적인 결핵 제어 전략을 연구하기에 적합한 모델로 판단되었다. $Nox2^{-/-}$ 마우스 모델의 결핵 면역 병인에 관여하는 요소들에 대한 연구는

숙주가 결핵균에 대응하는 데 있어 필수적이거나 혹은 유해한 새로운 경로 및 요소를 탐구할 수 있는 새로운 기회가 될 것이라고 판단되며, 결핵 면역 병인에 대한 포괄적인 이해도를 높이는 데도 큰 기여를 할 이라고 여겨진다. 또한 본 연구는 유전적 변이를 지닌 결핵에 취약한 환자들을 위해서 적용될 수 있는 숙주 지향 치료 요법 (host directed therapy) 의 가능성을 수립할 수 있는 기회로도 작용할 것이다.

제1장은 NADPH 산화효소 2 결핍이 숙주의 면역 반응에 미치는 영향을 포괄적으로 설명한다. 이 장은 NOX2 결핍으로 인하여 야기되는 다양한 면역학적 현상들에 주목하였으며, 특히 결핵균과 같은 세포 내 병원체 (intracellular pathogen) 에 대한 높은 취약성, 호중구 및 큰포식세포 기능의 결여, 면역 세포들의 비정상적인 활성화 및 과도한 염증 반응의 발생 등의 현상에 중점을 두었다. 후속 장들에서는 NOX2가 결여된 *Nox2*$^{-/-}$ 마우스가 결핵균에 감염되었을 때 이와 같은 비정상적인 면역 반응들이 발현하는지에 대한 여부를 확인하고, NOX2 결핍에 의하여 야기된 비정상적 면역 반응들이 *Nox2*$^{-/-}$ 마우스의 결핵 면역 병인에 어떤 역할을 수행하는지에 대해서 세부적으로 연구할 것이다.

제2장은 결핵에 대한 취약성을 보이는 수컷 *Nox2*$^{-/-}$ 마우스 모델의 수립 및 결핵의 면역 병인 진행과 관련된 면역학적 요소들을 스크리닝하는 과정에 초점을 맞추었다. 강력한 병원성을 지닌 임상 균주인 Mtb K 균주를 마우스에 감염시킨 결과, 수컷 *Nox2*$^{-/-}$ 마우스는 야생형 (Wild Type, WT) 마우스 및 암컷 *Nox2*$^{-/-}$ 마우스와 비교하였을 때 유의미하게 악화된 결핵 병변 및 진전을 보이는 것으로 확인되었다. 결핵에 취약한 수컷 *Nox2*$^{-/-}$ 마우스에서는 NOX2가 결핍으로 인하여 발생하는 대표적인 표현형들인 과도한 폐 염증 및 폐 내 면역세포 구성 비율의 불균형을 관찰할 수

있었으며, 그 중에서도 특히 결핵 심각성과 매우 강한 상관관계를 보이는 면역학적인 요소인 호중구들의 과도한 폐 유입이 두드러졌다. 본 장에서는 해당 호중구들이 WT 마우스의 호중구와 표현형적, 기능적인 차이를 보인다는 점을 규명하고 해당 호중구들이 수컷 *Nox2*$^{-/-}$ 마우스에 결핵 취약성을 부여하는 직접적인 요소임을 증명하였다.

제3장은 폐내 호중구의 병원성과 유해한 미성숙 호중구 생성에 필요한 면역학적 기전에 대하여 심층적으로 다루었다. 이 장은 미성숙한 폐 호중구의 표현형을 규명하고, 이러한 미성숙 호중구가 결핵 면역 병인에 있어 매우 중요한 요소임을 검증하였다. 본 장에서는 다양한 *in vivo* 연구를 통하여 어떠한 면역학적 인자가 미성숙 폐 호중구의 폭발적인 증가에 기여하는지 규명하였으며, 이를 통해 결핵균 감염에 의하여 유도된 G-CSF가 미성숙한 호중구의 형성에 가장 핵심적인 역할을 한다는 사실을 증명하였다. 본 연구 내용을 통하여 결핵 취약성을 조절하기 위해 G-CSF - 미성숙 호중구 축을 표적으로 하는 면역 치료의 가능성을 제시할 수 있었다.

제4장은 결핵에 대한 저항성을 나타내는 다른 마우스 모델을 활용하여 항결핵 면역을 조절하는 새로운 접근법을 연구하였다. 본 장에서는 새로운 TB 저항성 마우스 모델인 콜레스테롤 25-하이드록실레이즈 (Cholesterol 25-hydroxylase, CH25H) 가 결여된 *Ch25h*$^{-/-}$ 마우스의 결핵 면역 병인 기전을 분석하고 이를 결핵 예방에 활용할 수 있는 방안을 제시하였다. 본 장은 CH25H의 결여로 인하여 발생하는 선천적 면역 세포의 기능 변화가 수지상세포에 특이적으로 나타나며, 이들로 인해서 결핵균에 대한 방어에 있어 매우 중요한 역할을 끼치는 Th1 면역 반응이 증강된다는 사실을 새롭게 조명하였다. 또한, 이러한 발견을 바탕으로 통해 CH25H 의 결여 시 BCG

백신의 효능이 마우스 모델에서 크게 증가하며 효능이 장기적으로 유지된다는 점을 규명하여 결핵 예방에 대한 면역학적 활용 방안을 또한 제시하였다.

본 연구에서 조명한 NOX2, 미성숙 폐 호중구, G-CSF, CH25H 와 같은 다양한 숙주 요소들을 표적으로 하는 결핵 치료 및 예방 방식 전략들을 수립함으로서 결핵을 치료하고 예방하는 데에 매우 큰 기여를 할 수 있을 것으로 여겨진다.

핵심되는 말 : 결핵, 결핵균, 면역병리, NADPH Oxidase 2, 염증, 호중구, G-CSF, type I interferon, Cholesterol 25-hydroxylase, BCG

Publication list

1. Choi E, Choi HH, Kwon KW, Kim H, Ryu JH, Hong JJ, et al. Permissive lung neutrophils facilitate tuberculosis immunopathogenesis in male phagocyte NADPH oxidase-deficient mice. PLoS Pathog 2024;20:e1012500.
2. Kim H, Song EJ, Choi E, Kwon KW, Park JH, Shin SJ. Adjunctive administration of parabiotic Lactobacillus sakei CVL-001 ameliorates drug-induced toxicity and pulmonary inflammation during antibiotic treatment for tuberculosis. Int Immunopharmacol 2024;132:111937.
3. Kwon KW, Choi HG, Choi HH, Choi E, Kim H, Kim HJ, et al. Immunogenicity and protective efficacy of RipA, a peptidoglycan hydrolase, against Mycobacterium tuberculosis Beijing outbreak strains. Vaccine 2024;42:1941-52.
4. Kwon KW, Aceves-Sánchez MJ, Segura-Cerda CA, Choi E, Bielefeldt-Ohmann H, Shin SJ, et al. BCGΔBCG1419c increased memory CD8(+) T cell-associated immunogenicity and mitigated pulmonary inflammation compared with BCG in a model of chronic tuberculosis. Sci Rep 2022;12:15824.
5. Kwon KW, Kim LH, Kang SM, Lee JM, Choi E, Park J, et al. Host-directed anti-mycobacterial activity of colchicine, an anti-gout drug, via strengthened host innate resistance reinforced by the IL-1β/PGE(2) axis. Br J Pharmacol 2022;179:3951-69.
6. Choi HG, Kwon KW, Choi S, Back YW, Park HS, Kang SM, et al. Antigen-Specific IFN-γ/IL-17-Co-Producing CD4(+) T-Cells Are the Determinants for Protective Efficacy of Tuberculosis Subunit Vaccine. Vaccines (Basel) 2020;8.
7. Choi HH, Kwon KW, Han SJ, Kang SM, Choi E, Kim A, et al. PPE39 of the

Mycobacterium tuberculosis strain Beijing/K induces Th1-cell polarization through dendritic cell maturation. J Cell Sci 2019;132.

8. Kwon KW, Kim SJ, Kim H, Kim WS, Kang SM, Choi E, et al. IL-15 Generates IFN-γ-producing Cells Reciprocally Expressing Lymphoid-Myeloid Markers during Dendritic Cell Differentiation. International Journal of Biological Sciences 2019;15:464-80.

In Preparation

1. Choi ES, Kim HG, Kwon KW, Choi HH, Shin SJ, et al Enhanced DC-CD4^{+} T cell interaction drives long-lasting Th1 immunity in BCG-vaccinated *Ch25h*$^{-/-}$ mice. EMBO Journal.